Cover:

Čerenkov Free-Electron Lasers (CFELs) transform the kinetic energy from an accelerated electron beam into electromagnetic energy of a field. A typical CFEL design consists of a relativistic electron beam travelling along the axis of a dielectric-lined cylindrical waveguide. The liner of the waveguide reduces the phase velocity of the propagating wave such that, for a certain frequency, the wave and the electrons are velocity-matched. The modes with a non-zero electric field along the waveguide axis can exchange energy with the electrons. This coupling induces a bunching in the electron beam at the scale of the radiation wavelength. For a certain relative phase between these bunches and the electromagnetic wave, the electrons are decelerated and the field is amplified exponentially until saturation.

THEORY, DESIGN AND OPERATION OF A COMPACT ČERENKOV FREE-ELECTRON LASER

María Isabel de la Fuente Valentín

Promotiecommissie:

Prof. dr. ir. A. Bliek	University of Twente, Enschede
Prof. dr. K. J. Boller	University of Twente, Enschede
Dr. P. J. M. van der Slot	University of Twente, Enschede
Prof. dr. V. Subramaniam	University of Twente, Enschede
Prof. dr. M. Pollnau	University of Twente, Enschede
Prof. dr. W. J. van der Zande	Radboud University Nijmegen, Nijmegen

The research presented in this thesis was carried out at the
Laser Physics and Non-Linear Optics Group, University of Twente
P.O. Box 217, 7500 AE Enschede, The Netherlands.

ISBN 978-90-365-2475-9

THEORY, DESIGN AND OPERATION OF A COMPACT ČERENKOV FREE-ELECTRON LASER

PROEFSCHRIFT

ter verkrijging van
de graad van doctor aan de Universiteit Twente,
op gezag van de rector magnificus,
prof. dr. W.H.M. Zijm,
volgens het besluit van het College voor Promoties
in het openbaar te verdedigen
op vrijdag 9 maart 2007 om 13.15 uur

door

María Isabel de la Fuente Valentín
geboren op 10 November 1977
te Segovia, Spanje

Dit proefschrift is goedgekeurd door de promotor

Prof. dr. K. J. Boller

en de co-promotor

Dr. P. J. M. van der Slot

To my family,

Publications

- I. de la Fuente, P.J.M. van der Slot, and K.J. Boller, "Phase velocity fluctuations and gain in Cherenkov free-electron lasers", *Journal of Applied Physics*, **100** (5), 053108, (2006).
- I. de la Fuente, P.J.M. van der Slot, and K.J. Boller, "Liner radius fluctuations in a high-gain Cherenkov Free-Electron Laser", *Physical Review Special Topics: Accelerators and Beams*, **10**, (2), 20702, (2007).
- I. de la Fuente, P.J.M. van der Slot, and K.J. Boller, "Influence of liner Fluctuations on low- and high- gain Cherenkov FELs", 28th International Free Electron Laser Conference, Berlin, Germany, (2006), p. 118, http://www.JACoW.org.
- I. de la Fuente, P.J.M. van der Slot, and K.J. Boller, "A table-top Cerenkov FEL at 50 GHz", *Joint 29th International Conference on Infrared and Millimeter Waves and 12th International Conference on Terahertz Electronics*, Karlsruhe, Germany, (2004), p. 601.
- I. de la Fuente, P.J.M. van der Slot, and K.J. Boller, "A mm-wave table-top Cerenkov Free-Electron Laser", 26th International Free Electron Laser Conference and 11th FEL Users Workshop, Trieste, Italy, (2004), p. 314, http://www.JACoW.org.
- I. de la Fuente, P.J.M. van der Slot, and K.J. Boller, "The Effect of liner induced phase fluctuations on the gain of a Cerenkov FEL", 26th International Free Electron Laser Conference and 11th FEL Users Workshop, Trieste, Italy, (2004), p. 53, http://www.JACoW.org.
- P.J.M. van der Slot, I. de la Fuente, and K.J. Boller, "Waveguide Cerenkov Free-Electron Lasers as Compact THz sources", *2nd EPS-QEOD EuroPhoton Conference*, Pisa, Italy, (2006).
- P.J.M. van der Slot, I. de la Fuente, K.J. Boller, "Cerenkov Free-Electron Lasers as compact sources for THz radiation", *International Forum on Terahertz Spectroscopy and Imaging*, Kaiserslautern, Germany, (2006).

- I. de la Fuente, P.J.M. van der Slot, K.J. Boller, "Gain reduction in a Cerenkov FEL due to liner induced phase fluctuations", 30th fall meeting of the section Atomic Molecular and Optics Physics, Lunteren, The Netherlands, (2005).
- P.J.M. van der Slot, I. de la Fuente, K.J. Boller, "Off-resonance, self compensation of dielectric losses in a high gain Cherenkov FEL", Physics@Veldhoven, Veldhoven, The Netherlands, (2007).
- I. de la Fuente, P.J.M. van der Slot, and K.J. Boller, "Self-compensation of losses in a Cherenkov FEL", in preparation.

Abstract

Microwave radiation is extensively used in various fields of research and applications. An important example is the selective heating of materials. In particular, the so-called millimetre-wave radiation, which covers the wavelength range between 1 mm and 10 mm, has several advantages compared to radiation from standard microwave magnetrons, at a wavelength of about 12 cm. For example, in most technical ceramics dielectric absorption and, therefore, heating is stronger at higher microwave frequencies. Also, with higher frequency the heating radiation can be focused to smaller volumes which, together with a smaller penetration depth, becomes useful for applications which require spatially selective heating, *e.g.,* plasma production and metal sintering. However, current research into applications of millimetre-waves lacks a suitable source that provides appreciable output powers within the millimetre-wave range and, at the same time, offers the simplicity and compactness which is required for industrial applicability.

The objective of this thesis is to demonstrate that Čerenkov Free-Electron Lasers (CFELs) are a promising route towards such compact microwave sources with high-power and millimetre-wave output. The CFEL has already proven its general potential as wavelength tunable, high-frequency and high-power source in previous designs reported in literature, although at the expense of bulky constructions. The main aim here is to show that CFELs can actually be realized with a much reduced size such as, for example, a table-top device. The main obstacle to the realization of a compact device is that, to date, CFELs have required a rather strong electron current with a high kinetic energy to successfully bring the laser above threshold and into oscillation. Such electron beams cannot be generated in a compact setup. Here we demonstrate that CFELs can be brought into oscillation also with a much weaker electron beam current and with a much reduced kinetic energy. For this, we have theoretically and experimentally investigated a compact design of CFEL which should operate with a relatively small electron beam current of less than 1 A, and relatively low kinetic energy of less than 100 keV.

While the use of such low-current and low-energy electron beams is certainly the key for enabling an application of such sources, the problem is that such weak pumping may prevent the CFEL from reaching its threshold. In order to determine the corresponding minimum current

and energy of the electron beam, as with other lasers, it is required to carefully consider the presence of possible loss mechanisms. It transpires that some of these loss mechanisms were overlooked so far, and that they actually require careful consideration. In this thesis, we identified two loss mechanisms associated with the liner, the central element for wave amplification in the CFEL. These are the dielectric loss of the liner material and imperfections that can occur in the fabrication of a liner. To investigate the influence of these two effects we have generalized the existing theoretical model for CFELs. With this generalization, the model can be used to predict quantitatively the influence of dielectric liner loss and fabrication errors on the output power of such lasers. Especially, for compact CFELs that need to be based on weak pumping, we find that properly addressing these losses is essential for an experimental demonstration of laser oscillation.

For arriving at a suitable laser design we explored a wider range of laser parameters, such as pumping with low versus high-currents. These calculations predicted novel types of laser dynamics which will be of interest for the construction and operation of CFELs. We observed that high-current pumping provides a substantial gain for a broad range of frequencies over which the low-current pumped CFEL shows no wave amplification at all. Furthermore, this broadband gain does not seem to be affected even by large dielectric losses from the liner. Apparently, and in contrast to other laser systems, the transfer rate of energy from the electrons to the wave grows with increasing losses, which compensates the power dissipated in the liner. This results in an output power which is independent of loss over wide ranges. This is a quite remarkable property which, to our knowledge, is not present in any other type of laser.

For the design of the low-current CFEL, the numerical study yielded essential results for experimental implementation. In particular, it was found that in a low-current driven CFEL the dielectric loss and the liner radius irregularities, even if apparently small, can easily prevent the laser from reaching the threshold. Therefore, to bring a low-current pumped CFEL into operation, the selection of the liner in a CFEL, requires careful consideration of the material loss and radius tolerance levels, and is far from being a straightforward choice.

To achieve the experimental demonstration of the low-current pumped CFEL emission, we have selected modest pumping parameters, consisting on a maximum of 800 mA current and a maximum of 100 keV kinetic energy, which are consistent with a compact design. For emission in the V-band (40-75 GHz) and in the K-band (18-27 GHz), two designs of the lined waveguide were chosen, specifically, a 1.3 mm-thick quartz liner and a 1.5 mm-thick alumina liner with inner diameters of 3 mm and 4 mm, respectively. In order to preserve compactness, the total length of the waveguides was limited to 25 cm which, for the case of the quartz lined waveguide, involved configuration of the CFEL with a microwave resonator. This required a tailored design of the corresponding microwave outcoupler mirror. The electron beam was transported

through the waveguide by a magnetic field on the waveguide axis of about 0.15 T produced by a solenoid. The entire CFEL setup consists then of a 10 kV-800 mA electron gun, a post-acceleration section for energies of up to 100 keV, the solenoid for transporting the electron beam, the 25 cm long lined waveguide for the Čerenkov interaction, the outcoupler for the radiation, and a collector for the electron beam.

The experimental results showed what is, to our knowledge, the first working CFEL pumped with less than 1 A current and with electron energies below 100 keV. In practice, a quite weak pumping with only 250 mA current and 80 keV kinetic energy provided an output power of several watts centred at around 24 GHz. The output power level is in good agreement with the theoretical predictions for the experimental electron beam parameters, *i.e.,* about 250 mA electron beam current and 5 % energy spread, and for the experimental alumina liner parameters, *i.e.,* a maximum tangent loss of 10^{-3} and 3 % tolerance of the liner radius. The radiation was tunable at -0.15 GHz/kV, which matches well with the theoretically expected tuning rate.

From the experimental data and the generalized model, a number of specific modifications can now be identified which should lead to significant improvements of the laser output. A first step would be to improve the electron beam transport, which should lead to much higher output powers. In particular, to improve the quality of the electron beam, a more accurate means of electron beam alignment is required, in combination with a new design of the electron beam transporting solenoid and of the electron gun chamber. We expect that, thereafter, the full current emitted by the cathode, up to 800 mA, can be transported through the waveguide while the energy spreads can be reduced to only 1 %, leading to substantially increased gain. As an example, we expect from our model that, with the current experimental liners parameters, *i.e.,* a dielectric loss below 10^{-3} and precision machined liners of 3 % radius tolerance, and with an electron beam of 800 mA current and 75 keV kinetic energy, the CFEL would reach the kilowatt level both for the 50 GHz and the 22 GHz bands. This follow-up of the experimental work can be achieved by a systematic parametric characterization and stepwise modification of the technical design of the laser.

In conclusion, the investigations described in this work on realizing a millimetre-wave emitting CFEL with, to our knowledge, the weakest pumping and most compact design reported to date, are an important step in order to bring these promising laser sources towards industrial applications.

Samenvatting

Binnen vele gebieden in zowel wetenschappelijk onderzoek als in toepassingen wordt microgolfstraling gebruikt. Een belangrijk voorbeeld is het selectief verhitten van materialen. Millimeter golven, in het golflengtegebied tussen 1 mm en 10 mm, hebben een aantal voordelen boven microgolfstraling die in gewone magnetrons gebruikt wordt, met een golflengte van ca. 12 cm. Bijvoorbeeld, in de meeste technische keramische materialen is de diëlektrische absorptie, en daardoor, de verhitting sterker bij hogere microgolf frequenties. Bovendien kan, als er een hogere frequentie gebruikt wordt om te verhitten, de straling beter gefocust worden in kleinere volumes. Samen met een kleinere indringdiepte, wordt dit bruikbaar voor toepassingen waarbij ruimtelijk selectieve verhitting nodig is, bijvoorbeeld plasma productie en het sinteren van metaal. Echter, in het huidige onderzoek naar microgolftoepassingen ontbreekt een bron met voldoende vermogen in het millimeter gebied die ook nog eenvoudig en compact genoeg is voor een industriële toepassing.

Het doel van dit proefschrift is om te demonstreren dat de Čerenkov Vrije Electronen Lasers (CFELs) een veelbelovende route naar compacte microgolf bronnen met een hoog vermogen bij millimetergolven bieden. De CFEL heeft zijn potentieel al bewezen als een in golflengte verstembare, hoogfrequente, hoog vermogen bron in voorgaande ontwerpen zoals die in de literatuur beschreven worden. Echter, tot nu toe bestaan deze ontwerpen uit grote constructies. Het hoofdoel is hier om te laten zien dat een CFEL gemaakt kan worden die gereduceerd is in formaat, zodat het een apparaat wordt dat op een enkele tafel gezet zou kunnen worden. De belangrijkste obstakels om een compacte CFEL te maken is dat, tot nu toe, CFELs een grote elektronenstroom met een hoge kinetische energie nodig hebben om de laser boven de laserdrempel te krijgen en dat deze elektronenbundels in een compacte configuratie niet gerealiseerd worden. Hier laten we zien dat CFELs ook met een veel kleinere elektronenbundelstroom boven de laserdrempel gebracht kan worden. Hiervoor hebben we theoretisch en experimenteel een compact ontwerp voor een CFEL onderzocht. In dit ontwerp heeft de CFEL een relatief kleine elektronenbundelstroom van minder dan 1 A en een relatief geringe kinetische energie van 100 keV nodig.

Hoewel het gebruiken van een lage stroom zeker de manier is om de toepassing van dit soort bronnen mogelijk te maken, is het probleem dat een dergelijke elektronenbundelstroom de CFEL wellicht niet boven de laserdrempel kan krijgen. Om de minimale stroom en energie voor de elektronenbundel te bepalen is het nodig om, net als met andere lasers, de aanwezigheid van mogelijke verliesmechanismen zorgvuldig te analyseren. Hierbij zijn een aantal verliesmechanismen aan het licht gekomen die tot nu to over het hoofd zijn gezien, en deze mechanismen vragen om een zorgvuldige analyse. In dit proefschrift bepalen we twee verlies mechanismen die in verband worden gebracht met de diëlektrische bekleding van de binnenkant van een golfpijp, het centrale element voor de versterking van golven in de CFEL. Deze zijn de diëlektrische verliezen van het het materiaal waar de bekleding van gemaakt is en imperfecties die kunnen voorkomen in de produktie van de bekleding. Om de invloed van deze twee effecten te onderzoeken hebben we het bestaande theoretische model van CFELs uitgebreid. Met deze uitbreiding kan het model gebruikt worden om de invloed van de diëlektrische verliezen in de bekleding en fabricage fouten op het uitgangsvermogen van CFELs kwantitatief te voorspellen. Vooral voor compacte CFELs, die gebaseerd moeten zijn op een zwakke elektronenbundelstroom, is het van essentieel belang dat de verliezen goed in kaart gebracht worden om in een experiment te laten zien dat er laseroscillatie optreedt.

Om tot een geschikt laserontwerp te komen, hebben we een groter aantal variabelen onderzocht, zoals het vergelijken van pompen met een lage stroom en een hoge stroom. De berekeningen die we hiervoor gedaan hebben voorspellen nieuwe soorten dynamisch gedrag die van belang zullen zijn bij het ontwerp van een CFEL en de werking ervan. We laten zien dat bij een hoge pompstroom er versterking plaatsvindt over een brede frequentieband, terwijl bij een lage pompstroom er in deze frequentieband in de CFEL geen enkele versterking te zien is. Bovendien blijkt het zo te zijn dat deze breedbandversterking niet beïnvloed wordt door zelfs grote diëlektrische verliezen in de bekleding. Kennelijk, in tegenstelling tot andere laser systemen, neemt de snelheid waarmee elektronenenergie overdragen wordt aan de electromagnetische golf toe als de verliezen toenemen, en dit compenseert het verlies in de bekleding. Dit resulteert in een uitgangsvermogen dat onafhankelijk is van de verliezen over een brede frequentieband. Dit is een opmerkelijke eigenschap, die voor zover wij weten, in geen enkel ander type laser gevonden kan worden.

Voor het ontwerp van een CFEL die gepompt wordt met een lage pompstroom, heeft de numerieke modellering resultaten opgeleverd die essentieel zijn om tot een experiment te komen. In het bijzonder werd gevonden dat bij een lage pompstroom de diëlektrische verliezen en onregelmatigheden in de bekleding, zelf als ze klein lijken, makkelijk kunnen verhinderen dat de CFEL de laserdrempel haalt. Hierdoor heeft de keuze voor een bekleding voor een CFEL als hier voorgesteld een zorgvuldige afweging met betrekking tot de verliezen in het materiaal en

de toleranties in de radius nodig, en is zeker geen recht toe recht aan overweging.

Voor een experimentele demonstratie hebben we gekozen voor bescheiden parameters voor de elektronenbundel, bestaande uit een maximum stroom van 800 mA en een maximale kinetische energie van 100 keV. Deze getallen zijn consistent met een compact ontwerp. Om straling in de V-band (40-75 GHz) en in de K-band (18-27 GHz) te kunnen uitzenden, zijn twee verschillende ontwerpen voor de bekleding gemaakt: een 1.3 mm dikke quartz bekleding met een inwendige diameter van 3 mm en een 1.5 mm dikke aluminiumoxide bekleding met een inwendige diameter van 4 mm. In het belang van het compacte ontwerp is de totale lengte van de golfgeleider beperkt tot 25 cm. Voor het geval van de quartz bekleding is de single-pass gain laag en is een microgolf resonator noodzakelijk. Dit betekende dat er een aanpast ontwerp van de bijbehorende microgolf uitkoppelspiegel nodig was. Om de elektronenbundel door de golfpijp te geleiden is een magnetisch veld gebruikt. Dit veld, opgewekt met een spoel, is langs de as van de golfpijp gericht en heeft een sterkte van 0.15 T. De totale CFEL opstelling bestaat dan uit een 10 kV-800 mA elektronenkanon, een na-versneller met een energie tot 100 keV, de spoel om de bundel te geleiden, de 25 cm lange golfgeleider voor de Čerenkov wisselwerking, de uitkoppeling voor de straling en een collector voor de elektronenbundel.

Het experiment laat zien dat, voor zover wij weten, we de eerste werkende CFEL hebben gemaakt die gepompt kan worden met een stroom van minder dan 1 A en met een elektronenenergie van minder dan 100 keV. Het is gebleken dat een stroom van slechts 250 mA en een energie van 80 keV een uitgangsvermogen geven van een aantal watt rond de 24 GHz. Dit uitgangsvermogen komt goed overeen met de theoretische voorspellingen van de parameters voor de elektronenbundel, d.w.z., ongeveer 250 mA elektronenbundelstroom en 5 % spreiding in de energie, en voor de experimentele parameters voor de aluminiumoxide bekleding, d.w.z., een maximaal tangentieel verlies van 10^{-3} en 3 % tolerantie op de straal van de bekleding. De straling was verstelbaar met -0.15 GHz/kV wat goed overeenkomt met de theoretisch verwachtte verstemmingsratio.

Uit de experimentele data en het uitgebreide model kunnen een aantal specifieke aanpassingen geïdentificeerd worden die tot significante verhogingen van het uitgangsvermogen van de laser zouden moeten leiden. Een eerste stap om tot hogere uitgangsvermogens te komen, zou verbeteren van de elektronenbundelgeleiding moeten zijn. In het bijzonder dient de kwaliteit van de elektronenbundel verbeterd te worden, aan het magneetsysteem voor bundelgeleiding, wat mogelijk ook aanpassing van e anode kamer vereist. We verwachten dat als dit is gedaan de hele stroom van 800 mA, die door de cathode wordt uitgezonden, door de golfpijp geleid kan worden en dat de spreiding in energie gereduceerd wordt tot 1 %, en er dus substantieel meer versterking te halen zal zijn. We verwachten bijvoorbeeld op basis van ons model, dat de CFEL wel een uitgangsvermogen van meer dan een kilowatt voor zowel de 50 GHz als de

22 GHz band zou moeten kunnen halen met de huidige experimentele bekleding parameters, d.w.z, een diëlektrisch verlies beneden 10^{-3}, met precisie gemaakte bekledingen met een tolerantie van 3 % in de straal, en met een elektronenbundel met een stroom van 800 mA en een energie van 75 keV. De volgende stap in het experimentele werk bestaat uit een systematische karakterisering van de parameters en een stapsgewijze aanpassing van het technische ontwerp van de laser.

Tot besluit willen we opmerken dat het onderzoek dat in dit proefschrift wordt beschreven over de realisatie van een millimeter-golf CFEL met, voor zover wij weten, de zwakste elektronenbundelstoom en het kleinste ontwerp dat tot op heden bekend is, een belangrijke stap is om deze veelbelovende lasers in de industrie toe te passen.

Contents

1

Introduction

When H. Hertz (1857-1894) demonstrated the existence of the electromagnetic waves predicted by Maxwell, he measured waves of about 0.5 GHz frequency [1], which are nowadays known as microwaves. Microwave radiation ranges in frequency between 0.3 GHz and 300 GHz or, equivalently, in wavelengths between 1 mm to 1 m. Microwaves have found applications spanning a wide range of fields, from the most pure fundamental research to common devices present in our daily lives. In the beginning, microwaves were mainly used for long-distance communications, and this application is extensively used today in satellite systems, millimetre waveguide communications and modern microwave radios [2]. High power microwaves are also used in fundamental research, *e.g.,* in controlled fusion experiments for driving steady-state currents in magnetically confined plasmas [3], and as RF source for particle accelerators and TeV linear colliders [4]. However, microwaves are mostly used as heating mechanism, due to their ability to excite the vibrational modes of the molecules in many materials. Heating of materials by using microwave technology shows a number of advantages against conventional infrared heating, *e.g.,* the heating can be highly selective when applied to specific resonances of the material, it is volumetric, and allows for instantaneous control. It is thus not surprising to find uncountable examples where the microwave heating technology is adopted. For example, microwaves are used in healthcare to heat human tissue, which is known as microwave diathermy [5], for treatment of ceramics and polymers [6, 7, 8], mineral leaching and processing [9, 10], waste remedial [11], welding of thermoplastics [12, 13] and food and timber processing. Also, microwave-generated plasmas [14] are applied for thermal spraying [15], for sterilisation [16] and for ceramic processing [17, 18].

In view of all the examples above, one might expect that microwave technology is well developed and settled in many industrial environments. Nevertheless, many of the applications are still in a developing stage, and some effects associated to microwaves cannot be fully explained. Such is the case of certain microwave-irradiated chemical processes, which have shown to follow different reaction paths and different yields depending on the frequency of the radiation [19, 20]. Clearly, the use of other microwave frequencies could improve the efficiency

and also open new areas of application. For example, the size of a microwave plasma jet, that can be produced with a 2.46 GHz magnetron [18], reduces with increasing frequency and can become comparable to a laser plasma jet for, *e.g.,* 50 GHz. Also, millimetre waves, *i.e.,* with wavelengths between 1 mm and 10 mm, have strong advantages for the microwave heating of powdered metals [21]. However, most of the current industrial applications are limited to the frequencies of the magnetron, *i.e.,* 915 MHz and 2.46 GHz, since the magnetron is the only source that has found a path into widespread commercialization thanks to its compact design. In particular, one of the main limitations for further research into novel applications of microwaves is the lack of a high power microwave source with the portability of the magnetron and, additionally, operating at higher and tunable frequencies.

For microwave heating, electron tube-type sources are usually employed. The history of the vacuum tube sources goes back to the 1930's, when the first centimetre-wave sources appeared. They were used by radars in World War II, which accelerated their evolution. For example, the klystron [22], the cavity magnetron [23] and the travelling wave tube (TWT) [24] experienced an enormous development during those decades [25]. About the same time, in 1947, Motz suggested that a periodic magnetic structure, which he termed an undulator, could be used to generate high power electromagnetic radiation using an electron beam [26]. In 1957, Phillips built the so called ubitron that amplified microwave radiation by using the undulator and a non-relativistic electron beam [27]. However, for most of the electron tubes till then, the transversal size decreased with increasing frequency, which had associated power dissipation problems, thus limiting the maximum achievable power for increasing frequencies. Such problems were somewhat overcome by the gyrotron, invented in 1967, which could afford large transversal dimensions compared to the wavelength and, therefore, offered the opportunity to deal with very high power at high frequencies [28]. A novel type of vacuum device would arrive in 1971, when Madey proposed the so called Free-Electron Laser (FEL), a relativistic version of the ubitron [29]. Six years later, his proposal successfully led to the first experimental demonstration of a FEL amplifier [30] and of a FEL oscillator [31] and caused a huge interest in such devices [32, 33, 34, 35, 36, 37]. Today, FELs are high power sources not only in the microwave region but also over the entire electromagnetic spectrum. In summary, the development of vacuum tube devices during the second half of last century has yielded several types of microwave sources. They can provide high frequencies and high powers, and some of them are used today for heating applications.

In order to use microwaves in production technologies, most of the sources above are technologically feasible and fulfil a need, but each one of them suffers from some severe drawbacks [25]. For example, the gyrotron can reach megawatt power levels at a few hundreds of gigahertz with no special difficulties and, therefore, has no competitors when very high powers and

very high microwave frequencies are needed. However, these gyrotrons use superconducting magnets resulting in bulky and expensive devices. Another example is the FEL, which is more advantageous than the gyrotron when tunability, bandwidth, beam quality or short-pulse length are required [38]. However, FELs are also big-size devices with at least some tens of meters of length, and not specially efficient at microwaves. Nevertheless, to increase the efficiency in the microwave range, a FEL can be configured as a slow-wave device, where the most promising approach is the so-called Čerenkov Free-Electron Laser (CFEL). The CFEL shows the potential to work more reliably and efficient than the undulator FEL for high microwave frequency generation [39]. Furthermore, its design is relatively simple because no undulator is required as in a standard FEL. The CFEL is also advantageous as microwave emitter when compared to other slow-wave sources such as the TWT, especially at high microwave frequencies. Here, even under a more optimistic view, the expected power levels of the TWT are still well below the levels that can be produced with a laboratory CFEL source [40]. Also, the interaction structure of the TWT for high microwave frequencies is mechanically demanding against the simplicity of the CFEL structure.

The use of the Čerenkov effect as a source of microwave radiation was first introduced by Ginzburg in 1947 [41] and the first successful experiment to detect microwave Čerenkov radiation was reported by Danos *et al.* [42]. Some years later, spontaneous emission from a pre-bunched electron beam travelling near a dielectric loaded structure was observed [43]. The progress in the production of high quality and high current relativistic electron beams allowed in 1977 for the first demonstration of the stimulated Čerenkov process [44]. After that, the CFEL has proved to be an efficient emitter within the millimetre and sub-millimetre wavelength regions and a wealth of experimental work has been reported [40, 45, 46, 47, 48, 49, 50, 51]. In the first CFEL experiment, Walsh *et al.* obtained radiation at 60 GHz and with an output power of 1 MW [44]. Such high output powers were only possible at the expense of a high-energy and high-current electron beam, 0.5 MeV and 10 kA in that case. More moderate electron beam energies, although still high electron beam currents, have also shown to provide large output powers. For example, Von Laven *et al.* [46] achieved 50 GHz with an output power of 30 kW with a 115 kV and 12 A electron beam, and Felch *et al.* [47] obtained radiation between 20-30 GHz up to 1 kW with a 150 kV, 10 A electron beam. The CFEL has also shown potential to reach high microwave frequencies, of a few hundreds of GHz. For example, Garate *et al.* [52] achieved a power level of approximately 100 kW at 88 GHz and demonstrated operation on higher-order modes at frequencies up to 320 GHz, using a current density of 10 $\mathrm{A/cm^2}$ and voltages up to 300 kV. Radiation at frequencies higher than 300 GHz or, equivalently, wavelengths shorter than 1 mm was obtained by Garate *et al.* with a slab-type device [49]. They obtained tunable radiation from 375 μm to 1 mm wavelengths using electrons currents

between 35 A and 100 A and electron energies between 0.5 MeV and 1 MeV. Another example of short-wavelength emission is the CFEL operating at the beginning of the 1990's in ENEA (Italy) [53] based on 5.3 MeV and 3 A electron pulses from which powers of up to 50 W at the wavelengths of 1.6 mm and 0.9 mm were obtained.

The CFEL can thus provide high output power, in the kilowatt level, and operate at the high frequency edge of the microwave spectrum, although at the expense of large electron beam currents. To handle such high currents, the experimental setup, unfortunately, becomes large and technically complex. As a result, none of the CFELs reported in literature is a convenient choice for a compact microwave source. Nevertheless, if the required power by the specific applications of the source is only a few hundreds of watts, the use of low currents and energies becomes a highly interesting option and may yield a compact device. However, to achieve such goal, *i.e.,* preserving appreciable output power also for low electron beam currents and energies, is one of the big potentials of the CFELs that needs to be investigated.

Concluding, the CFEL is a promising compact source for research into novel microwave applications due to some unique properties: unlike other slow wave devices, the output powers remain high when the frequency of the emission increases; the CFEL can have a small size, for it can afford voltages as low as a few tens of kilovolts and electron beam currents as low as a few hundreds of milliamp; and, finally, the CFEL structure for interaction is very simple compared to other sources, since it consists essentially of a dielectric-lined waveguide. Overall, the CFEL is of special interest when millimetre-waves and appreciable output powers are to be generated with a compact device [54]. Nevertheless, there has been, so far, no attempt to realize such a source in a compact size. In this thesis, we study, theoretically and experimentally, the possibility of obtaining high microwave frequencies at appreciable power using a CFEL with a footprint size smaller than one square metre.

1.1 Outline of the thesis

The outline of this thesis can best be understood by looking into the chronological sequence of events during the research work. Initially, an experimental investigation into the emission of the CFEL at around 50 GHz showed difficulties for lasing, and was traced back to an insufficient low single-pass gain as well as unexpectedly high losses in the CFEL. These difficulties motivated us to first investigate the causes of such low performance, which resulted in a theoretical study of gain depression and several types of losses, which has never been presented before. These theoretical studies were very useful to understand the possible reasons for insufficient gain. This led us to a different liner design that evolved towards the first experimental demonstration on the microwave production using a CFEL with less than 1 A electron beam current,

and a footprint of less than one square meter. With this background, the thesis is organized as follows:

In Chapter 2, we recall the theoretical model that describes the basic working principle of a CFEL [55], and we implement this model in a numerical approach to describe the three-dimensional and non-linear evolution of the laser field. The model is based on the self-consistent set of Maxwell and Newton-Lorentz equations. Our novel contribution to the theory is that we introduce a more accurate calculation of the wave amplification, which allows to include important local effects, namely, the presence of dielectric losses in the liner and an irregularity of the liner parameters.

In Chapter 3, we investigate numerically the gain of a CFEL both in the low- and in the high-gain regimes of operation, including the presence of the two types of gain degradation described in the Chapter 2. On the one hand, this is of fundamental interest, since we found an unexpected behaviour for frequencies below resonance when the CFEL is pumped with a high electron current. In this case, the high-current pumped CFEL seems to adjusts its own dynamics to the presence of losses by inducing a higher amplification of the wave, just sufficient to compensate the dissipation caused by the losses. On the other hand, this chapter gives quantitative information on the effects of the different types of losses at resonance, which are of high value for a proper design of an experimental CFEL.

In Chapter 4, we investigate numerically the generation of high-power microwave frequencies with a CFEL of reduced size. The novelty from this type of CFEL versus other CFELs reported in literature is the use of low currents and low energies in the electron beam. To reduce the size of the CFEL as much as possible by avoiding a long lined-waveguide for the interaction, we also study the possibility of configuring the CFEL within a microwave resonator. To obtain a realistic laser design for an experiment, we have included the presence of losses.

In Chapter 5, we describe the experimental setup of the CFEL. This includes the design of the main components of the CFEL, *i.e.,* of the electron gun, of the system to accelerate and transport the electron beam and of the out-coupler of the radiation. Special emphasis is put on the propagation of the electron beam near the dielectric material, the radiation feedback and output coupling, and the separation of the electron beam from the radiation.

In Chapter 6, we present the first experimental results from the operation of the CFEL around a frequency of 24 GHz. This is done on the basis of a prior characterization of the experimental pumping conditions, in particular, with regard to the current and energy of the beam, as well as the proper operation of the electron gun and the electron beam transport.

Finally, in Chapter 7, the main conclusions from this thesis are given.

2

Theory of the Čerenkov Free-Electron Laser

Abstract

In the present chapter, we present a three-dimensional and non-linear description of a Čerenkov Free-Electron Laser (CFEL) amplifier, based on the solution of the self-consistent set of Maxwell and Newton-Lorentz equations. Further, we investigate the modelling of several types of losses associated to a CFEL. Specifically, we model the dynamics of a CFEL when the liner has non-negligible dielectric losses and when the liner shows irregularities in the radius along the waveguide. This generalization of the CFEL model, which does not exist in the former literature on CFELs, provides an important tool for gain analysis in a CFEL, especially in low-gain devices, that are extremely sensitive to the losses.

The theory of the Čerenkov Free-Electron Laser (CFEL) describes the dynamics of an electromagnetic field and of an electron beam when they co-propagate in a waveguide lined with a dielectric material. There are several models of the CFEL, such as the model by Walsh [56] and the model by Freund [57], which have explained satisfactory experimental results [52, 47]. However, the existing models fail to describe the effects of some types of losses which are specific for the CFEL. One example is the dielectric loss of the liner material, which produces attenuation of the propagating wave and results in heat dissipation. Another example are the imperfections in the thickness of the liner, which produce a variable phase velocity of the propagating wave and, thus, affect the dynamics of the system. We generalized in this chapter the three-dimensional and non-linear model of the CFEL amplifier of Freund [57] by including the dielectric losses of the liner and the thickness irregularities of the lined waveguide. The organization of the chapter is as follows. We present the CFEL model in section 2.1. Our novel contribution to the theory is given in sections 2.2 and 2.3, where we describe the effects of the dielectric losses in the liner and of the varying phase velocity of the fields, respectively.

2.1 Model of the Čerenkov Free-Electron Laser

The CFEL is a particular case of the Free Electron Laser (FEL), the latter being proposed in 1971 by John M.J. Madey [29]. In his model, Madey used quantum-mechanics to describe a relativistic FEL but it was later found that the FEL can be accurately modelled within the frame of classical mechanics. Nowadays, the descriptions of the field-particle dynamics in the FEL are diverse, including a Hamiltonian treatment [58], a Maxwell-Vlasov distribution function treatment [35], and a self-consistent Maxwell-Lorentz treatment [59]. A unified theory was published in 1981 by Gover and Sprangle [36], in which all kinds of FELs satisfy the same gain-dispersion relation and differ only in a single coupling parameter. Models particular for the CFEL were promptly developed after the first clear-cut demonstration of emission of stimulated Čerenkov radiation in 1977 [44, 45, 60, 61].

One of the main differences among the existing models for the CFEL is whether they use a linear approximation for the interaction between the electromagnetic wave and the electrons. In many of the early models of the CFEL, the amplification of the wave is described within the limits of the linear approximation, such as the model of Walsh and co-workers, who treat the electron beam as a linear fluid and describe the dynamics of the electrons by using the continuity and the Lorentz force equations. They have modelled the CFEL both in the single-particle regime and the high-gain dense-beam regime [62, 56]. The linear description gives a practical analytical tool to describe the gain, but only provides estimations of the saturation efficiency, and thus of the maximum output power. To describe the evolution of the wave further from the linear regime, a fully non-linear analysis was developed by Freund and co-workers [55, 57]. This model is based on the solution of the Maxwell and the Newton-Lorentz equations that self-consistently describe the spatio-temporal evolution of both the electrons and the electromagnetic wave when co-propagating through the interaction region. In this model the small-signal (linear) regime of wave amplification, and the strong-signal (non-linear) growth and saturation at maximum output are contained.

There are two types of gain regimes in a CFEL, depending on the strength of the pumping current density of the electron beam. For sufficiently large electron current densities, the Coulomb repulsion among the electrons, known as the space-charge effect, is non-negligible and induces longitudinal waves oscillating at the plasma frequency. This collective effect is negligible if the number of space-charge oscillations executed is small compared with unity, which is called the single-particle regime or Compton regime. When the named space-charge effect is non-negligible, the CFEL is said to operate in the Raman regime [40, 62, 56, 63].

Regarding the type of waveguide used in the CFEL, there are a number of possibilities such as a single or a double slab [49, 64, 65], a rectangular waveguide, and a circular waveguide

[46, 47, 48, 52, 66, 67]. In general, a planar surface is easier to manufacture and coat with the dielectric liner material but the circular geometry is better adapted to electron beams with circular cross-section, which are more common in the experiments.

The model described in the present section describes the non-linear interaction between the electrons and the wave within the Compton regime, using in a cylindrical waveguide lined with a dielectric material as the gain section. First, we present the main concepts of generation of Čerenkov radiation, when electrons travel near the liner of the waveguide. Next, we describe the propagation of the electromagnetic field in the dielectric-lined cylindrical waveguide. Finally, we study the interaction between these modes and the electrons, and illustrate the results from the model with a numerical example.

2.1.1 Čerenkov radiation

In the 1930s, P. A. Čerenkov (1904-1990) performed extensive experimental investigations of the faint bluish light emitted by pure liquids when exposed to gamma rays [68, 69]. He soon realized that the light was caused by quickly moving electrons ejected from the atoms of the liquid. After recognizing that the key to understanding Čerenkov's observations was that the charged particles were moving with a speed greater than the speed of light in the material, Frank and Tamm gave a theoretical description of this phenomenon [70] based on classical electromagnetism in excellent agreement with experimental results. In honour of Čerenkov's discoveries, the radiation produced is now called Čerenkov radiation. An extensive discussion of the phenomenon and reference to most of the early work is given by Jelly [71]. Here, following the description of Jelly, we comment on the most relevant aspects of the Čerenkov radiation that are useful for our description of the CFEL.

The Čerenkov radiation is a response of a medium to the Coulomb field of an incident charged particle. When an electron travels through a material, it transiently polarizes the medium in a volume around the electron along its trajectory and, as a response, the polarized atoms radiate like elementary dipoles. For an electron moving well below relativistic velocity, the polarization field surrounding the electron is symmetric and, therefore, no resultant propagating field is generated at large distances. However, for an electron moving at a velocity comparable to that of light in the medium, the polarization field along the trajectory of the electron becomes asymmetric, which results in a non-zero dipole moment and, therefore, a radiation pulse. Essentially, the wave fronts from the different points of the trajectory interfere constructively, resulting in an electromagnetic field sent off under a specific angle of observation. The angle of observation of Čerenkov radiation for an electron travelling at a velocity v through a material with a refraction index n can be inferred geometrically as shown in figure 2.1. The figure shows the trajectory of the electrons from A to B and one can see that, for a particular

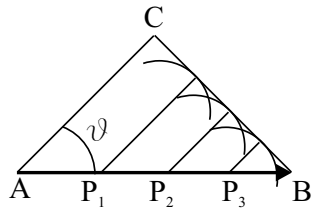

Figure 2.1: The electron travels in from A to B within a material faster than light in this material. The wavelets from points P_1, P_2, $P_3 \ldots$ of the trajectory interfere constructively for a certain observation angle θ.

angle θ, the wavelets from arbitrary Čerenkov emitting points P_1, P_2 and P_3 interfere constructively and form the wavefront BC. This occurs if the time $\Delta\tau$ in which the electrons travel a distance AB, *i.e.,* $AB/\beta c_0$, is equal to the time it takes the light to travel a distance AC, *i.e.,* $n\,AC/c_0$. By equating both expressions, we have that the angle of emission is given by

$$\cos\theta = \frac{1}{\beta n} \tag{2.1}$$

Here $\beta = v/c_0$, where c_0 is the speed of light in vacuum. From equation (2.1) one can derive the threshold velocity of the electrons $\beta_t = 1/n$ below which no radiation occurs, which is equal to the the phase velocity of the wave in the medium. In principle, all media in which the refractive index is larger than unity, such as gases, liquids and solids, are suitable for Čerenkov emission. However, in the case of gases, the refractive index is rather close to unity. Therefore, Čerenkov emission in gases is only observed when the electrons travel with velocities very close to c_0. In liquids and solids, to generate pure Čerenkov radiation, the electrons need to travel at highly relativistic velocities as well because otherwise the Čerenkov radiation can be masked by other types of emission, *e.g.*, Bremsstrahlung. To generate pure Čerenkov radiation, the electron beam can also be driven through vacuum in close proximity to a solid dielectric material. Although the electron is not travelling inside the medium, the electric field of the charged particle still does, with the subsequent emission of Čerenkov radiation. When the electrons travel near the surface of a dielectric material, the strenth of the emission decreases with increasing distance between the electrons and the surface [72], but for sufficient proximity between the electrons and the solid, even mildly relativistic velocities are well sufficient to generate Čerenkov emission. This situation was analysed theoretically by Danos [73] for a flat electron beam near a flat dielectric sheet and for a cylindrical electron beam within a cylindrical hole in a dielectric material. Later, he conducted corresponding experimental work [42] and these experiments became the first demonstration of generating microwave radiation with an electron beam. An adapted version of the set-up used by Danos is used nowadays in modern CFELs, where the electrons travel parallel to a dielectric material.

2.1.2 Electromagnetic fields in the waveguide

In the present section we describe a most essential ingredient for a CFEL, which is the propagation of electromagnetic modes in the so-called cold waveguide of the CFEL, *i.e.*, the waveguide when the electron beam is not present. Figure 2.2 shows such a waveguide of cylindrical shape made of metal with an inner radius r_g, lined with a dielectric material with inner radius r_d. In this waveguide two regions can be defined, namely, the vacuum region of permittivity ϵ_0, for radii less than r_d and the dielectric region of permittivity ϵ, for radii between r_d and r_g. The magnetic permeability is equal to the vacuum permeability μ_0 in both regions. We assume here that ϵ is real, *i.e.*, the liner has no dielectric losses, although later this assumption will be given up (section 2.2) for the description of more realistic CFELs. For the moment we also assume homogeneity of the dielectric properties in both regions, thus, we can write within each of them $\vec{\nabla}\epsilon = 0$. Again, later this simplistic approach is given up in order to include the more realistic case when, *e.g.,* the thickness of the liner somewhat fluctuates along the interaction length (section 2.3). The properties of the electromagnetic fields propagating in the cold waveguide can be derived from Maxwell's equations, which for the vacuum and for the dielectric regions of the waveguide shown in figure 2.2 can be written as

$$\begin{aligned} \vec{\nabla} \times \vec{E} + \frac{\partial \vec{B}}{\partial t} &= 0 \\ \vec{\nabla} \times \vec{H} - \epsilon \frac{\partial \vec{E}}{\partial t} &= 0 \\ \vec{\nabla} \cdot \vec{D} &= 0 \\ \vec{\nabla} \cdot \vec{B} &= 0. \end{aligned} \tag{2.2}$$

Here $\vec{D} = \epsilon \vec{E}$ is the displacement vector and $\vec{H} = \frac{1}{\mu_0}\vec{B}$ is the magnetic induction. By considering time-harmonic fields of frequency ω, one derives from the Maxwell equations the following wave equation for the fields

$$\left(\vec{\nabla}^2 + \epsilon_r \frac{\omega^2}{c_0^2}\right) \left\{ \begin{array}{c} \vec{E}(\vec{r}) \\ \vec{B}(\vec{r}) \end{array} \right\} = 0 \tag{2.3}$$

where $\epsilon_r = \epsilon/\epsilon_0$ and $c_0 = 1/\sqrt{\epsilon_0 \mu_0}$. Equation (2.3) possesses an infinite number of solutions, known as modes of the cold waveguide, and the general solution is given by a superposition of these modes. For a cylindrical coordinate system as the one shown in figure 2.2, the modes can be written as transverse eigenmodes depending on r and on θ, and which propagate along z with a wavenumber k_{zn}, where n denotes the mode number. Due to the symmetry of the waveguide, we only consider azimuthally symmetric eigenmodes which depend only on r and not on θ. This implication of symmetry divides the propagating modes in two distinct sets, namely, modes with a zero longitudinal component for the magnetic field, called transverse

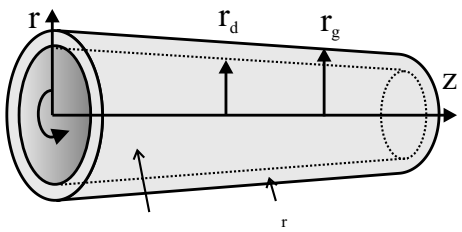

Figure 2.2: Dielectric-lined waveguide used for the CFEL interaction. The inner liner radius is r_d and the waveguide radius is r_g.

magnetic or TM_{0n} modes, and modes with a zero longitudinal component for the electric field, called transverse electric or TE_{0n} modes. In the CFEL, an amplification of the field by the longitudinally travelling electrons occurs only for the longitudinal component of the electric field. Therefore, only the TM_{0n} modes are of interest for a CFEL. Further, the electrons are to interact with the forward propagating wave in the waveguide, so only a positive phase velocity of the fields along the z-direction is considered. With these assumptions, the solutions of (2.3) of interest are:

$$\begin{aligned} \vec{E}(\vec{r},t) = &\ \sum_{n=1}^{\infty} \mathrm{Re}\left(\vec{\mathcal{E}}_n(r)\ A_n\ e^{i(k_{zn}z-\omega t)}\right) \\ \vec{B}(\vec{r},t) = &\ \sum_{n=1}^{\infty} \mathrm{Re}\left(\vec{\mathcal{B}}_n(r)\ A_n\ e^{i(k_{zn}z-\omega t)}\right) \end{aligned} \tag{2.4}$$

where A_n is the field amplitude of the nth mode and $\vec{\mathcal{E}}_n(r)$ and $\vec{\mathcal{B}}_n(r)$ are the TM_{0n} transverse eigenmodes, which are derived in appendix A and given by

$$\vec{\mathcal{E}}_n = \begin{pmatrix} -i\frac{k_{zn}}{\kappa_n} J_1(\kappa_n r) \\ 0 \\ J_0(\kappa_n r) \end{pmatrix} \qquad \vec{\mathcal{B}}_n = \begin{pmatrix} 0 \\ -i\frac{\omega}{\kappa_n c_0^2} J_1(\kappa_n r) \\ 0 \end{pmatrix} \tag{2.5}$$

for the region $0 \leq r \leq r_d$, and by

$$\vec{\mathcal{E}}_n = \begin{pmatrix} -i\frac{k_{zn}}{\kappa_n'}(a_n J_1(\kappa_n' r) + b_n Y_1(\kappa_n' r)) \\ 0 \\ a_n J_0(\kappa_n' r) + b_n Y_0(\kappa_n' r) \end{pmatrix} \qquad \vec{\mathcal{B}}_n = \begin{pmatrix} 0 \\ -i\frac{\omega\epsilon_r}{\kappa_n' c_0^2}(a_n J_1(\kappa_n' r) + b_n Y_1(\kappa_n' r) \\ 0 \end{pmatrix} \tag{2.6}$$

for the region $r_d < r \leq r_g$. The constants a_n and b_n are defined by equations (A.12) in appendix A. The functions J and Y are Bessel's functions of the first and second kind, respectively. Finally, κ_n is the transverse wavenumber for the vacuum region and κ_n' the transverse wavenumber

for the dielectric region, which are related to the longitudinal wavenumber k_{zn} by

$$\begin{aligned} {\kappa_n}^2 &= \tfrac{\omega^2}{c_0^2} - k_{zn}^2 \\ {\kappa'_n}^2 &= \epsilon_r \tfrac{\omega^2}{c_0^2} - k_{zn}^2. \end{aligned} \tag{2.7}$$

For the description of amplification of these modes it is required to find the relation between the phase velocity and frequency of these modes which is called the dispersion relation. This is possible with the physical properties of the waveguide, such as the radii and the dielectric constant of the liner. The derivation of the dispersion of the modes is given in appendix A, and for the TM_{0n} modes one obtains

$$J_1(\kappa_n r_d)W + \frac{\kappa_n \epsilon_r}{\kappa'_n} J_0(\kappa_n r_d)X = 0. \tag{2.8}$$

Here W, X are combinations of Bessel functions defined by equations (A.8) in appendix A. Figure 2.3 shows a graphical representation of the dispersion relation (2.8) for $n = 1$ and for a lined waveguide with r_d=1.5 mm, r_g=2.8 mm and ϵ_r=5.8. The figure also shows a line with unity slope and a line with slope $1/\sqrt{\epsilon_r}$, which represent a plane wave travelling in vacuum and a plane wave travelling in a medium of relative dielectric constant ϵ_r, respectively. It is possible to derive some properties of the CFEL interaction from figure 2.3. For this purpose, figure 2.3 also shows the so called electron beam line, given by a line with slope equal to the normalized electrons velocity β_z. It turns out that the amplification process requires a synchronism between the phase velocity of the wave and the velocity of the electrons, which corresponds to the point in the graph where the electron beam line and the TM_{01} mode line cross each other. It can clearly be seen that just by varying the speed of the electrons, *i.e.*, the slope of the electron beam line, the crossing point moves along the model line, thereby it is possible to tune the frequency of amplification of the CFEL via the velocity of the electrons. In particular it can be seen that lowering the electron velocity tunes the frequency of the amplified wave towards higher values. Alternatively, for a fixed electron beam velocity, lowering the dielectric constant, decreasing the liner thickness or decreasing the transverse dimensions of the waveguide, tunes the CFEL to higher operating frequencies.

We have seen in section 2.1.1 that the emission of Čerenkov radiation occurs for velocities of the electrons above a threshold velocity given by $\beta_t = 1/\sqrt{\epsilon_r}$. In figure 2.3 this condition translates into a lower limit to the slope of the electron beam line and, equivalently, limits the amplification to frequencies such that $\omega^2/c_0^2 > k_{zn}^2/\epsilon_r$. By using equations (2.7), this condition corresponds to ${\kappa'_n}^2 > 0$ and, therefore, the transverse wavenumber in the liner remains real. A second condition is given by the upper limit in the velocity of the electrons given by c_0. This limits the slope of the electron beam line to less that unity or, equivalently, limits the

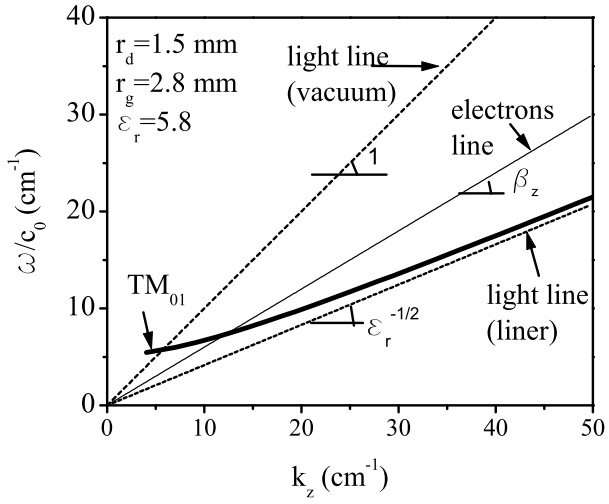

Figure 2.3: Dispersion relation for the TM_{01} mode in the dielectric-lined cylindrical waveguide. The light and the electron beam lines are also represented. The inner radius of the liner is r_d =1.5 mm, the outer radius of the liner is r_g=2.8 mm, and the dielectric constant is ϵ_r=5.8.

interaction to frequencies such that $\omega^2/c_0^2 < k_z^2$. By using (2.7), this condition implies that ${\kappa_n}^2 < 0$, *i.e.*, the transverse wavenumber in vacuum becomes imaginary. Thus, these two conditions on the velocity of the electrons limit also the velocities of the waves that can be amplified and, specifically, to be amplified the wave must travel slower than c_0. For this reason the CFEL is also referred to as a slow-wave device. The transverse wavenumber in vacuum κ_n, which is found to be imaginary, appears in the argument of the Bessel function of the transverse eigenmodes in vacuum. For convenience, one can define $\kappa_n^r = -i\kappa_n$ and use the properties of Bessel functions[1] such that the eigenmode takes the form $J_0(\kappa_n r) = J_0(i\kappa_n^r r) = I_0(\kappa_n^r r)$. The function I_0 decays with r and, therefore, the transverse eigenmode is an evanescent wave tailing off from the dielectric surface into the vacuum region. The decay distance $L_\perp$ of this evanescent wave is $L_\perp \approx 1/|\kappa_n|$, which, when synchronous with the electron beam, can be written as

$$L_\perp = \frac{c_0}{\omega}\sqrt{\gamma^2 - 1} \tag{2.9}$$

where $\gamma = 1/\sqrt{1-\beta_z^2}$ is the energy of the electrons. Only those electrons travelling at a distance closer than $L_\perp$ to the liner can exchange energy and contribute to the wave amplification. Specifically, equation (2.9) shows that higher frequencies have a shorter decaying distance so, to amplify high frequencies, the electron beam has to travel in close proximity to the liner. For a fixed frequency to be amplified, equation (2.9) means that the decay distance increases for

[1] $J_p(ix) = i^p I_p(x)$, with I_p the modified Bessel function of first kind of order p [74]

a higher energy of the electron beam. The result is a stronger interaction between the electrons and the radiation wave for relativistic Čerenkov devices (high γ) than for their weakly relativistic counterparts.

2.1.3 CFEL dynamics

In this section, we consider the interaction between an electromagnetic field propagating in the waveguide as in figure 2.2 with an electron beam of current density $\vec{J}$ injected at a relativistic speed along the axis of the same waveguide. The dynamics of the electromagnetic field are described by Maxwell's equations with the electron current as the source term, and the dynamics of the electrons under the action of the electromagnetic field are described by the Newton-Lorentz equations. The interchange of energy $\delta\mathcal{W}$ between the electrons and the electromagnetic field propagating in the waveguide is given as

$$\delta\mathcal{W} = \int_V dV\, \vec{J}\cdot\vec{E} \tag{2.10}$$

where the integral is extended over the entire volume of the waveguide. Since the electron current $\vec{J}$ is primarily directed along z, the integral (2.10) is non-zero only for modes for which $E_z \neq 0$ and, therefore, confirming that only the TM_{0n} modes are amplified or deamplified, via a bunching of the electrons and subsequent stimulated emission. Thus, the CFEL particle-field dynamics is obtained by solving the self-consistent set of equations formed by the Maxwell and the Newton-Lorentz equations and the gain of electromagnetic energy via this process is given by calculating the energy balance via (2.10).

To solve the set of equations, we assume that the propagating modes in the waveguide with the electron beam present are the same as the modes in the cold waveguide, however, with an amplitude and a phase that may change along the longitudinal direction z:

$$\begin{aligned} \vec{E}(\vec{r},t) &= \textstyle\sum_{n=1}^{\infty} \mathrm{Re}\left(\vec{\mathcal{E}}_n(r)\, \tilde{A}_n(z)\, e^{i(k_{zn}z-\omega t)}\right) \\ \vec{B}(\vec{r},t) &= \textstyle\sum_{n=1}^{\infty} \mathrm{Re}\left(\vec{\mathcal{B}}_n(r)\, \tilde{A}_n(z)\, e^{i(k_{zn}z-\omega t)}\right) \end{aligned} \tag{2.11}$$

Here, $\vec{\mathcal{E}}_n(r)$ and $\vec{\mathcal{B}}_n(r)$ are the transverse eigenmodes given by (2.5) and (2.6) and $\tilde{A}_n(z) = A_n(z)\, e^{i\phi_n(z)}$ is the complex amplitude of the field. The magnitude of the complex wave amplitude, $|\tilde{A}_n(z)|$ describes the amplification or damping, while the phase of the complex amplitude, $\phi_n(z)$, describes phase changes of the field as a result of the interaction with the electrons.

To calculate the amount of energy gained by the field after the interaction with the electron beam, requires to determine the power carried by the modes. The power flow P is given by

the flux of the time average of the Poynting vector $\vec{\Pi} = \vec{E} \times \vec{H}$ over the cross section S of the waveguide, which can be written as

$$P = \left\langle \iint_S dS\,(\vec{E} \times \vec{H}) \cdot \hat{z} \right\rangle =$$
$$= \frac{1}{2\mu_0} Re \left[\iint_S dS \left(\sum_n |A_n(z)|^2 \vec{\mathcal{E}}_n \times \vec{\mathcal{B}}_n^* + \sum_{n \neq m} |A_n(z)||A_m(z)| \vec{\mathcal{E}}_n \times \vec{\mathcal{B}}_m^* \right) \cdot \hat{z} \right] \quad (2.12)$$

In this expression, the power orthogonality property of the modes [75] ensures that the flux of the cross terms of the fields is zero. Therefore, the power of a set of modes propagating in the waveguide can be calculated as the sum of the powers P_n carried by each individual mode, $P = \sum_n P_n$. For the TM_{0n} modes given in equations (2.4)-(2.6) the power P_n carried by mode n is given by

$$P_n = \frac{1}{2\mu_0} Re \left(|A_n(z)|^2 \mathcal{N}_n \right) \quad (2.13)$$

where we have defined the normalization constant $\mathcal{N}_n$ as

$$\mathcal{N}_n = \iint_S dS\ \mathcal{E}_{rn} \mathcal{B}_{\theta n}^* \quad (2.14)$$

To find how the electron beam current drives the complex amplitudes of the modes propagating through the waveguide, in the following, we insert the modes given by equations (2.11) in the Maxwell equations where the source term is given by the electron beam current. Then, the solution obtained for the fields is inserted into the Newton-Lorentz equation to calculate the orbits and velocities of the electrons.

Wave dynamics

For each of the two regions of the waveguide, namely, the vacuum and the dielectric regions, the wave equation in the presence of a source $\vec{J}$ can be written as

$$\vec{\nabla}^2 \vec{B} - \frac{\epsilon_r}{{c_0}^2} \frac{\partial^2 \vec{B}}{\partial t^2} = -\mu_0 \vec{\nabla} \times \vec{J} \quad (2.15)$$

with $\vec{J} = (J_r, J_\theta, J_z)$ the current density of the electron beam. Implicitly equation (2.15) assumes that the potential associated with the electron beam space-charge waves is negligible so the description is limited to the Compton regime. For the set of monochromatic TM_{0n} modes described by equations (2.11) and after executing time and transverse derivatives for each mode,

we can write equation (2.15) separately for each of the two regions as

$$\sum_{n=1}^{\infty}(\epsilon_r\frac{\omega^2}{{c_0}^2}-\kappa_n^2+\frac{\partial^2}{\partial z^2})\mathrm{Re}\left(\mathcal{B}_{\theta n}\tilde{A}_n(z)e^{i(k_{zn}z-\omega t)}\right)=\mu_0(\frac{\partial J_z}{\partial r}-\frac{\partial J_r}{\partial z}). \tag{2.16}$$

In the dielectric region the current density $\vec{J}$ is assumed to be zero because electrons that may hit the liner can be considered as lost from the electron beam. We further assume that the complex field amplitude, $\tilde{A}_n(z)$ follows the slowly-varying envelope approximation (SVEA), meaning that both the amplitude and the phase vary only slowly over one wavelength of the radiation. With this approximation, the second order derivatives in z of the complex amplitude can be neglected, so that

$$\frac{\partial^2\tilde{A}_n(z)e^{i(k_{zn}z-\omega t)}}{\partial z^2}\approx\left[2ik_{zn}\frac{d\tilde{A}_n(z)}{dz}-k_{zn}^2\tilde{A}_n(z)\right]e^{i(k_{zn}z-\omega t)}. \tag{2.17}$$

Making use of (2.17) and of the relations (2.7), we can rewrite the expression (2.16) for each of the two regions as

$$\sum_{n=1}^{\infty}\mathrm{Re}\left(2ik_{zn}\frac{d\tilde{A}_n(z)}{dz}\mathcal{B}_{\theta n}e^{i(k_{zn}z-\omega t)}\right)=\mu_0(\frac{\partial J_z}{\partial r}-\frac{\partial J_r}{\partial z}). \tag{2.18}$$

For convenience, by using the properties of complex numbers[2] and by multiplying equation (2.18) by $e^{-i(k_{zn}z-\omega t)}$ one obtains

$$\sum_{n=1}^{\infty}ik_{zn}\frac{d\tilde{A}_n(z)}{dz}\mathcal{B}_{\theta n}+\left(ik_{zn}\frac{d\tilde{A}_n(z)}{dz}\mathcal{B}_{\theta n}\right)^*e^{-2i(k_{zn}z-\omega t)}=\mu_0\,(\frac{\partial J_z}{\partial r}-\frac{\partial J_r}{\partial z})\,e^{-i(k_{zn}z-\omega t)}. \tag{2.19}$$

Within the SVEA approximation, the field amplitude changes slowly over one period of the wave. Correspondingly, the current density $\vec{J}$, which is driven by the field, and its spatial derivatives experience only a slow variation over one period as well. Thus, one can apply a temporal average to simplify equation (2.19). Since the second term in the *lhs* of the equation oscillates rapidly such that the average over one period vanishes, one can write

$$\sum_{n=1}^{\infty}\frac{d\tilde{A}_n(z)}{dz}\mathcal{B}_{\theta n}=-\frac{i\mu_0\omega}{2\pi k_{zn}}\int_0^{\frac{2\pi}{\omega}}dt\;e^{-i(k_{zn}z-\omega t)}\;(\frac{\partial J_z}{\partial r}-\frac{\partial J_r}{\partial z}). \tag{2.20}$$

The expressions (2.20) is a sum over all modes of the waveguide. To separate out one mode, we multiply both sides of (2.20) by $\mathcal{E}_{rm}^*$ and we integrate over the cross section of the waveguide.

[2]for $z\in\mathbb{C}$, $\mathrm{Re}(z)=(z+z^*)/2$

We obtain two equations, one for each of the two regions, which we add up for obtaining a single equation. By using the power orthogonality of the modes [75], one obtains for the single nth mode

$$\frac{d\tilde{A}_n(z)}{dz} = -\frac{i\mu_0\omega}{k_{zn}\mathcal{N}_n^*}\int_0^{\frac{2\pi}{\omega}} dt\, e^{-i(k_{zn}z-\omega t)}\int_0^{r_d} r\, dr\, (\frac{\partial J_z}{\partial r} - \frac{\partial J_r}{\partial z})\, \mathcal{E}_{rn}^*, \tag{2.21}$$

where we have used the normalization constant defined in (2.14). It is convenient for numerical purposes to modify the expressions inside the integral on the *rhs* of the equation (2.21) by removing the partial derivatives. For that, we observe that the electron current density is rapidly modulated with the phase of the field but only slowly modulated by the varying field amplitude, so that one can write the electron current density J_i for each electron i with a functional dependence given by

$$J_i(\vec{r},t) = f(z)f_i(k_{zn}z - \omega t). \tag{2.22}$$

Here $f(z)$ describes the slow variation in the electron beam current along z as a consequence of the growth or damping of the wave amplitude and $f_i(k_{zn}z-\omega t)$ describes the rapid variation of the electron beam current along z due to the change in the phase of the wave. From (2.22) we can write

$$\frac{\partial J_i}{\partial z} = f_i\frac{df}{dz} + k_{zn}\frac{\partial f_i}{\partial z} \tag{2.23}$$

$$\frac{\partial J_i}{\partial t} = -\omega f\frac{\partial f_i}{\partial t} \tag{2.24}$$

Applying again the SVEA approximation in equation (2.23), the first term on the *rhs* becomes much smaller than the second term. Then it follows that

$$\frac{1}{k_{zn}}\frac{\partial J}{\partial z} \approx -\frac{1}{\omega}\frac{\partial J}{\partial t}. \tag{2.25}$$

Note that the relation (2.25) expresses that the electrons velocity is approximately equal to the phase velocity of the wave, *i.e.,* a synchronism between the wave and the electrons. This can only be fulfilled for a slow-wave device for which the phase velocity of the propagating wave is lower than c_0. Thus for slow-wave devices, the radial and temporal integrals on the *rhs* of equation (2.21) can be transformed with integration by parts. This yields the following relations.

$$\begin{aligned} \int_0^{r_d} r\, dr\, \tfrac{\partial J_z}{\partial r}\mathcal{E}_r^* &= -\int_0^{r_d} dr\, J_z(r\tfrac{d\mathcal{E}_r^*}{dr} + \mathcal{E}_r^*) \\ \int_0^{\frac{2\pi}{\omega}} dt\, \tfrac{\partial J_r}{\partial t}e^{-i(k_{zn}z-\omega t)} &= -i\omega\int_0^{\frac{2\pi}{\omega}} dt\, J_r e^{-i(k_{zn}z-\omega t)}. \end{aligned} \tag{2.26}$$

By substituting expressions (2.26) in equation (2.21) one obtains

$$\frac{d\tilde{A}_n(z)}{dz} = -\frac{i\omega\mu_0}{k_{zn}\mathcal{N}_n^*}\int_0^{\frac{2\pi}{\omega}} dt\, e^{-i(k_{zn}z-\omega t)}\int_0^{rd} dr\ \left(J_z(r\frac{d\mathcal{E}_r^*}{dr}+\mathcal{E}_r^*)+irk_{zn}J_r\mathcal{E}_r^*\right) \tag{2.27}$$

To evaluate the wave amplitude from this expression, one requires to specify the current density, $\vec{J}$, that drives the amplitude. To specify the current density, we consider a monochromatic electron beam in which each electron travels with velocity $\vec{v}_j(\vec{r},t)$. With an electron density n_b, a length L and a total number of electrons N_T, the current density can be expressed as the sum of the individual currents associated with each electron,

$$\vec{J}(\vec{r},t) = -en_b\frac{L}{N_T}\sum_{j=1}^{N_T}\frac{\vec{v_j}(\vec{r},t)}{|v_{zj}(\vec{r},t)|}\delta(t-t_j(z)) \tag{2.28}$$

where $t_j(z)$ is the time at position z. By substituting (2.28) in equation (2.27), the evolution of the field amplitude becomes

$$\begin{aligned}&\frac{d\tilde{A}_n(z)}{dz} = \\ &= \frac{i\mu_0\omega}{k_{zn}\mathcal{N}_n^*}(-\frac{en_bL}{N_T})\int_0^{\frac{2\pi}{\omega}} dte^{-i(k_{zn}z-\omega t)}\int_0^{r_d} dr\sum_{j=1}^{N_T}\Big[\delta(t-t_j(z))(r\frac{d\mathcal{E}_{rn}^*}{dr}+\mathcal{E}_{rn}^*)+ \\ &+irk_{zn}\frac{v_{rj}}{|v_{zj}|}\delta(t-t_j(z))\mathcal{E}_{rn}^*\Big].\end{aligned} \tag{2.29}$$

The time integral is extended over one wave period and, therefore, the summation over the total number of electrons of the beam is now limited to those electrons in one wave spatial period $N_\omega = (2\pi N_T v_{z0})/(\omega L)$. For a more compact notation, we abbreviate over the number of electrons within one spatial period of the electromagnetic wave as

$$\langle\cdots\rangle = \frac{1}{N_\omega}\sum_{j=1}^{N_\omega}\cdots. \tag{2.30}$$

Finally, equation (2.29) is scaled to obtain a dimensionless amplitude with the definition $\tilde{a}_n(z) = \frac{e}{m_e c_0}\tilde{A}_n(z)$ as

$$\frac{d\tilde{a}_n(z)}{dz} = -\frac{2i\pi\omega_p^2\beta_{z0}}{k_{zn}c_0^2\mathcal{N}_n^*}\int_0^{r_d} dr\ \left[\left\langle e^{-i\alpha_{nj}(z)}\right\rangle(r\frac{d\mathcal{E}_{rn}^*}{dr}+\mathcal{E}_{rn}^*)+irk_{zn}\left\langle\frac{\beta_r}{|\beta_z|}e^{-i\alpha_{nj}(z)}\right\rangle\mathcal{E}_{rn}^*\right]. \tag{2.31}$$

Here, $\omega_p^2 = n_b e^2/m_e\epsilon_0$ is the squared plasma frequency of the electron beam, $\beta_{z0} = v_{z0}/c_0$ is the normalized initial velocity of the electrons, and $\alpha_{nj} = k_{zn}z - \omega t_j$ is the relative phase

at the moment t_j between the electron j and the *nth* mode of the cold waveguide. The term $\langle e^{-i\alpha_{nj}} \rangle$ is the average of these relative phases taken over all the electrons within one wave period and is known as the so-called complex bunching term. Expression (2.31) still contains a general expression of the transverse eigenmodes, however, for the cylindrical, lined waveguide described above, one can specify the spatial field distribution by substituting (2.5) into (2.31). Further, we showed in section 2.1.2 that the transverse wavenumber is imaginary, and a real wavenumber can be defined as $\kappa_n^r = -i\kappa$. With these specifications, equation (2.31) assumes the form

$$\frac{d\tilde{a}_n(z)}{dz} = \frac{2\pi\omega_p^2\beta_{z0}}{c_0^2\mathcal{N}_n^*} \int_0^{r_d} r\,dr \left[\left\langle e^{-i\alpha_{nj}} \right\rangle I_0(\kappa_n^r r) + i\frac{k_{zn}}{\kappa_n^r} \left\langle \frac{\beta_r}{|\beta_z|} e^{-i\alpha_{nj}} \right\rangle I_1(\kappa_n^r r) \right]. \qquad (2.32)$$

The result obtained here is equivalent to the result obtained by Freund and Ganguly [57]. However, to describe the amplification or damping of the field amplitude, Freund and Ganguly use a real amplitude, and to describe the phase change of the field as a result of the interaction with the electron beam, they use a wavenumber varying along the propagation direction. As a result, they obtain separate equations for the evolution of the amplitude and of the phase of the field as effect of the interaction with the electrons. In the model presented here, the complex field amplitude, $\tilde{a}(z)$, contains both a varying amplitude and a varying phase, and thus the evolution of the field can be described with a single equation. The advantage of our notation is that the phase changes related to the interaction with the electrons are described by the phase term of the complex amplitude, and other phase changes related to the liner, *e.g.,* the dielectric losses and the liner radius fluctuations, can be described by variations of the wavenumber. We treat these cases in sections 2.2 and 2.3.

Electron beam dynamics

The transfer of energy from the electrons to the field, or vice versa, depends on the relative phases between the wave and each of the electrons, which is given by $\Phi_{nj}(z) = \alpha_{nj}(z) + \phi_n(z)$. The evolution of the relative phases between the electrons and the wave is given by

$$\frac{d\Phi_{nj}}{dz} = k_{zn}(1 - \frac{v_{\Phi n}}{v_{zj}}) + \frac{d\phi_n(z)}{dz} \qquad (2.33)$$

where $v_{\Phi n}$ is the phase velocity of the nth mode, and v_{zj} is the longitudinal velocity component of the jth electron. Therefore, to determine the relative phases between the electrons and the wave, and thus the energy transfer in a CFEL, one needs to know the dynamics of the electrons.

The evolution of the momentum $\vec{p} = \gamma m\vec{v}$ and energy $\mathcal{U} = \gamma mc_0^2$ of the electrons under the

action of the fields $\vec{E}$ and $\vec{B}$ is governed by the Newton-Lorentz equations

$$\begin{aligned} \frac{d\gamma m\vec{v}}{dt} &= -e(\vec{E} + \vec{v} \times \vec{B}) \\ \frac{d\gamma mc_0^2}{dt} &= -e\vec{v} \cdot \vec{E} \end{aligned} \tag{2.34}$$

The magnetic field used in equation (2.34) may include an external static magnetic field for electron beam transport. For convenience, we separate the equations (2.34) into the various cylindrical components of the velocity of the electrons. For this, we use $d/dt = v_z d/dz$ where v_z is the longitudinal velocity component of the electrons and $\vec{\beta} = \vec{v}/c_0$

$$\begin{aligned} \frac{\mathrm{d}\beta_r}{\mathrm{d}z} &= -\frac{e}{\gamma mc^2}\left\{\frac{E_r}{\beta_z} + c\left(\frac{\beta_\theta}{\beta_z}B_0 - B_\theta\right) - \frac{\beta_r}{\beta_z}\left(\beta_r E_r + \beta_z E_z\right)\right\} \\ \frac{\mathrm{d}\beta_\theta}{\mathrm{d}z} &= \frac{e}{\gamma mc^2}\left\{c\frac{\beta_r}{\beta_z}B_0 + \frac{\beta_\theta}{\beta_z}\left(\beta_r E_r + \beta_z E_z\right)\right\} \\ \frac{\mathrm{d}\beta_z}{\mathrm{d}z} &= -\frac{e}{\gamma mc^2}\left\{\frac{E_z}{\beta_z} + c\frac{\beta_r}{\beta_z}B_\theta - \left(\beta_r E_r + \beta_z E_z\right)\right\}, \end{aligned} \tag{2.35}$$

where B_0 is the homogeneous static magnetic field used to transport the electron beam.

The complete description of the CFEL contains thus the dynamics of the electromagnetic field, described in section 2.1.3, and the dynamics of the electron beam, described in the present section. In the following we present a numerical example and the physical interpretation of the dynamical CFEL equations.

2.1.4 Interpretation of the equations and numerical example

To this end we have described the propagation of the wave in the waveguide of the CFEL, by expanding the field as a superposition of the TM_{0n} modes of the cold waveguide but allowing for a z-dependent amplitude $a_n(z)$ and phase $\phi_n(z)$, which are both driven by the interaction with the electron beam. By making use of Maxwell's equations and the Lorentz-Newton equations we have derived explicit equations, for the evolution of the complex field amplitude (equation (2.32)) and for the evolution of the velocity of the electrons (equations (2.35)). Together, these equations should describe the dynamics of the CFEL for a wide range of physical parameters. In this section, we further analyse these dynamical equations in order to present a more intuitive picture of the dynamics of the CFEL.

The evolution of the field amplitude is given by equation (2.32), in which, to simplify, we can assume $\beta_r \ll \beta_z$, *i.e.*, the transverse velocity of the electrons is much smaller than the longitudinal velocity of the electrons. This assumption is justified since the electron beam moves parallel to the axis of the lined waveguide. This allows us to neglect the second term on the *rhs* of equation (2.32). As an abbreviation of the notation we introduce a factor F, which

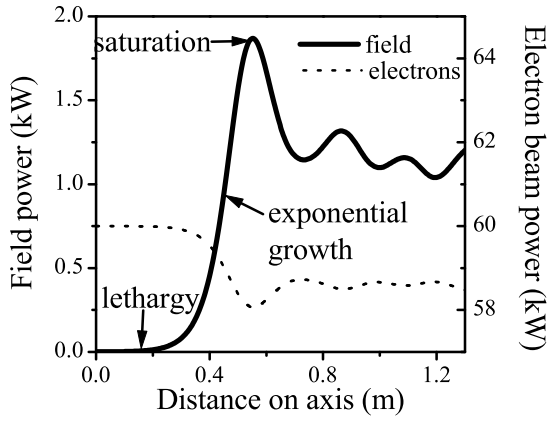

Figure 2.4: Electromagnetic wave and electron beam power along the propagation axis of the waveguide for a frequency of 50 GHz, an accelerating voltage of the electrons of 75 kV and an electron beam current of 800 mA. The inner radius of the liner is r_d =1.5 mm, the outer radius of the liner is r_g=2.8 mm and the dielectric constant is ϵ_r=5.8.

is proportional to the total electron beam and which scales with the transverse spatial overlap between the field and the current density. With this pump overlap factor, equation (2.32) can be written as

$$\frac{d\tilde{a}_n(z)}{dz} = F\left\langle e^{-i\alpha_{nj}(z)}\right\rangle . \tag{2.36}$$

It can be seen in equation (2.36) that the evolution of the complex amplitude is driven by the complex bunching term $\left\langle e^{-i\alpha_{nj}(z)}\right\rangle$. The bunching term represents an average of the relative phases α_{nj} that each electron j assumes respect to the nth mode. As an illustration, if the electrons are evenly spaced within the wave period, the contributions of the individual electron phases to $\left\langle e^{-i\alpha_{nj}(z)}\right\rangle$ cancels such that the bunching of a homogeneous electron beam is zero. Contrary to this, $\left|\left\langle e^{-i\alpha_{nj}(z)}\right\rangle\right|$ is maximum when the electrons assume the same relative spatial phase with respect to the wave. In this case the electron beam is said to be perfectly bunched.

Equation (2.36) describes the evolution of the complex field amplitude, so contains the evolution of both the amplitude and phase of the field. The physical interpretation can be done in a more simple way by using separate equations for the evolution of the amplitude and of the phase of the field. For this, we split equation (2.36) into real and imaginary parts as

$$\frac{da_n(z)}{dz} = F\left\langle \cos\left(\alpha_{nj}(z)+\phi_n(z)\right)\right\rangle \tag{2.37}$$

$$\frac{d\phi_n(z)}{dz} = -\frac{F}{a_n(z)}\left\langle \sin\left(\alpha_{nj}(z)+\phi_n(z)\right)\right\rangle \tag{2.38}$$

Equations (2.37) and (2.38) tell how the field amplitude grows ($da/dz > 0$) or decreases

($da/dz < 0$) depending on the strength and phase of any bunching with regard to the phase of the electromagnetic field, while this relative phasing depends on the velocity of the electrons via equation (2.33). One can further see that the maximum growth rate is achieved for a relative phase of zero between bunching and the wave, $\langle \alpha_{nj}(z) + \phi_n(z) \rangle = 0$, and that in this case the amplification does not induce any phase shift on the field. In summary, to have amplification of the wave in the CFEL, not only a bunching has to be formed but also bunching must be formed at a certain relative phase with respect to the field. From equation (2.33) it can be seen that the bunching phase which maximizes the wave amplification also corresponds to a maximum deceleration of the electrons. This is, of course, reflecting that kinetic energy of particles is directly transformed into energy of an electromagnetic in the described CFEL.

In chapter 3 we will give a detailed analysis of the numerical predictions obtained from the CFEL dynamical equations for various different electron beam currents and liner parameters. Here, figure 2.4 shows a typical example of the evolution of the electromagnetic power and the electron beam power along the interaction distance z for a 75 kV-800 mA electron beam and a liner with r_d=1.5 mm, r_g=2.8 mm and ϵ_r=5.8. The graph shows the three main regions of interaction which are known as lethargy, exponential growth and saturation. During lethargy, the electromagnetic field noise present at all waveguide mode frequencies starts to form bunches in the electron beam, although the exchange of energy between the electrons and the field is still small. The bunches are formed for each noise frequency and are separated by one wavelength from each other. However, for a certain mode, which is travelling nearly synchronous with the electrons, the bunching occurs and remains at a decelerating phase with respect to the field such that the wave amplitude grows exponentially. Finally, when the electron bunches are decelerated, they end up in a relative phase corresponding to acceleration of the electrons by the radiation wave. Here, the transfer of energy reverses, the system is said to saturate, producing its maximum electromagnetic power. One can see in figure 2.4 that the maximum in the field power corresponds to a minimum in the electron beam energy as required by energy conservation. One also sees, if the interaction is continued such as in a long, lined waveguide, that the energy oscillates between the electrons and the field which leads to an output electromagnetic power below what could be achieved when the waveguide (and thus the interaction) would have been ended at saturation (approximately at 0.5 m in figure 2.4). This behaviour is general for all FELs [59].

In summary, wave amplification in a CFEL works as follows. When the electrons travel close to the dielectric liner, Čerenkov emission occurs and the field propagates as modes in the waveguide with a specific phase velocity below the speed of light in vacuum. When the phase velocity of the wave matches the electron beam velocity, the modes with a longitudinal component of the electric field start to exchange energy with the electrons and induce a correlated

modulation in the kinetic energy of the electrons. Upon further propagation, the energy modulation of the electron beam transforms into a charge density modulation and the electrons form bunches at the scale of the radiation wavelength. For a certain relative phase between these bunches and the electromagnetic wave, the bunches are decelerated and thereby amplify the field amplitude. The contributions to the field amplitude from the different bunches add up in phase and the field is amplified exponentially. This amplification continues until saturation sets in at a certain interaction length. At this interaction coordinate, also called the saturation length, the bunches shift out of the phase range corresponding to gain, into a phase which corresponds to decrease of the field amplitude. The decrease of the field amplitude is accompanied by a reacceleration of the electrons.

So far, we have recalled the basic working principle of a CFEL and reformulated it for an easy use in the remainder of this thesis. In the following sections, we describe our novel contributions to the theory of CFELs by, for the first time, including dielectric losses in the liner and by, also for the first time, considering fluctuations of the phase velocity of the wave during propagation as can be caused by irregularities in the waveguide.

2.2 CFEL with dielectric losses

Dielectric losses in the material lining the waveguide of the CFEL may induce significant power dissipation of the propagating electromagnetic mode and therefore reduce the output power of the CFEL. Nevertheless, the existing models of the CFEL dynamics have always neglected such dielectric losses, assuming that their effect is insignificant. In contrast to this assumption, we have found that dielectric losses can even prevent a CFEL to oscillate, especially in low-gain CFELs based on a feedback resonator, where the typically small growth rates might be insufficient to overcome the losses threshold. Generally, high-gain CFELs can be pumped above threshold due to the high growth rates involved but, precisely because of this, there might also be a bigger amount of power dissipated, which would increase the temperature of the liner material. This can induce a higher tangent loss of the liner material and bring the CFEL below lasing threshold. The illustration of such scenarios emphasizes the importance to investigate the influence of dielectric losses in the liner of CFELs on the output of the laser. Therefore, it is essential to properly include liner losses in the theoretical description of the CFEL dynamics. Here, we present such an extension of the CFEL model. As a first step in the extension, we study the loss-induced modification of the cold modes propagating in a waveguide and, as a second step, we calculate the implications on the dynamics of the CFEL.

2.2.1 Wave propagation in a lossy waveguide

A lossy medium is usually described with a complex permittivity $\tilde{\epsilon}_r(\omega) = \epsilon'_r(\omega) - i\epsilon''_r(\omega)$. It is standard to write the permittivity in polar coordinates $\tilde{\epsilon}_r = \epsilon_r e^{-i\delta}$, where $\tan\delta = \epsilon''_r/\epsilon'_r$ is known as the tangent loss of the medium [75].

The propagation of a wave in a material is described by the dispersion relation, *e.g.,* $k_{z0}^2 = \epsilon'_r\omega^2/c_0^2$ with ϵ'_r real, for a wave propagating in a lossless medium. For a lossy medium, due to a complex dielectric constant $\tilde{\epsilon}_r = \epsilon'_r - i\epsilon''_r$, the same dispersion relation can only be fulfilled if the wavenumber is also complex. The propagation of a wave in a lossy medium is thus given in terms of a complex wavenumber, $\tilde{k}_z = Re(\tilde{k}_z) + i\, Im(\tilde{k}_z)$. The complex wavenumber produces a twofold effect in the propagation of the wave. On one side, the existence of the imaginary part in the wavenumber translates into a damping of the amplitude of the wave, and thus into power dissipation. On the other side, the imaginary part involves a change of the phase velocity of the wave as follows. In the example above, by using the equations of the dispersion relation in a lossless medium and in a lossy medium, one can obtain the relation between the wavenumbers in both media as $(Re(\tilde{k}_z))^2 = k_{z0}^2 + (Im(\tilde{k}_z))^2$. This relation shows that the existence of an imaginary component of the wavenumber implies a real component of the wavenumber larger than the wavenumber in the lossless medium. Therefore, the phase velocity in the lossy medium is reduced with respect to the velocity in the lossless medium.

The combined effects of wave damping and slowing can be expressed in the lined waveguide by re-deriving the waveguide dispersion relation $D(\omega, \tilde{k}_{zn}, \tilde{\epsilon_r}, r_d, r_g) = 0$ as given in appendix A, however, by using a complex dielectric constant of a lossy liner medium. The resulting dispersion for the TM_{01} modes then becomes

$$\tilde{\epsilon_r}\kappa_n J_0(\kappa_n r_d)X + \kappa'_n J_1(\kappa_n r_d)W = 0 \tag{2.39}$$

where X and W are defined in appendix A. To obtain from this implicit equation the phase velocity as an explicit expression of the wave frequency we look for the roots of (2.39). For constant ω, r_d, and r_g, one can differentiate the relation and obtain

$$\mathrm{d}D = \frac{\partial D}{\partial \tilde{k}_{zn}}\mathrm{d}\tilde{k}_{zn} + \frac{\partial D}{\partial \tilde{\epsilon_r}}\mathrm{d}\tilde{\epsilon}_r = 0. \tag{2.40}$$

By using equation (2.39), we rewrite (2.40) as

$$\left(\tfrac{\tilde{k}_{zn}}{\kappa_n}A + \tfrac{\tilde{k}_{zn}}{\kappa'_n}B\right)\mathrm{d}\tilde{k}_{zn} - \left(\kappa_n J_0(\kappa_n r_d)X + \tfrac{\omega^2}{2\kappa'_n c^2}B\right)\mathrm{d}\tilde{\epsilon}_r = 0, \tag{2.41}$$

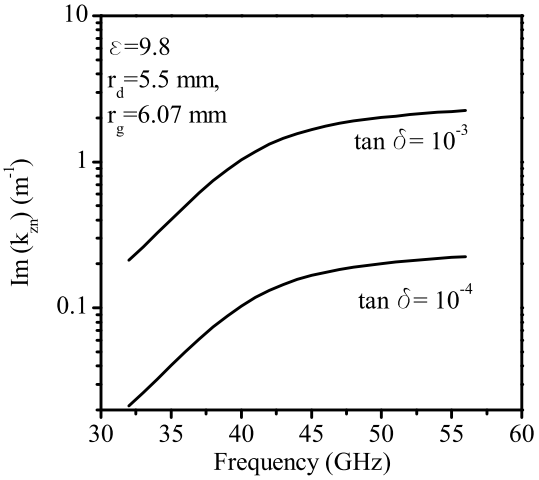

Figure 2.5: Imaginary part of the wavenumber $\tilde{k}_{zn}$ as a function of the frequency for two different values of the tangent loss, 10^{-4} and 10^{-3}. The parameters of the lined waveguide are $r_g = 6.07$ mm, $r_d = 5.5$ mm and $\epsilon_r = 9.8$.

for which we have introduced the abbreviations

$$\begin{aligned} A &= \tilde{\epsilon}_r[(J_0(\kappa_n r_d) - \kappa_n r_d J_1(\kappa_n r_d))\, X + \\ &+ \tfrac{\kappa_n'}{\tilde{\epsilon}_r \kappa_n}\,(\kappa_n r_d J_0(\kappa_n r_d) - J_1(\kappa_n r_d))\, W] \\ B &= (J_1(\kappa_n r_d) - \tilde{\epsilon}_r \kappa_n r_d J_0(\kappa_n r_d))\, W + \\ &+ \left(\kappa_n' r_d J_1(\kappa_n r_d) - \tfrac{\tilde{\epsilon}_r \kappa_n}{\kappa_n'} J_0(\kappa_n r_d)\right) X \\ &\quad + \kappa_n' r_g J_1(\kappa_n r_d) Y + \tilde{\epsilon}_r \kappa_n r_g J_0(\kappa_n r_d) Z. \end{aligned} \tag{2.42}$$

Finally, we solve (2.41) for $d\tilde{k}_{zn}$ which yields a differential equation for the desired wave wavenumbers,

$$\mathrm{d}\tilde{k}_{zn} = \frac{\frac{\kappa_n \kappa_n'}{\tilde{k}_{zn}} J_0(\kappa_n r_d) X + \frac{\omega^2}{2\tilde{k}_{zn} c_0^2} B}{\frac{\kappa_n'}{\kappa_n} A + B} \mathrm{d}\tilde{\epsilon}_r \tag{2.43}$$

To calculate the complex wavenumber $\tilde{k}_{zn}$, equation (2.43) is integrated from a real dielectric constant, corresponding to a loss-free waveguide to a complex dielectric constant, corresponding to the waveguide lined with the lossy dielectric.

To give an example of the outcome of the integration, figure 2.5 shows the imaginary part of $\tilde{k}_{zn}$ as a function of frequency for two values of the tangent loss when the wave propagates in a lined waveguide with the parameters given in the caption of the figure. One can see that $Im(\tilde{k}_{zn})$ increases with frequency showing that the losses will be more noticeable at higher

frequencies even if the tangent loss parameter is independent of the frequency.

As was done for the lossless waveguide in section 2.1.2, here we write the propagating wave in the lossy CFEL waveguide as the superposition of TM_{0n} modes,

$$\vec{E}(\vec{r},t) = \sum_{n=1}^{\infty} \mathrm{Re}\left(\vec{\mathcal{E}}_n(r)\; A_n\; e^{i(\tilde{k}_{zn}z-\omega t)}\right) \tag{2.44}$$

where $\vec{\mathcal{E}}_n(r)$ are the transverse eigenmodes with complex wavenumbers $\tilde{k}_{zn}$ and where A_n is the field amplitude.

2.2.2 CFEL dynamics with a lossy waveguide

As was done in section 2.1 to derive the dynamics of the CFEL, we expand the electromagnetic field in the waveguide into a superposition of TM_{0n} modes of the cold waveguide but allowing for slowly varying amplitudes as

$$\vec{E}(\vec{r},t) = \sum_{n=1}^{\infty} \mathrm{Re}\left(\vec{\mathcal{E}}_n(r)\; \tilde{A}_n(z)\; e^{i(\tilde{k}_{zn}z-\omega t)}\right). \tag{2.45}$$

Here, $\vec{\mathcal{E}}_n$(r) are the transverse eigenmodes, now with a complex wavenumbers $\tilde{k}_{zn}$, and $\tilde{A}_n(z) = A_n(z)e^{i\phi_n(z)}$ is the complex field amplitude. The power P_n^L carried by a mode n is now

$$P_n^L(z) = \frac{|A_n(z)|^2}{2\mu_0}\mathrm{Re}\left(\mathcal{N}_n e^{-2i\mathrm{Im}(\tilde{k}_{zn})z}\right). \tag{2.46}$$

It can be seen that the power decays with increasing z due to the imaginary part of the wavenumber. As in the lossless case, the evolution of the amplitude is obtained by solving Maxwell's equations by inserting the modes given in (2.45). The solving procedure is performed in full analogy with section 2.1. From this we obtain for the dimensionless amplitude $\tilde{a}_n(z) = e/(m_e c_0)\tilde{A}_n(z)$ the following dynamical equation

$$\begin{aligned}\frac{d\tilde{a}_n(z)}{dz} &= 2\frac{\omega_p^2\beta_{z0}e^{Im(\tilde{k}_{zn})z}\pi\tilde{k}_{zn}^*}{c_0^2\mathcal{N}_n^*\tilde{k}_{zn}}\int_0^{r_d} dr\;\left[\left\langle e^{-i\alpha_n}\right\rangle r J_0^*(\kappa_n r)+\right.\\ &\left.+ir\frac{Re(\tilde{k}_{zn})}{\kappa^*}\left\langle\frac{\beta_r}{|\beta_z|}e^{-i\alpha_n}\right\rangle J_1^*(\kappa_n r)\right]\end{aligned} \tag{2.47}$$

To keep the phase of the field real we introduce a lossy complex amplitude $\tilde{a}_n^L(z)$, which relates to $\tilde{a}$ as $\tilde{a}_n^L(z) = \tilde{a}_n(z)e^{-Im(\tilde{k}_{zn})z}$. By using (2.47), the evolution of $\tilde{a}_n^L(z)$ along z is then obtained as

$$\frac{d\tilde{a}_n^L(z)}{dz} = \frac{d\tilde{a}_n(z)}{dz}e^{-Im(\tilde{k}_{zn})z} - Im(\tilde{k}_{zn})\tilde{a}_n^L(z) \tag{2.48}$$

This equation will be used in chapter 3 to study numerically the effect of liner-induced losses in CFELs.

2.3 CFEL with fluctuations in the liner radius

The inner and outer radius of the liners used in a CFEL are specified within certain tolerance limits given by the manufacturer. The tolerance levels depend on the machining precision. As a numerical example, standard tubes that can be used as liners may have typical tolerances in the wall thickness of ± 10 %, while precision tubes can have tolerances of ± 3 %. The tolerance levels mean that the radii of the tube present random fluctuations around an average value. These fluctuations in the radii of the liner translate to fluctuations in the phase velocity of the propagating wave in the waveguide. As explained in section 2.1, the gain in the CFEL is determined by the relative phase between the bunch of electrons and the propagating wave. Therefore, we expect that the fluctuations of the radii affect the gain of the CFEL. In particular, we expect that a fluctuating phase velocity of the wave would slow the formation of bunches during the lethargy regime and would weaken the charge modulation. Thus, the fluctuating phase velocity would delay the onset of exponential growth. Additionally, once exponential growth occurs, the phase velocity fluctuations could bring the bunches out of the optimum driving phase and, thus, they might reduce the amplification of the wave amplitude. To the common belief, standard fabrication quality is high enough to neglect the influence of residual imperfection on a proper working of CFELs. However, depending on the design, a small tolerance of the liner radius can be large enough to shift the bunch of electrons from a relative phase with the field corresponding to amplification of the wave or emission to a relative phase corresponding to damping of the wave or absorption. Therefore, contrary to previous models that neglect their effect, we claim that fluctuations of the radius, even if apparently small, should be considered in the gain analysis of the CFEL. Here, we present a generalization of the dynamic equation for the CFEL to include a fluctuating phase velocity of the electromagnetic wave due to imperfections in the liner. We model, as a prototype for various kinds of imperfection, a fluctuation of the inner radius of the liner and do not separately treat other types of fluctuations, such as a spatial inhomogeneity of the dielectric constant. First, to calculate the dynamics of the laser, we study mode propagation in a waveguide with a fluctuating inner radius.

2.3.1 Wave propagation in a waveguide with a fluctuating liner inner radius

In order to model the lined waveguide with a fluctuating liner radius, we assume an average liner inner radius r_{d0} with small variations along z given by $\delta r(z)$. Thus, the inner radius of the liner is given by $r_d(z) = r_{d0} + \delta r(z)$, with $\delta r(z) << r_{d0}$. When the inner liner radius fluctuates along z we expect that the wavenumber shows also fluctuations along z, and we write

$$k_{zn}(z) = k_{z0n} + \delta k_{zn}(z), \tag{2.49}$$

where k_{z0n} is the wavenumber for an inner radius equal to the average liner inner radius, and $\delta k_{zn}(z)$ are the fluctuations of the wavenumber due to fluctuations of the inner radius. For simplicity and to show only the principle effect, we treat only the case of small and spatially slowly varying fluctuations. In this case the fluctuations of the wavenumber are small compared to k_{z0n}, and $\delta k_{zn}(z)$ is slowly varying with z within one wavelength of the radiation. In principle, a z-varying wavenumber can induce a variation with z of the phase of the field, and of the shape of the transverse eigenmodes. To model these effects, we propose that the mode propagates along the lined waveguide as a z-varying transverse eigenmode with wavenumber $k_{zn}(z)$ and we express it as

$$E_{zn}(r, z) = f_n(r, z) e^{i\left(\int_0^z k_{zn}(z')dz' - \omega t\right)}, \tag{2.50}$$

where $f_n(r, z)$ is a slowing varying function along z. Here, we limit the description to the electric field only, however, we expect that a similar behaviour is expected for the magnetic field. Further, we consider fluctuations of only the z component of the field since the radial components can be expressed as a function of the longitudinal component. To investigate the function f_n, we use the wave equation that has to be fulfilled by the electric field E_{zn}

$$\left(\vec{\nabla}_\perp^2 + \frac{\partial^2}{\partial z^2} + \epsilon_r \frac{\omega^2}{c_0^2}\right) E_{zn}(r, z) = 0. \tag{2.51}$$

By substituting (2.50) in (2.51), we have the following condition between $f_n(r, z)$ and $k_{zn}(z)$

$$\vec{\nabla}_\perp^2 f_n + \frac{\partial^2 f_n}{\partial z^2} + \left(\frac{\omega^2}{c_0^2} - k_{zn}^2(z)\right) f_n + i\left(2k_{zn}(z)\frac{\partial f_n}{\partial z} + f_n \frac{dk_{zn}(z)}{dz}\right) = 0. \tag{2.52}$$

Within the SVEA for f_n stated above, we can neglect the second derivative $\partial^2 f_n / \partial z^2$ for small variations $\delta r_d(z)$. By separately equating the real and imaginary parts of equation (2.52) to zero

we obtain

$$\vec{\nabla}_{\perp}^{2} f_n + \left(\frac{\omega^2}{c_0^2} - k_{zn}^2(z) \right) f_n = 0 \tag{2.53}$$

$$2k_{zn}(z)\frac{\partial f_n}{\partial z} + f_n \frac{dk_{zn}(z)}{dz} = 0. \tag{2.54}$$

From equation (2.54) we derive that

$$f_n(r,z) = \frac{g(r)}{\sqrt{k_{zn}(z)}} \tag{2.55}$$

with $g(r)$ representing a radial dependence of the function $f_n(r,z)$. If in equation (2.53) we make the approximation $k_{zn}(z) \approx k_{z0n}$, and then substitute (2.55) in (2.53), we obtain that the radial function $g(r)$ is a solution of Bessel's equation for a homogeneous lined waveguide with constant inner radius r_{d0}. Therefore, to first order approximation, it can be assumed that the transverse profile of the electromagnetic wave remains unaffected by the slowly varying inner radius. On the other hand, small variations in $k_{zn}(z)$ may give an appreciable change in $\exp\left(i\int_0^z k_{zn}(z')dz'\right)$, and thus $k_{zn}(z)$ cannot be approximated by k_{z0n} in the phase of the field, which is given by $\int_0^z k_{zn}(z')dz' - \omega t$. The slowly varying longitudinal wavenumber is

$$k_{zn}(z) = k_{z0n} + \int_0^z \frac{dk_{zn}}{dz'}dz' \approx k_{z0n} + \left.\frac{\partial k_{zn}}{\partial r_d}\right|_{r_{d0}} \int_0^z \frac{dr_d}{dz'}dz'. \tag{2.56}$$

Finally, the modes in the waveguide with fluctuations in the liner can be written as

$$\vec{E}(\vec{r},t) = \sum_{n=1}^{\infty} \mathrm{Re}\left(\vec{\mathcal{E}}_n(r)\, \frac{A_n}{\sqrt{k_{zn}(z)}}\, e^{i(k_{zn}(z)z - \omega t)} \right), \tag{2.57}$$

where $\vec{\mathcal{E}}_n(r)$ are the transverse eigenmodes with wavenumbers $k_{zn}(z)$, and A_n are the mode amplitudes.

2.3.2 CFEL dynamics in a waveguide with a fluctuating liner inner radius

As in previous sections, we write the propagating modes in the waveguide of the CFEL as a superposition of the TM_{0n} modes of the cold waveguide given in (2.57) but with a slowly varying complex amplitude. We can write the total field as

$$\vec{E}(\vec{r},t) = \sum_{n=1}^{\infty} \mathrm{Re}\left(\vec{\mathcal{E}}_n(r)\, \hat{A}_n(z)\, e^{i(k_{zn}(z)z - \omega t)} \right) \tag{2.58}$$

where $\hat{A}_n(z) = A_n(z)/(\sqrt{k_{zn}(z)})\, e^{i\phi_n(z)}$ and $\vec{\mathcal{E}}_n(r)$ is the transverse eigenmode. As described in previous sections, the evolution of the field amplitude is obtained by inserting the field (2.58) into Maxwell's equations. The mathematical procedure is equivalent to the one presented in section 2.1.3 such that, here, we only show the result for the evolution of the normalized field amplitude,

$$\frac{d\hat{a}_n(z)}{dz} = \frac{2\omega_p^2 \beta_{z0} \pi k_{z0n}}{c_0^2 \mathcal{N}_n^* \sqrt{k_{zn}(z)}} \int_0^{r_d} r\, dr \, \left[\left\langle e^{-i\alpha_{nj}(z)} \right\rangle J_0(\kappa_n^* r) + i \frac{k_{zn}(z)}{\kappa_n^*} \left\langle \frac{\beta_r}{|\beta_z|} e^{-i\alpha_{nj}(z)} \right\rangle J_1(\kappa_n^* r) \right], \tag{2.59}$$

where $\alpha_{nj}(z) = \int_0^z k_{zn}(z')dz' - \omega t_j$ is used to calculate the bunching term. In chapter 3, based on (2.59), we will give a numerical analysis of the gain of the CFEL under the influence of the liner fluctuations.

3

Numerical study of the gain in a Čerenkov FEL

Abstract

In this chapter, we investigate numerically the gain of a CFEL both in the low- and in the high-gain regimes of operation and under the effect of several types of losses. For that, we use the model presented in chapter 2. We show that the gain bandwidth of the CFEL is substantially broadened in the high-gain regime and we offer an explanation of such effect based on the evolution of the complex bunching term. We also show that, in the high-gain regime and off-resonance, the lossy CFEL seems to adjusts its own dynamics and induce a higher amplification of the wave, exactly enough to compensate the dissipation caused by the dielectric losses. Such a phenomenon is interesting from a theoretical point of view since it has not been observed in other laser systems before. Finally, the calculations of this chapter show that, the analysis of the effects produced by dielectric losses and liner fluctuations is advisable in the CFEL design since micrometre changes of the radius can be enough to suppress oscillation of the laser, specially in low-gain CFELs.

In the previous chapter 2, a theoretical model was presented that describes the dynamics of the CFEL and which enables to calculate the laser gain and output power. We saw that the growth of the field amplitude depends on how well the bunches are formed within the electron beam and how well the phase matching of these bunches with the radiation field is maintained. From the nature of the generation process it is clear that the gain is degraded by an initial energy spread in the electron beam because this reduces the bunching of the electrons [57]. Furthermore, we saw that, if the phase velocity of the radiation wave fluctuates, *e.g.,* by the variation of the inner radius of the liner, then both the formation of the bunches and the phase matching are adversely affected. Finally, we saw that dielectric losses in the material lining the waveguide lead to a damping of the electromagnetic field and, therefore, reduce the output power of the CFEL. In chapter 2, we generalized the model of the laser to prepare a quantitative description and to include such liner fluctuations and dielectric losses. In the present chapter, we apply this generalized model to study in specific examples of CFELs how strongly liner

fluctuations and dielectric losses influence the laser output. In section 3.1 we describe the CFEL that we use in this study and investigate its operation for low and high currents in the electron beam. Next, in section 3.2 the gain of this CFEL is studied under the presence of dielectric losses in the liner and in section 3.3 under the presence of liner radius fluctuations.

3.1 Low- and high-gain regimes in the Čerenkov FEL

It is expected that different gain regimes have different sensitivities towards the effects of liner radius fluctuations and dielectric losses. To study the influence of liner fluctuations and dielectric losses on the output characteristics of CFELs in various regimes, we used for our calculations the parameters of a CFEL from a previous experiment [67], which can be operated with both low and high pump currents. As a typical example for the generation of an output frequency in the range of tens of GHz, we assume the following parameters: the radius of the cylindrical electron beam is fixed at r_b=5 mm and the electron beam current I_b is varied from 0.8 A to 20 A, which corresponds to electron current densities of 1 A/cm^2 to 25 A/cm^2. We assume that the liner is made of alumina, which has a relative dielectric constant of ϵ_r=9.8, with an average inner radius of r_{d0}=5.5 mm and an average thickness of d=0.57 mm.

In chapter 2 we saw that the numerical integration of the dynamical equations of the CFEL shows that a weak input field (at z=0) of power P_{in} undergoes an exponential growth until the growth saturates and terminates at a power P_{sat} at a certain interaction length, z_{sat}. With the parameters given above, our model predicts that the CFEL emits an output frequency around 50 GHz when the electron beam energy is set to 84.2 keV. At such voltage and with no liner fluctuations and no dielectric losses, the saturated power is maximum for a frequency of 50.2 GHz for weak pumping (I_b =0.8 A) and for a frequency of 50.6 GHz for strong pumping (I_b =20 A). The saturated powers for the low and high pumping are about 220 W and 24 kW, respectively, and they are reached for distances of 1.28 m and 0.41 m, respectively. For these pump currents, figure 3.1 (a) shows the gain spectrum which is obtained by tuning the frequency of the probe input field from below to above resonance (32 GHz to 54 GHz). For frequencies below 31.3 GHz, the phase velocity of the wave in the cold waveguide is above c_0 and, therefore we chose 32 GHz as the lower frequency limit of the input seed in our calculations. It can be seen that at strong pumping there is a wide tail of appreciable power (of about a few hundreds of watts) extending to frequencies far below 50 GHz. To better understand the latter effect we have calculated the phase velocity of the amplified wave as a function of the probe frequency, for weak and strong pumping and the results are plotted in figure 3.1 (b). For comparison, we have also plotted the phase velocity in the cold waveguide as the dotted line and the initial velocity of the electrons as the solid line. In figure 3.1 (b) all velocities are normalized to c_0. It can be seen that at low

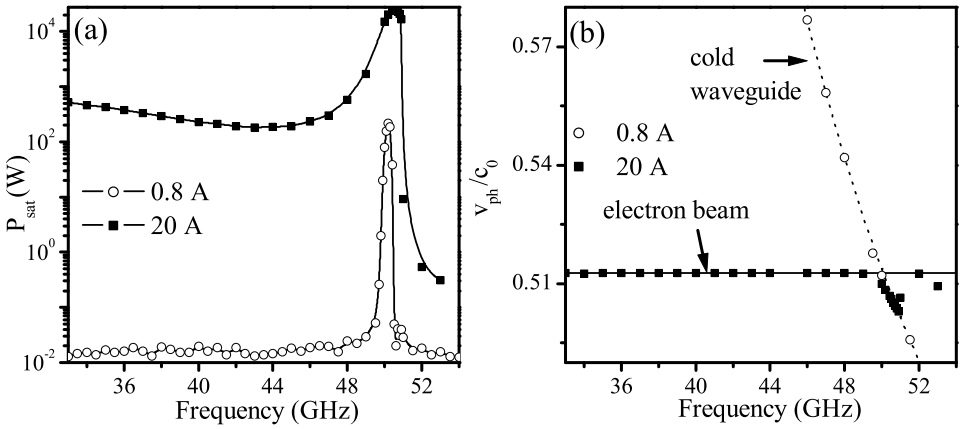

Figure 3.1: For the electron beam currents of 0.8 A and 20 A and no fluctuations in the liner radius, saturated power P_{sat} (lines are for guidance) (a) and phase velocity (b) versus the frequency of the seed field. Fig. (b) also shows the initial velocity of the electron beam and the phase velocity of the TM_{01} mode in the cold waveguide.

pump current (I_b =0.8 A), the phase velocity of the field is almost equal to the phase velocity of the cold TM_{01} mode and thus matches the electron velocity only in a narrow range around 50 GHz, resulting in a narrowband gain. In contrast, for strong pumping (I_b =20 A), the phase velocity of the field is strongly reduced to a constant value matching the electron velocity over a wide range of frequencies spanning at least from 32 GHz to 50 GHz. Additionally, in a small range above 50 GHz, the phase velocity reduces and follows the velocity of the wave in the cold waveguide.

To explain the origin of the gain at frequencies below resonance, we use the simplified dynamical equations of the CFEL shown in equations (2.37) and (2.38), where the evolution of the amplitude and the phase of the field is described. Equation (2.37) shows that the growing (or damping) of the amplitude $a_n(z)$ along z is intrinsically associated to the relative phase between the field and the bunching term, $\langle \alpha_n + \phi_n \rangle$, which is zero only in the case of maximum (or minimum) growth rate, *i.e.,* at resonance. Equation (2.38), in turn, describes how the phase of the field is driven by the bunched electrons. This change of phase translates into a change of the phase velocity of the wave given by

$$v_{\phi_n} = \frac{\omega}{k_{zn} + \frac{d\phi_n(z)}{dz}} \tag{3.1}$$

For a better illustration of the amplitude and phase changes of the wave induced by the electron bunches, we show equations (2.37) and (2.38) graphically in figure 3.2. Here, the bunching

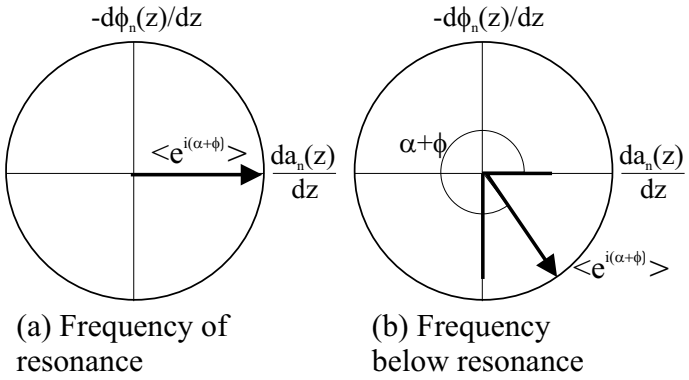

Figure 3.2: Diagram showing the contribution of the bunching term to the driving of the amplitude and the phase of the field for the case of a perfectly velocity matching frequency (a) and a frequency below resonance (b).

term $\left\langle e^{i(\alpha_n(z)+\phi_n(z))}\right\rangle$ is represented as a phasor. Its projection on the horizontal axis gives the change of amplitude of the field and its projection on the vertical axis gives the change of phase of the field. At resonance, for both low- and high-gain regimes, the amplitude growth is maximum and the phase of the field is not modified. It corresponds to the bunching phasor pointing along the horizontal axis, as it is shown in figure 3.2 (a). It points along the positive part of this axis for amplification of the wave amplitude, or laser emission, and along the negative part for damping of the wave amplitude, or absorption. The modulus of the bunching phasor indicates the quality of the bunching and, therefore, the strength of the emission or absorption process. For a frequency below resonance, figure 3.1 (b) shows that the phase velocity of the wave in the cold waveguide is significantly higher than the electron beam velocity. For low electron beam currents densities, the scaling factor F in equations (2.37) and (2.38), which is proportional to the electron current, is small and, therefore, a growing amplitude $a_n(z)$ quickly stops the phase change. As a result, the phase velocity remains equal to the phase velocity of the cold waveguide, as we can see in figure 3.1 (b) for the case of 0.8 A electron beam current. Therefore, it is not possible to phase-match the electrons to the wave and the gain quickly drops to zero for frequencies away from resonance. At sufficiently high electron beam current, however, when the scaling factor F is large, the field dynamics is completely different. The electrons drive the phase of the field producing a considerable value of $d\phi_n/dz$, that makes the phase velocity of the field assume a value that matches the velocity of the electrons. This changed phase velocity leads to a situation as displayed in the figure 3.2 (b) where the bunching vector attains a fixed angle $(\alpha_n(z) + \phi_n(z))$ with the horizontal axis. The projection of the phasor in the horizontal axis corresponds to the off-resonance amplification of the field amplitude, which gives rise to broadband wave amplification of figure 3.1 (a). The projection in the vertical axis corresponds to the change of velocity for frequencies off-resonance, which gives the velocity shown in figure

3.1 (b) for 20 A. Thus, the magnitude of the bunching determines both the strength of the wave amplification (or wave damping) and the strength of the driving of the field phase. The modulus of the bunching term as a function of the frequency is calculated for 20 A and it is shown in figure 3.3. We see that for a high current, the bunching modulus increases for decreasing frequencies, probably due to a better overlap between the wave and the electron beam. Therefore, although for decreasing frequency, the difference in velocities between the wave in the cold waveguide and the electrons is larger (see figure figure 3.1 (b)), the vertical projection of the bunching term, or $d\phi/dz$, is also larger and can overcome this difference. The horizontal projection, or $da_n(z)/dz$, increases as well, which produces higher amplification of the wave for decreasing frequency as it can be seen in figure 3.1 (a). Thus, initially "unmatched" frequencies below resonance can experience amplification of their field amplitude when the electron current is high enough.

The situation is different for frequencies above resonance where the gain quickly drops as can be seen in figure 3.1 (a). For a frequency above resonance the phase velocity in the cold waveguide is below the electron beam velocity. By the same mechanism explained above, the electron beam can increase the phase velocity of the wave and the wave and the electrons are matched again in velocity. However, the projection of the phasor in the horizontal axis corresponds now to damping of the field amplitude, which produce a decrease of the output power for frequencies above 50 GHz in figure 3.1 (a).

In the following, we continue to describe the dynamics of the CFEL described above in the regimes of high gain and low gain (pump currents 0.8 A and 20 A), however, with a quantification of the effects of dielectric losses and liner fluctuations.

3.2 Effect of dielectric losses

To minimize the power dissipation of the propagating mode, liner materials with low dielectric loss in the microwave region of the spectrum are normally chosen during the design of CFELs, with tangent losses between 10^{-4} and 10^{-3}. To our knowledge such losses have so far not been taken into account in any CFEL description. More importantly, what has been neglected so far in all CFEL designs calculations is that the dielectric losses may strongly increase with the temperature of the medium and also with the frequency of the electromagnetic wave [76]. So even if the specified loss of material is a relatively low value, the losses actually can turn out to be much larger during the laser operation when energy is dumped into the liner and raises its temperature. Excessive dielectric losses may even prevent a CFEL to oscillate, especially in low-gain systems, where small growth rates might be insufficient to overcome the losses. High-gain CFELs may be expected to suffer less strongly from losses. However, due to the

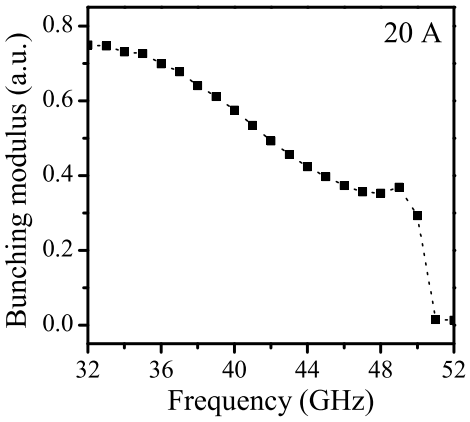

Figure 3.3: Modulus of the bunching term as a function of the frequency of the radiation for an electron beam current of 20 A.

higher power of such systems, there may also be a higher amount of power dissipated which, via an increasing temperature, induces a significant tangent loss of the material far above the loss specifications of the cold material. Therefore, it becomes essential to estimate the effects produced by the dielectric losses on the performance of the CFEL, both in low- and in high-gain regimes.

For the explanation, we use the simplified version of the CFEL dynamics given in equations (2.37) and (2.38), however, including additional terms that contain the losses of the liner material.

$$\frac{da_n^L(z)}{dz} = F\left\langle \cos\left(\alpha_n + \phi_n^L\right)\right\rangle - Im(\tilde{k}_{zn})a_n^L \tag{3.2}$$

$$\frac{d\phi_n^L(z)}{dz} = -\frac{F}{a_n^L}\left\langle \sin\left(\alpha_n + \phi_n^L\right)\right\rangle \tag{3.3}$$

The presence of the losses in equations (3.2) is shown explicitly by $Im(\tilde{k}_{zn})$, which leads to a decay of the field amplitude along z and thus the dissipation of power. However, when the longitudinal wavenumber is complex, *i.e.,* dielectric losses are present, also the phase $Re(k_{zn})z - \omega t$ of the driving term is slightly shifted with respect to the phase of a lossless system, $k_{zn0}z - \omega t$, since $Re(k_{zn}) > k_{zn0}$, as was derived in chapter 2. Note that, because the gain is determined by the relative phase between the electrons and the mode, the phase shift induced by the lossy liner modifies also the gain, in addition to the obvious effect of field amplitude damping. We shall see this with the example of CFEL considered in this chapter.

For the CFEL described in the previous section, we calculate the saturated power P_{sat}, and the interaction length required for saturation z_{sat}, when the dielectric losses are present. For cold alumina the specified loss varies typically between a tangent loss of 10^{-5} and of 10^{-3} depending

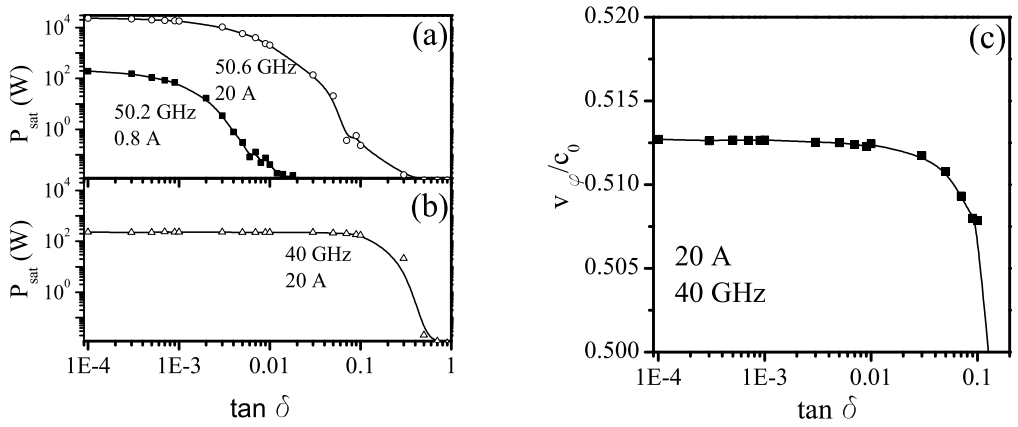

Figure 3.4: Saturated power P_{sat} as a function of the tangent loss of the liner for the resonant frequency and pump currents of 0.8 A and 20 A (a) and for a frequency of 40 GHz and a pump current of 20 A (b). Also shown is the phase velocity of the wave (normalized to c_0) as a function of the tangent loss of the liner for a current of 20 A and a frequency of 40 GHz (c).

on the quality of the sample [76]. However, here we explore a wider range of losses that comprises low-loss dielectrics (tan $\delta = 10^{-5}$) to dielectrics at elevated temperature, where high radiation powers might render the dielectric essentially conductive (tan $\delta = 1$). We study the effect of the dielectric losses in two cases: for resonance and for frequencies below resonance, where earlier (figure 3.1 (a)) we had found significant gain caused by phase velocity reduction. The saturated power at resonance (around 50 GHz) for increasing dielectric losses is shown in figure 3.4 (a) for a low (0.8 A) and a high (20 A) electron currents. It can be seen that, as expected, the low-current CFEL is much more sensitive to the dielectric losses than the high-current CFEL. While the saturated power has decreased to half of its value for a tangent loss of $5\ 10^{-3}$ for a low pumping current (0.8 A), the same loss results in a saturated power still about 86 % of the maximum lossless value for a high pumping current (20 A). These findings are in line with what is expected in other types of lasers as well, *e.g.,* solid state lasers, where low losses are important in low gain systems.

Surprisingly, we have observed a rather different behaviour for the off-resonance gain below 50 GHz. In this spectral range, not accessible with low current pumping, the laser gain appeared to be unusually robust against even strong losses. To demonstrate this behaviour, figure 3.4 (b) shows the saturated power P_{sat} as a function of the tangent loss of the liner for 20 A at some frequency below resonance (here we selected 40 GHz). It can be seen that the saturated power remains at constant value of about 200 W although the dielectric loss of the liner increases even over three orders of magnitude. Only when the tangent loss becomes as large as 10^{-1}, the power starts to decrease and eventually reduces to zero. To understand this phenomenon we compare

the velocities of the wave for the different frequencies. At resonance, the velocity of the wave is slightly below the velocity of the electrons, as it can be seen in figure 3.1 (b). That velocity, which for our example is 0.5053 c_0, allows for optimal gain in the CFEL. At a frequency below resonance, figure 3.1 (b) shows that the velocity of the wave is equal to the velocity of the electrons and, although it allows for gain, the amplification is not maximum. However, the addition of dielectric losses in the liner can reduce further the velocity of the wave. Following the numerical example here, for a frequency of 40 GHz and a pump current of 20 A, we have calculated the velocity of the propagating wave as a function of the tangent loss of the liner and the result is shown in figure 3.4 (c). It can be seen that the phase velocity of the field decreases with increasing tangent loss. The increasing losses reduce the velocity of the wave at 40 GHz below the electrons velocity and bring it closer to the velocity of the wave at resonance, *i.e.,* to the velocity that allows for maximum gain. The effect is an increase of the gain in the CFEL. For a tangent loss of 0.1, figure 3.4 (c) shows that the velocity of the wave at 40 GHz is equal to 0.5053 c_0, that is, equal to the velocity of the wave at resonance.

The question can be raised on which of the following two effects is dominant: (i) the damping of the magnitude of the wave by increasing the losses or (ii) the extra gain for the wave as a result of loss induced wave slowing. The calculations presented in figure 3.4 (b) give the answer: when operating a strongly pumped CFEL below resonance in its broadband gain region, the loss induced by dissipation (effect (i)) is exactly compensated by a loss-induced extra gain (effect (ii)). Only for extremely large losses or larger detuning further away from resonance, the dissipated power cannot be compensated by additional gain and the saturated power decreases (figure 3.4 (b) beyond tan δ=0.1).

In summary, dielectric losses decrease the saturated output power at resonance for both the low- and the high-current-driven CFEL in agreement with expectations. In contrast, for strong pumping and frequencies below resonance, the loss-induced reduction of the phase velocity of the cold waveguide radiation mode results in an increase in gain for the amplitude that exactly compensates the dissipated power for the cases investigated. Therefore, the output power for frequencies below resonance is not affected by the presence of the dielectric losses but remains constant up to a certain threshold of losses.

3.3 Influence of liner fluctuations

We saw in chapter 2 that, when the waveguide shows irregularities along the propagation distance, *e.g.*, by fluctuations of the inner radius of the liner, the fields experience a twofold effect. First, the fluctuating radius modifies the transverse mode profile. Second, it produces fluctuations in the phase velocity of the wave when it propagates along the waveguide. However, it

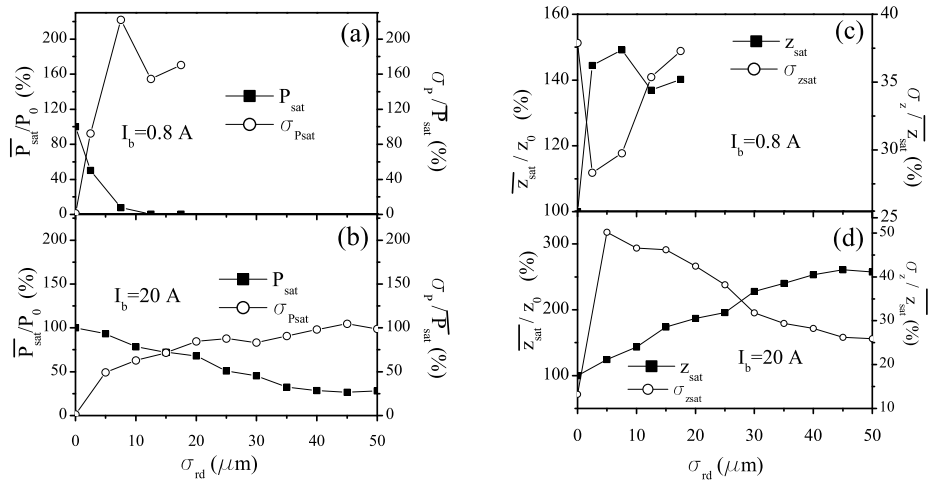

Figure 3.5: Normalized saturated power ($\overline{P_{sat}}/P_0$) and normalized standard deviation ($\sigma_P/\overline{P_{sat}}$) as a function of the standard deviation of the liner fluctuations σ_{rd} for a weak pump current of 0.8 A (a) and a strong pump current of 20 A (b). Normalized distance to saturation ($\overline{z_{sat}}/z_0$) and normalized standard deviation $\sigma_z/\overline{z_{sat}}$ as a function of the standard deviation of the liner fluctuations σ_{rd} for a weak pump current of 0.8 A (c) and a strong pump current of 20 A (d). All the cases are at resonance. The lines are only for guidance.

was shown in chapter 2 that, if the liner fluctuations are small and slowly varying along the propagation distance, they mainly affect the phase velocity of the wave while the transverse mode profile remains approximately unchanged. The variation of phase velocity can be expressed as a variation of the longitudinal wavenumber k_{zn} with z. Since the variation in k_{zn} is the result of the variation of r_d with z, to better display the scaling of the wavenumber, we expand the variation of k_{zn} into a product of partial derivatives

$$\frac{dk_{zn}}{dz} = \frac{\partial k_{zn}}{\partial r_d}\frac{\partial r_d}{\partial z} \tag{3.4}$$

The first factor ($\partial k_{zn}/\partial r_d$) can be seen as a device parameter because it depends only on the dimensions of the lined waveguide and is thus specific for a particular design of the CFEL. The second factor ($\partial r_d/\partial z$) contains the variations of the radius of the liner. Equation (3.4) makes clear that the size of phase velocity fluctuations and thus the sensitivity of a CFEL to liner fluctuations can be rather different for each CFEL even when the same absolute size of liner radius fluctuations is present. Therefore, to avoid a large sensitivity of the laser to liner fluctuations, geometries should be chosen that minimize the scaling factor $\partial k_{zn}/\partial r_d$. For the CFEL described in the section 3.1, we have $\partial k_{zn}/\partial r_d = -4.6\ 10^6\ m^{-2}$. An rms fluctuation of 1 % would produce a change in the longitudinal wavenumber of $\Delta k_{zn} = 253\ \mathrm{m}^{-1}$. Such

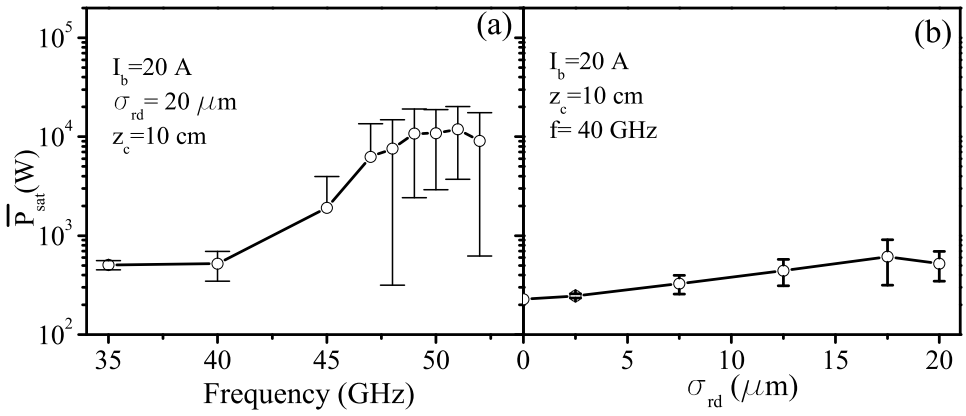

Figure 3.6: For the electron beam current of 20 A, (a) average saturated power $\overline{P_{sat}}$ versus the frequency of the seed field for liner fluctuations characterized by $\sigma_{rd} = 20$ μm and $z_c = 10$ cm and (b) average saturated power $\overline{P_{sat}}$ versus σ_{rd} for a frequency of 40 GHz. In both graphs lines are for guidance.

a change in the longitudinal number would induce a phase difference of the wave of π after a propagation of only 1.3 cm and, therefore, it would be sufficient to move the electron bunch out of the gain region. This must be taken into account if comparison with other systems is to be made.

To model the variation in the inner liner radius we use a random distribution of radius fluctuations superimposed on the average radius r_{d0}, and where in each specific distribution the strength of the liner fluctuations is characterized by its rms value, σ_{rd}. A spatial low-pass filter with a cut-off length z_c is used to remove from the random distribution spatially fast fluctuations, compared to the wavelength, which are excluded by the approximations used in our model. The cut-off length has to be large compared to the wavelength but we obtained that the output power does not strongly depend on the actual value of z_c once the slow-varying fluctuations approximation is fulfilled. We choose a cutoff-length of $z_c = 10$ cm, which is about 16 times the free-space wavelength for 50 GHz, such that the approximation is well fulfilled. The size of the rms value is set to values in a range between zero and 50 μm, which for this setup corresponds to a maximum tolerance in the radius of 1%. Note that this is still very optimistic compared to standard tubes but can be realised using precision tubes.

For the CFEL described in the section 3.1, we calculate the saturated power P_{sat} and the distance to saturation z_{sat} when the liner radius fluctuations are present. In order to obtain statistical information of the output as a function of typical liner fluctuations, we generate an ensemble of 100 different realizations of random liner fluctuations for each combination of the rms fluctuations amplitude σ_{rd} and cut-off distance z_c. For each combination we determine

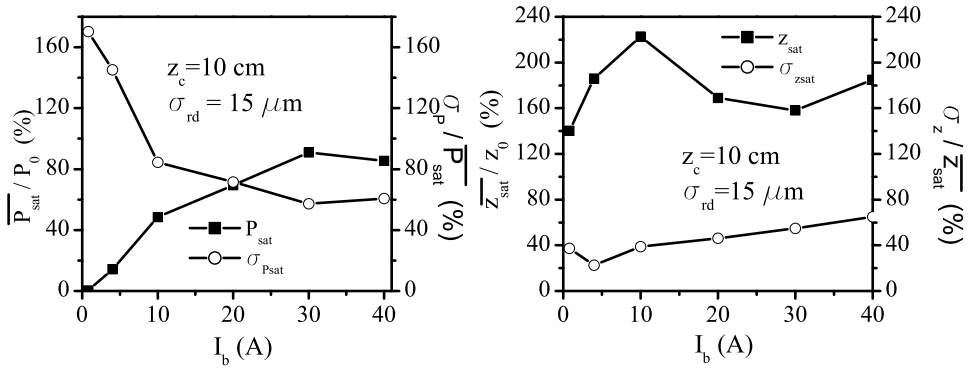

Figure 3.7: Normalized saturated power ($\overline{P_{sat}}/P_0$) and normalized standard deviation($\sigma_p/\overline{P_{sat}}$) as a function of the electron beam current I_b (a) and corresponding values for the distance to saturation (b).

the ensemble average $\overline{P_{sat}}$ and its standard variation, σ_P, and the corresponding values for the distance to saturation, $\overline{z_{sat}}$ and σ_z. A large standard deviation, σ_P or σ_z, would indicate that, in such a CFEL, liner fluctuations should be avoided because the gain and the optimum interaction length are difficult to predict.

To study the effect of the liner fluctuations on the whole gain bandwidth of the laser, we calculate the saturated power and the distance to reach saturation at resonance and at frequencies below and above resonance. The results of the saturated power at resonance are shown in figures 3.5 (a) and (b). They show the ensemble average of the saturated power, $\overline{P_{sat}}$, normalized to the saturated power in absence of fluctuations, P_0, as a function of the standard deviation of the fluctuations in the inner liner radius, σ_{rd}. Figure 3.5 (a) shows the results for a low current pumping (I_b=0.8 A) and 3.5 (b) for a high current pumping (I_b=20 A). The corresponding values for the distance to saturation z_{sat} are shown in figures 3.5 (c) and (d). It can be seen in figure 3.5 (a) that the power for the low-gain CFEL is reduced to almost zero already for small liner fluctuations, $\sigma_{r_d} = 20$ μm, which is only about 0.4% of the liner radius. Therefore, seemingly irrelevant liner fluctuations may lead to a complete failure in bringing a CFEL into operation. In contrast, for the same rms fluctuation but with strong pumping, almost 70% of the output (compared to the case of a perfect liner) can be expected. In both regimes of operation of the CFEL, *i.e.,* weak and strong pumping, $\overline{z_{sat}}$ is larger than z_0. This is due to the increase of the lethargy distance and the reduction of the growth rates. Thus, the formation of the bunches and the phase matching between the bunch and the wave are adversely affected by the liner fluctuations. Such results indicate that at strong pumping the regular precision tubes can be used without seriously degrading the gain of the CFEL, but it is more difficult to manufacture

liners with the required precision when the CFEL operates in the low-gain regime. To have a realistic calculation of the expected powers, the liner fluctuations must be considered in the design of the CFEL.

The results for frequencies away from resonance is given in figure 3.6 (a), which shows the averaged saturated power as a function of the frequency of the seed field (from 34 to 52 GHz) for a standard deviation of the fluctuations in the liner radius of $\sigma_{rd} = 20$ μm. By comparison with the spectrum shown in figure 3.1 (a), it can be seen that the fluctuations broaden the gain bandwidth of the CFEL and at the same time reduce the maximum saturated power. This is in agreement with the results shown in figure 3.5 (b). This broadening initially increases the output at neighbouring frequencies before the saturated power is also reduced at these frequencies. As an example, figure 3.6 (b) shows the average saturated power for 40 GHz as a function of the standard deviation of the fluctuations σ_{rd}. The power initially increases with the fluctuations as a result of the broadening. For larger fluctuations, the power starts to drop here as well. Such a behaviour is similar to the bandwidth broadening occurring in other types of lasers due to various loss mechanisms. The broadening should be especially considered when the CFEL is to be used inside a resonator to avoid mode competition.

From the previous sets of results we have seen that the reduction of the power for a fixed value of liner fluctuations is smaller the higher the current is. However, in an experimental setup, it is less convenient to use high currents. In order to know the minimum current necessary to avoid an excessive decrease of the power, we have calculated, for a fixed value of liner fluctuations, the saturated power as a function of the electron beam pump current. At resonance, figure 3.7 (a) shows the normalized ensemble average $\overline{P_{sat}}/P_0$ and the spread $\sigma_P/\overline{P_{sat}}$ as a function of the electron beam current I_b. Figure 3.7 (b) shows the corresponding values for z_{sat}. In all the cases, the rms radius fluctuation is fixed at σ_{r_d} =15 μm. We can see that the electron beam current must be at least 30 A to keep the reduction of the saturated power below 10 % of the maximum attainable without fluctuations. Therefore, quite high currents are required to avoid a large reduction of the power.

In summary, the effects produced by fluctuations in the radius of the liner, although seemingly small on a first view, may seriously hamper the functioning of CFELs, particularly in the low-gain regime of operation. Our calculations show that also in the high-gain regime the saturated power can be substantially degraded by the presence of liner fluctuations. As a conclusion, when designing the liner, it is advisable both to select a geometry with small scaling factor, $\partial k_n/\partial r_d$, and to reduce the absolute size of radius fluctuations via high-precision manufacturing. For the CFEL considered here, and for a radius tolerance of 1%, the relative change of the longitudinal wavenumber with z is sufficiently large to reduce the saturated power by 25 %. In this case, the selection of high-precision tubes is recommended.

4

Emission properties of the Čerenkov FEL

Abstract

In this chapter, we investigate the physical dimensions of the liner in a CFEL when a high-power microwave output is to be obtained from a device of compact dimensions. To enable a compact size, the novel concept in this study is the generation of high output with a low-energy and low-current electron beam, and with a short interaction region. The study includes the effects produced by several types of losses, such as dielectric losses, liner fluctuations and energy spread of the electron beam. We show that radiation at frequencies around 50 GHz and 22 GHz can be achieved by using quartz and alumina liners, respectively. We show that, for negligible losses, the quartz-lined CFEL can emit in the kilowatt level when it is configured as an oscillator and the alumina-lined CFEL can emit several tens of watts when it is configured as a single-pass amplifier. Finally, we quantify the gain degradation for both configurations under the influence of dielectric losses, liner fluctuations, and energy spread in the electron beam.

In the previous chapter 3, we have showed that low-current pumped CFELs are able to provide amplification of a wave by several orders of magnitude. We saw that, to calculate the expected output powers in a CFEL design, the inclusion of dielectric losses and radius fluctuations in the liner can be of central importance, especially for low-energy and low-current pumped, and thus compact CFELs. Most of the CFELs operated till present use electron beams of energies larger than 100 keV and currents of more than 1 A. These CFELs produce high peak powers at a low duty cycle and are considered high-gain devices, but the named pump beam specifications render these lasers rather bulky devices. A compact design for the CFEL requires low voltages, low currents and also short interaction lengths. In this chapter, we determine the characteristics of the electron beam and of the liner of the CFEL that allows for the construction of compact CFELs, where the above named losses are accounted for as well.

In order to be competitive within the range of available microwave sources, the CFEL should aim on the higher frequency side of the microwave spectrum. However, for a fundamental

research on a low gain and compact CFEL, the choice of frequency is not of primary interest and therefore we made our design studies at 22 GHz as nominal operating frequency, within the K-band (18-27 GHz) and at a nominal 50 GHz, within the V-band (40-75 GHz).

In section 4.1 we analyse the influence of the electron beam current and voltage, *i.e.*, the characteristics of the pump beam specification, on the performance of the CFEL. Next, we describe in section 4.2 our choice of appropriate waveguide dimensions and liner materials. Finally, for the electron beam and lined waveguide selected, we study in section 4.3 the characteristics of the radiation expected from the CFEL.

4.1 Pumping conditions

The pump energy in a CFEL is provided by an accelerated electron beam. Within the single-particle regime (Compton regime), the gain of the CFEL increases linearly with the electron beam current density [62]. Thus, high electron beam current densities are desirable since they can amplify the wave to high powers within short distances. Nevertheless, for very high electron beam current densities the Coulomb repulsion between the electrons, *i.e.*, the space-charge effect, becomes dominant, and experimentally it becomes more difficult to obtain a good beam quality. In this thesis, to avoid such complications, we have decided to consider only current densities within the Compton regime by choosing a suitable combination of the cross-section of the electron beam and the total current. So far, most of the CFELs used electron beams with a rather large cross section, which then also requires a large current to provide sufficient gain. In practice, however, a large total current leads to a higher technical complexity. For example, when the electrons are dumped after passing through the waveguide, their energy is dissipated and this might require bulky cooling methods when the total current is high. Also, high currents only allow for a low duty cycle unless a large-scale power supply is used. In the approach that we take here we aim on a compact design by restricting the beam to a small current and, to generate a high current density for sufficient gain, reducing the size of the electron beam diameter. More specifically, we have restricted our design considerations to a current below 800 mA and an electron beam with only 2 mm diameter, which corresponds to a high current density of 25.5 A/cm^2. The choice of such a small current is a big step towards miniaturization of the CFEL which has not been attempted so far in any other design.

Next to the current of the electron beam, the accelerating voltage of the beam strongly influences the compactness of the design. For example, due to the risk of high-voltage breakdown, it is required to maintain a generous distance between all electrodes biased at more than a few kilovolts difference. To give a typical number, a 20 kV DC voltage between two electrodes in air demands at least 1 cm separation between them. Also, when working with high voltages

such as in the MeV range, a significant amount of high energy X-rays is generated when the electrons are dumped, which then needs an extensive shielding with bulky and heavy setups. In contrast to this, the X-rays generated by mildly relativistic electrons in the range of several tens of keV are comparatively easy to shield in a light-weight and compact setup. Therefore, we decided to restrict our design to an upper limit of the acceleration voltage of 100 kV.

The electron beam with the given specifications needs to be transported through the waveguide. To preserve a good overlap between the electrons and the evanescent-type wave modes, the transport should be accurate enough to maintaining a gap smaller than typically a millimetre between the electrons and the liner. For this task we have designed a solenoid, which can provide a sufficiently strong and homogeneous axial field in the lined waveguide, and which preserves the 2 mm diameter of the electron beam. Former work [77] had shown that for such a transport system the gap between electrons and liner may even be as small as half a millimetre.

In summary, to obtain a compact design for a CFEL we limited the total current to 800 mA, the maximum acceleration voltage to 100 kV, and aim on a small electron beam diameter of 2 mm.

4.2 Lined waveguide

In the present section, given the above stated specifications of the electron beam, we investigate the properties of the liner that should best meet the requirements for laser amplification at the nominal frequencies of interest (22 GHz in the K-band and 50 GHz in the V-band). More specifically, we select a suitable type of liner material and the dimensions of the lined waveguide.

Since the first demonstration of stimulated Čerenkov radiation, where the waveguide was loaded with lucite and with polyethylene [44], many different materials have been used in experimental CFELs. Some examples are boron nitride [48], polymethylpentene (TPX) [64], quartz [47], quartz lined with mylar [78], sapphire [65] and polyethylene [79]. Here, in order to find the best suited material for the liner and its dimensions, we refer to the dispersion diagram (figure 2.3, chapter 2) where the crossing point between the electron beam line and the mode dispersion line determines the frequency of emission. To find a suitable crossing point, two basic conditions must be fulfilled. First, the phase velocity at such cross point must be larger than the phase velocity in the dielectric (Čerenkov threshold). Second, the phase velocity of the wave at the cross point should be considerably smaller than c_0 (synchronization with mildly relativistic electrons).

Fulfilling the first condition depends only on the dielectric constant of the material. One can see in equation 2.1 in chapter 2 that the threshold Čerenkov velocity varies with the inverse of the square root of the dielectric constant. When inserting numbers one finds that a dielectric

constant below 5 requires an acceleration voltage already larger than our upper design limit of 100 kV. Thus the liner should have a dielectric constant above 5. In addition, a working CFEL requires the material to have adequate strength, low temperature expansion coefficients, and acceptable low surface desorption rates. Following those criteria, we have chosen alumina (Al_2O_3), and clear fused quartz doped with titanium oxide, namely, GEquartz 219 [80]. There can be some variation in the dielectric constant of alumina in a range between 8.2 and 10.5 [76] depending on the quality of the material, the temperature and the frequency. However, for definiteness, here we assume an ϵ of 9.8 [76]. Such variations do not have a significant influence on the gain and output of the laser but they would slightly shift the frequency of the output. These issues will be discussed in chapter 6. For the GEquartz 219, the specified dielectric constant is $\epsilon_r = 5.8$.

Fulfilling the second condition depends on the material and on the inner and outer radii of the liners. The suitable radii can be derived from plotting the wave dispersion as in figure 2.3 for a number of liner materials and liner thicknesses. One observes that the larger the dielectric constant and the thicker the liner is, the slower the wave travels. For a choice between alumina and quartz to generate a fixed frequency, the alumina should be thinner than the quartz. A thin liner offers the advantage that the evanescent wave penetrates deeper into the vacuum region where the electron beam propagates, serving for a better pump overlap. A drawback of a thin liner is that the variation of resonance frequency with the liner thickness is also larger for thin liners, which might lead to problems with fabrication tolerances. In order to provide a good trade-off between these two effects we decided to use a 1.3 mm thick quartz liner for the 50 GHz range and a 1.5 mm alumina liner for the 22 GHz range.

The lower limit on the inner radius is imposed by the 2 mm electron beam, and the desired 0.5 mm gap between the electron beam and the liner. We thus choose for the quartz an inner diameter of 3 mm. As it will be later shown, during the characterization of the electron beam transport with the first experimental CFEL, which was lined with quartz, we found that a fraction of the electron beam was lost in the walls of the liner (see chapter 6). In order to reduce the loss of current in the walls of the liner, it was chosen an inner diameter of 4 mm for the alumina for the second experimental CFEL.

4.3 Emission properties

In the following we calculate the wave amplification by the CFEL, for which we use the equations of the evolution of the field amplitude given in chapter 2, with the electron beam specifications and liner specifications described in the previous sections. The goal of these calculations is to find suitable design values for the remaining laser parameters which are, *e.g.,* the required

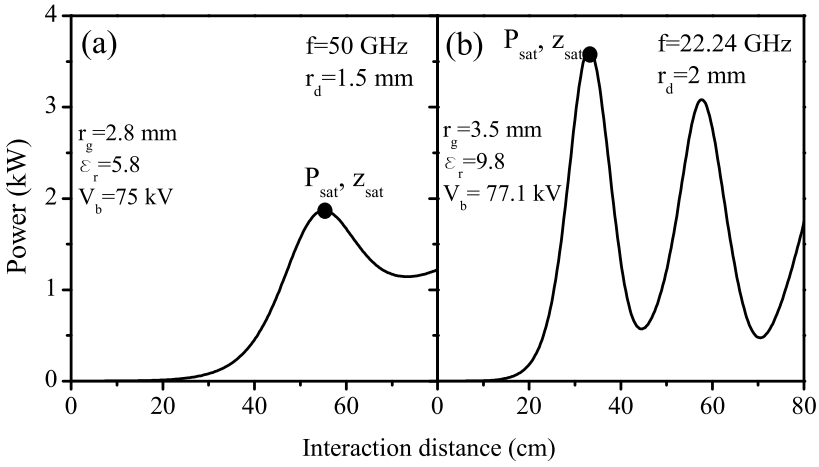

Figure 4.1: Power as a function of the propagating distance for 50 GHz (a) and for 22.24 GHz (b). In both cases, the tangent loss is of 10^{-5}, the power of the input seed is of 1 μW and the electron beam current is of 800 mA.

length of the waveguide and the required amount of feedback for a laser resonator, for low threshold operation as laser oscillator. For the nominal frequencies of 50 GHz and 22 GHz we first calculate the power amplification in a single pass through the amplifier when a weak probe wave (seed or probe wave) is injected. Then, we study the influence of different losses present in the CFEL, specifically, the tangent losses of the dielectric liner and fluctuations in the liner radius caused by fabrication errors, as well as the energy spread in the electron beam. Next, to investigate the possibility of reducing the size, we study the CFEL configured as an oscillator. Finally, we describe the emission properties within a spectral range around 50 GHz and 22 GHz.

4.3.1 Single-pass amplification

The calculation of wave amplification in the CFEL is done by numerically integrating the equations that describe the evolution of the field amplitude presented in chapter 2. For the liners of quartz and alumina and the electron current of 800 mA, we have first calculated the amplification in the CFEL for negligible losses and negligible fluctuations of the liner and for a beam energy spread of 1 %. For a calculation of the single-pass amplification we have assumed a weak input seed wave of 1 μW power at 50 GHz for the quartz-lined CFEL and of 22 GHz for the alumina-lined CFEL. Figure 4.1 (a) and (b), shows the calculated microwave power as a function of the interaction length in the waveguide for 50 GHz (75 kV) and 22.24 GHz (77.1 kV), respectively. One can see in figure 4.1 (a) that at 50 GHz, the CFEL should achieve a saturated output power, P_{sat}, of almost 2 kW after an interaction length, z_{sat}, of about 62 cm.

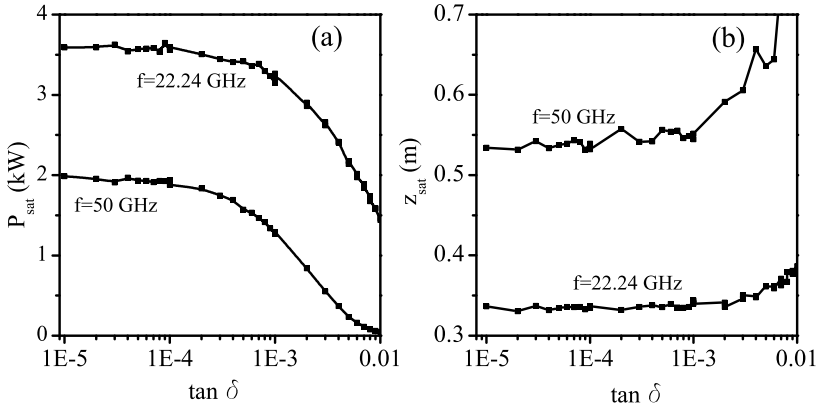

Figure 4.2: Saturated power (a) and distance to saturation (b) for 50 GHz (at 75 kV) and 22.24 GHz (at 77.1 kV) as a function of the tangent loss of the dielectric liner. The electron beam current is 800 mA.

Although this is an appreciable output power, this comes at the expense of a somewhat long interaction distance. When the CFEL is desired to be shorter by roughly a factor of two, a choise is to be made. For example, when the waveguide is shortened to 25 cm, one would either have to tolerate a much smaller ouput in a single pass or the CFEL could be configured as an oscillator. This oscillator configuration will be investigated later in this chapter. In figure 4.1 (b) one sees that, at the lower frequency of 22.24 GHz, the CFEL should reach a substantial output power of about 3.5 kW already after an interaction length of about 40 cm and the CFEL should still reach a few tens of watts in a single pass over a shortened interaction length of 25 cm.

In summary so far, the shown results look rather promising, particularly, when considering that they were obtained with a rather small electron beam current of 800 mA, and a very modest acceleration voltage of around 75 kV.

4.3.2 Dielectric losses and liner fluctuations in the liner and energy spread of the beam

It can be expected that the single-pass saturated power calculated in section 4.3.1 would become reduced to some degree due to several types of losses that may be present in a CFEL. We have derived in chapter 2 an extended theoretical model that allows to include two specific types of losses, namely, dielectric losses in the liner, and fluctuating liner radius along the propagation distance. In contrast to this, the reduced output power as effect of an energy spread in the electron beam is well known [55]. In the present section, we investigate CFEL amplification under the presence of these three types of losses. To quantify and compare the effects with ideal

(loss-free) single-pass amplification as given in section 4.3.1, we calculate again the saturated power P_{sat} and the distance to saturation z_{sat}.

The effects induced by the dielectric losses in the liner are calculated for negligible liner fluctuations and for an energy spread of 1 %. Figures 4.2 (a) and (b) show the saturated power P_{sat} and the distance to reach saturation z_{sat}, respectively, as a function of the tangent loss of the liner. The calculations are done for a voltage of 75 kV for 50 GHz and 77.1 kV for 22.24 GHz. We have chosen to vary the tangent loss over a large range starting with a small value of 10^{-5}, where the influence of losses can be neglected, up to a rather large tangent loss of 0.01. Such upper limit may seem unrealistic on the first view but we use it here to obtain a more complete information of the sensitivity of the CFEL over a broad range of dielectric losses. To estimate the expected output power in the experimental CFEL, we consider that the tangent loss for the quartz and for the alumina are below 10^{-3} as was specified elsewhere [81, 82]. However, we note that a radiation-induced heating of the liner, or collisions of a small part of the electrons in the pump beam, might modify the tangent loss to higher values. One can see in figure 4.2 (a) that, as expected, an increase in the tangent loss always leads to a decrease in the saturated power. For 50 GHz, the power is approximately reduced by 50 %, from 2 kW for negligible losses to about 1 kW for a tangent loss of 10^{-3}. For 22 GHz, one can see that the power reduces only by 15 %, from about 3.5 kW for negligible loss to about 3 kW for the same tangent loss of 10^{-3}. Regarding the distance to saturation, one can see in figure 4.2 (b) that, in both cases, an increase in the tangent loss increases the distance to saturation. However, it can be seen that z_{sat} does not noticeably increase as long as the tangent loss is below about 10^{-3}.

The effect of the liner fluctuations on the saturated power and on the saturation distance is calculated with the same procedure described in chapter 3, now for a negligible dielectric loss in the liner and again for an energy spread in the pump beam of 1 %. As was described there, we use a random fluctuation of the inner liner radius superimposed on the average inner radius r_{d0}. Further, as before we use a spatial low-pass filter with a certain cut-off length z_c to remove spatially fast fluctuations from the random distribution. For such a randomly radius distribution the liner is then characterized by its rms value of radius fluctuation, σ_{rd}, and its cut-off distance, z_c. For both liners (quartz and alumina), we choose a cutoff-length of $z_c = 10$ cm, *i.e.*, we assume that the liner is nearly perfect on a scale smaller than 10 cm. As explained in chapter 3, to obtain statistical information of the output as a function of liner fluctuations, we generate an ensemble of 100 different realizations of a random liner for each combination of the rms fluctuations amplitude and cut-off distance. For each combination we determine the ensemble average $\overline{P_{sat}}$ and its standard variation, σ_{Psat}, and the corresponding values for the distance to saturation, $\overline{z_{sat}}$ and σ_{zsat}. Regarding the strength of fluctuations expected in liner fabrication, we note that the tolerance of the liner radius of a standard tube can be as

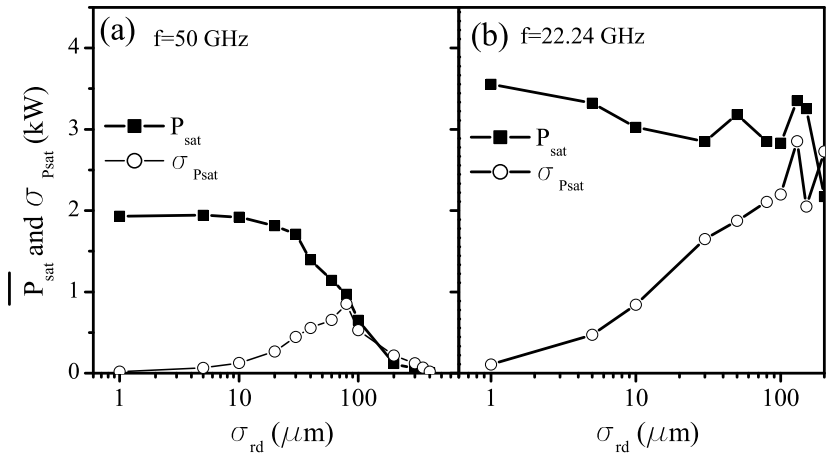

Figure 4.3: Saturated power for 50 GHz (a) and 22.24 GHz (b) as a function of the rms value of the liner fluctuations. The electron beam voltages are 75 kV (a) and 77.1 kV (b). In both cases, the electron beam current is 800 mA. Lines are for guidance.

high as 10 %, which corresponds to an rms fluctuation of 150 μm for the quartz liner and of 200 μm for the alumina liner. Precision tubes have smaller tolerances of down to 3 %, which corresponds to rms fluctuations of 45 μm for the quartz and 60 μm for the alumina liner. In order to consider the named tolerances of commercial tubes, we choose to vary the rms value of the liner fluctuations up to a maximum value of 200 μm. The figures 4.3 (a) and (b) show the ensemble average $\overline{P_{sat}}$ and the standard variation $\sigma_{P_{sat}}$ as a function of the rms value of the liner fluctuations for the quartz-lined CFEL (at 50 GHz) and the alumina-lined CFEL (at 22 GHz), respectively. Figure 4.3 (a) shows that, for the tolerance levels of standard tubes, the saturated power of the quartz-lined CFEL may be strongly reduced from 2 kW to about 300 W. The figure also shows that even for high precision tubes, the saturated power is reduced by 50 % to about 1 kW. These results indicate that the quartz-lined CFEL is very sensitive to the liner fluctuations and, therefore, the quartz-lined CFEL should indeed use a spacial high precision tube to avoid a large decrease of the power. In figure 4.3 can be seen that the spread in the saturated power, which results from the different realizations of the liner fluctuations, increases strongly to almost 100% of the maximum output for standard tubes. This indicates that the output power is almost impossible to predict for such high liner fluctuations. Figure 4.3 (b) shows that, for a standard alumina tube, the output power decreases from about 3.5 kW to about 3 kW, *i.e.,* the fluctuations in the alumina tube do not induce such a severe reduction of the output power in the alumina-lined CFEL. However, for such high rms value of the fluctuations, the spread in the saturated power still almost reaches the average output power pointing to a poor predictability for the laser output. Again, the spread on the results can be diminished

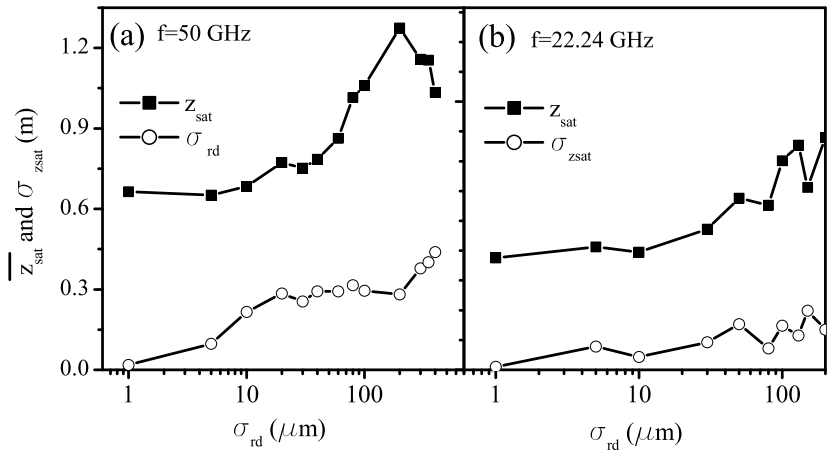

Figure 4.4: Distance to saturation for 50 GHz (a) and 22.24 GHz (b) as a function of the rms value of the liner fluctuations. The electron beam voltages are 75 kV (a) and 77.1 kV (b). In both cases, the electron beam current is 800 mA. Lines are for guidance.

by using a precision tube for the alumina liner. In that case, the power reduces from 3.5 kW (without fluctuations) to about 3.2 kW for a rms fluctuation of 60 μm, which corresponds to only a small reduction of the power by about 6 %.

Figures 4.4 (a) and (b) show that both the average interaction length required for saturation, $\overline{z_{sat}}$ and its standard deviation $\sigma_{z_{sat}}$, increase with increasing liner fluctuations in both configurations of the CFEL. A standard tube for the quartz liner may even result in an increase of z_{sat} from 60 cm to about 1 m and also with a precision tube z_{sat} increases considerably to approximately 80 cm. A standard alumina tube would induce an increased distance to saturation of about 70 cm and a precision alumina tube an increase from 40 cm to 60 cm. Although such increments of the saturation distance may still be considered as modest, especially, when the CFEL is designed as an oscillator, they certainly need to be taken into account as a relevant design criterion for CFELs for an amplifier configuration.

Finally, the effects induced by the beam energy spread on the saturated power and on the distance to saturation are calculated for negligible liner fluctuations and negligible dielectric losses in the liner. The energy spread in the electron beam can have different causes, *e.g.,* a temporal ripple in the voltage of the used power supply or a poorly designed electron transport that would induce a larger transverse velocity component to a fraction of the electron beam. In the description of the experimental setup later in chapter 5 we will estimate the magnitude of such effects. Here, to study the basic effect of velocity spread, we choose to vary the energy spread in a range from 1 % to 10 %. Figures 4.5 (a) and (b) show the saturated power P_{sat} and the distance to reach saturation z_{sat}, respectively, as a function of the beam energy spread. The

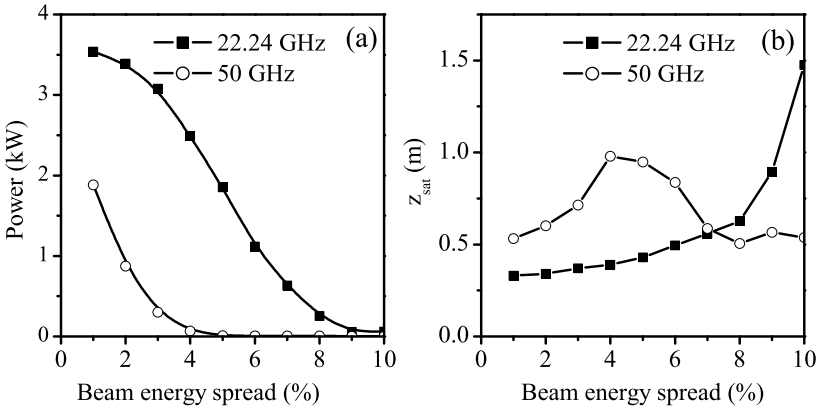

Figure 4.5: Saturated power (a) and distance to saturation (b) as a function of the energy spread of the electron beam for 50 GHz (at 75 kV) and 22.24 GHz (at 77.1 kV). In all cases, the electron beam current is 800 mA. Lines are for guidance.

calculations are done for a voltage of 75 kV for 50 GHz and 77.1 kV for 22.24 GHz. One can see in figure 4.5 (a) that, for the quartz-lined CFEL, already a 5 % energy spread reduces the saturated power from 2 kW to zero. Regarding the distance to saturation, figure 4.5 (b) shows that, for the quartz liner, an energy spread of only 4 % doubles the distance to saturation. Such results indicate that the quartz-lined CFEL is very sensitive to fluctuations in the energy of the electrons and that, to retain much of the ideally possible output, a spread of 1 to 2 % is to be maintained.

Figure 4.5 (a) shows that the same energy spread of 5 % that fully would suppress the emission for the quartz liner, only reduces the saturated power from 3.5 kW to about 2 kW for the alumina liner, while the distance to saturation remains constant below approximately 5 % energy spread. Therefore, the output performance of the alumina-lined CFEL appears relatively robust versus an increased energy spread in the electron beam.

In summary, the operation of the CFEL at 50 GHz with the quartz liner is more sensitive to all types of losses than the operation of the CFEL at 22 GHz with the alumina liner. If losses are not within the limits derived in the results above, a lasing of the quartz-lined CFEL may fail. For the alumina-lined CFEL, the constraints are more relaxed and also a higher efficiency of the CFEL is expected.

4.3.3 Oscillator configuration

In section 4.3.1 we have calculated the single-pass amplification for two CFELs configurations and we have seen that for the quartz-lined CFEL the distance to saturation is more that 60 cm,

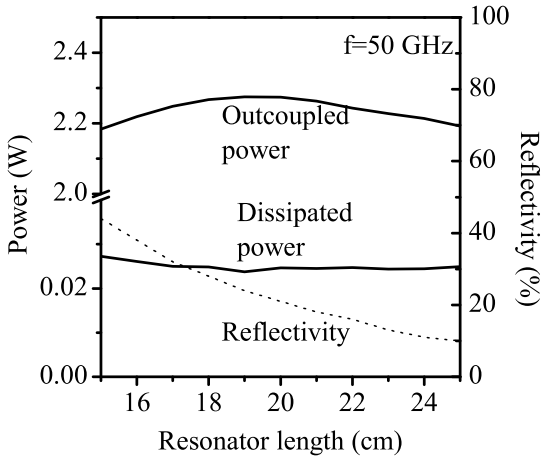

Figure 4.6: Maximum power and dissipated power as a function of the resonator length for 50 GHz. The reflectivity required for outcoupling maximum power is also indicated for every length. The electron beam voltages is 75 kV and the beam current is of 800 mA. The dielectric losses and the liner fluctuations are neglected.

increasing further when losses are present. This long distance makes it more difficult to design an appropriate electron beam transport and it increases the size of the CFEL. A solution to both problems is to configure the CFEL as an oscillator by reflecting part of the radiation back into the waveguide causing multiple round trips such that the waveguide can be shortened. In practice, the ends of the waveguide always show some impedance mismatch for propagating radiation producing reflection and, therefore, no CFEL works as a true single-pass amplifier without special measures taken. Therefore, as a general classification one can say that when the length of the interaction is large enough to reach saturation at or near the end in a single pass, the CFEL is mainly working as an amplifier. When the interaction length is much shorter than the distance to saturation and the reflection is controlled to provide a macroscopic output, the CFEL is mainly working as an oscillator. In the following, we investigate the outcoupled power from the CFEL when the length of the waveguide is reduced and controllable feedback is used to design the CFEL as an oscillator.

In a CFEL oscillator with a standing wave resonator, the wave counterpropagates to the electron beam in the second half of each round trip within the resonator. During this backward travelling, the wave does not fulfil the phase matching condition, which means that the wave amplification is uni-directional, occurring only for the wave copropagating with the electron beam. A simple calculation shows that during an electron current pulse of, *e.g.,* 10 μs, the wave performs in the order of 10^3 round trips for a cavity length of about 25 cm. Therefore, it is sufficient to consider the steady-state solution of the interaction, such that in the beginning of each round trip, the wave interacts with non bunched electrons. The bunching of the electrons then

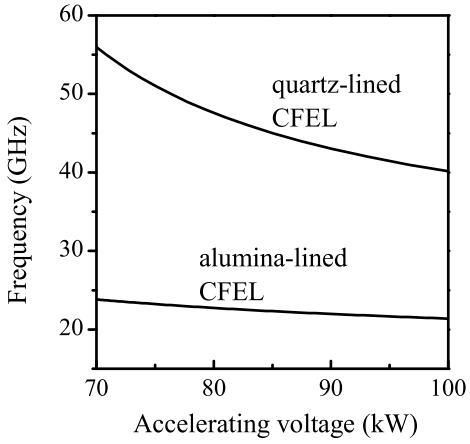

Figure 4.7: Tuning curve of the quartz-lined CFEL and of the alumina-lined CFEL.

continuously occurs at a certain interaction length, which depends on the steady-state power distribution of the wave.

The outcoupled power in the oscillator CFEL, as in any laser oscillator, is maximum for a certain reflectivity of the downstream mirror. Additionally, the gain medium in a CFEL offers a specific gain per unit length. As a result, the maximum output power also depends on the length of the liner. In order to determine the optimum liner length and downstream mirror reflectivity, we have calculated the outcoupled power and the intracavity dissipated power for various liner lengths and total mirror reflectivity. The outcoupled power is determined in the following way. For a given liner length, we calculated the single pass gain for a range of input powers starting from the noise level up to the saturated power. Next, we represent the resonator by a simple feedback model that starts with a seed power corresponding to the noise level. The corresponding single-pass gain is used to determine the intracavity power. Then, corrected for the total reflectivity of the resonator, this power is used as a seed for the next round trip. This process is repeated until a steady state is reached, *i.e.,* the single-pass gain equals the total round-trip loss. Using the same single-pass gain data, various values of reflectivity of the resonator can be investigated without recalculating the gain of the CFEL. A different length of the liner requires recalculation of the single-pass gain as a function of the input power. In this way, we calculate the outcoupled power for various resonators having different liner lengths and different amounts of outcoupling. Figure 4.6 shows the maximum output power and the dissipated power inside the waveguide as a function of the length of the resonator for 50 GHz. The figure also shows the reflectivity necessary for achieving such outcoupled power for each length. One can see in figure 4.6 that, for the quartz-lined CFEL, a resonator length of only 20 cm provides the highest output power of almost 2.3 kW. We also see that the outcoupled

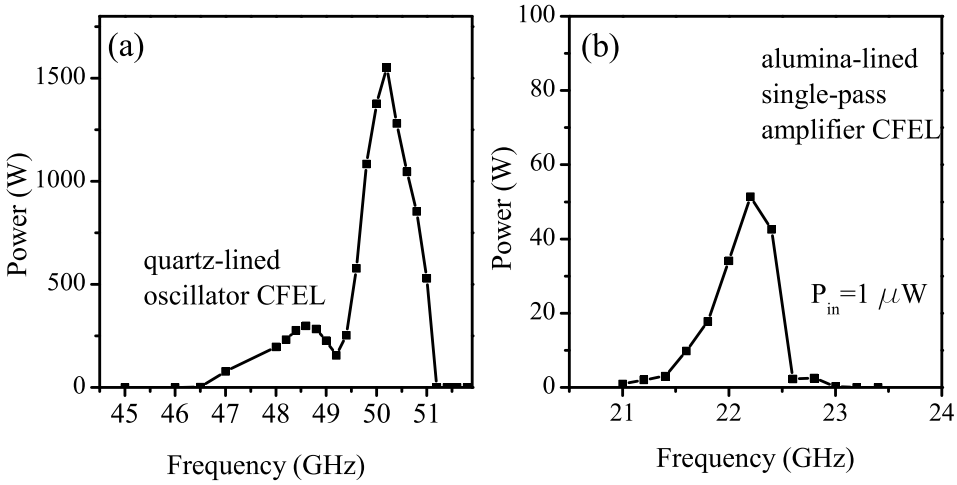

Figure 4.8: Calculated gain bandwidth of the oscillator CFEL at 75 kV (a) and of the amplifier CFEL at 77.1 kV (b). For both cases, the dielectric losses and liner fluctuations are chosen as negligibly small. The energy spread of the beam is chosen as 1 % and the electron beam current is 800 mA. Lines are for guidance.

power even decreases with a longer waveguide. To minimize the heat dissipation in the liner, with the goal to lower its temperature, it would be appropriate to keep the intra-cavity power as low as possible by providing a relatively small feedback. One can see in figure 4.6 that the reflectivity for maximum output power decreases for longer waveguides. To provide a good compromise between minimum heat load on the liner and maximum output power, we select for our design with the quartz liner (50 GHz) a waveguide of 25 cm length, with only about 10% reflectivity and which still provides about 2.2 kW of outcoupled power.

4.3.4 Tuning properties

One of the most attractive features of the CFEL is the possibility of an easy and quick tuning the frequency of the emitted radiation over wide ranges, which can simply be done by varying the accelerating voltage of the electron beam. Therefore, it is of interest here to determine the bandwidth over which the laser can be tuned within the operating voltages provided by voltage changes. For this, we have solved the dispersion relation for the quartz- and the alumina-lined waveguide. Then, for each accelerating voltage, we calculated the frequency of maximum gain corresponding to the crossing point between the electron line and the mode line obtaining thus the frequency of resonance as in figure 4.7. One can see that a voltage sweep from 70 to 100 kV produces an almost full spectral coverage of the range between 40 and 60 GHz for the quartz-lined CFEL and of about 2 GHz tuning for the alumina-lined CFEL.

4.3.5 Gain bandwidth

In the previous sections we have calculated the maximum power that can be coupled out of the CFEL for the two nominal frequencies of operation, *i.e.*, for 50 GHz and 22 GHz. In this section we calculate the outcoupled power for a fixed acceleration voltage and for frequencies around the resonating frequency, *i.e.*, we calculate the gain bandwidth of the CFEL.

The quartz-lined CFEL is designed as an oscillator and, therefore, to determine the outcoupled power within the gain bandwidth one first has to specify any frequency dependence of the reflectivity of the downstream mirror. The design of the downstream mirror is described later in chapter 5, and it shows that the reflectivity is, indeed, highly dependent on the frequency of the radiation. In order to calculate the outcoupled power, in the present chapter we use the reflectivity data of the downstream mirror that will be presented in the chapter 5. The result is given in figure 4.8 (a), which shows the output power as a function of the frequency. One can see that the power has a maximum of about 1.5 kW at approximately 50 GHz and that the FWHM is about 1 GHz.

For the alumina-lined CFEL, we have calculated the power in a single-pass through a 25 cm long waveguide for frequencies between 21 GHz and 24 GHz and the result is shown in figure 4.8 (b). The calculation is done for a fixed voltage of 77.1 kV and a fixed seed input power of 1 μW, which we assume to be approximately equal to the noise level of electromagnetic power inside the lined waveguide. One can see that the FWHM is about 1 GHz with a maximum of about 60 W at approximately 22.3 GHz. As for the 50 GHz oscillator, the 22 GHz single-pass device only needs a few percent reflected power to drive the laser into saturation and then, the output power will be of the order of the saturated power in a single-pass, *i.e.,* 3.5 kW.

5

Experimental set-up

Abstract

In this chapter, the experimental design and setup of the CFEL is described. First, we present the design of the cathode and the electron gun structure, which provides a 10 kV and 800 mA electron beam of 2 mm diameter. Then, we describe the electrical circuit used to accelerate this beam to the 70-100 keV energies required for CFEL operation. Also, we describe the magnet used to inject the electron beam into the lined waveguide and to transport the beam through the lined waveguide. Finally, we describe the design of the outcoupler for the radiation where also the electron beam is separated from the radiation. The result is an experimental setup that fulfils the requirements for wave amplification given in the previous chapter and that is ready for operation.

In the previous chapters we have presented a detailed theoretical investigation of the output power expected from a CFEL. In particular, the study has resulted in the specifications for a compact source that can achieve several hundreds of watts when configured as an oscillator and some tens of watts when configured as a single-pass amplifier. In this chapter, we describe the experimental setup designed and built to realize a working CFEL.

The experimental setup of the CFEL combines the design of an accelerating and guiding structure for the electron beam and the design of waveguides for the microwave propagation with feedback and output coupling. Therefore, the design integrates elements of electron beam physics and of microwave engineering. Figure 5.1 shows an overview of the experimental setup of the designed CFEL which comprises an electron gun, a high-voltage network to accelerate the electron beam, a lined waveguide for the interaction and an outcoupler of the radiation. The left-hand part of the figure shows the electron gun chamber, where the electron beam is generated and accelerated. Next, the electrons are guided along the axis of the lined waveguide by means of a solenoid (not shown in the figure). Finally, the right-hand side of the figure shows the downstream mirror, which is used to outcouple the radiation. Section 5.1 describes the electron gun and section 5.2 describes the elements concerning the acceleration and propagation of the

electron beam. Next, section 5.3 describes the outcoupler of the radiation. Finally, section 5.4 presents the hardware and software tools used as interface with the experimental setup.

5.1 Electron gun

The small electron currents to be used in the CFEL allow for a compact and small electron gun. A further reduction of the size of the gun was achieved by choosing a low-voltage gun and, instead, let a second acceleration stage follow with a high voltage. As source for the electron beam, we have chosen a thermionic dispenser cathode integrated in a 10 kV electron gun. In the following, we present the physical mechanisms for electron emission in the dispenser thermionic cathode, and next, we present the design of the entire electron gun structure.

5.1.1 Cathode

The used dispenser thermionic cathode is an M-type cathode with an osmium-ruthenium layer. This type of cathode demands clean vacuum conditions, where a partial pressure of 10^{-7} mbar for oxygen, $3 \cdot 10^{-7}$ mbar for water vapour, 10^{-6} mbar for CO_2 and $5{\cdot}10^{-6}$ mbar for air should not be exceeded [83]. To understand the underlying physical processes of the emission of the electrons and the need for these vacuum requirements, in the following we briefly describe the working principle and properties of thermionic dispenser cathodes.

There are two main mechanisms for the emission of electrons from a solid surface [84, 85]. One of the methods consists on using standard metallic cathode materials and supplying sufficient energy to the material such that the conduction-band electrons overcome the work function. Then, the electrons can be easily triggered with an additional voltage gradient to leave the cathode material. Based on the type of energy supplied, one can distinguish between thermionic cathodes where the cathode is heated [86], photocathodes where the cathode is irradiated with UV light of sufficiently high photon energy [87], and secondary emission cathodes where the cathode is irradiated with electrons [88]. The second method for electron emission consists on reducing the work function of the emission material down to the energy level of the electrons, which are then emitted without the need of an extra energy supply. Based on the way of reduction of the potential barrier, one distinguishes between field emission cathodes [89], where a strong electric field ($\approx 10^7$ V/m) is applied to the cathode surface, and explosive emission cathodes, where a plasma is formed at the cathode surface reducing the work function to zero.

There are many examples of thermionic emitters [86] such as oxide cathodes, Cermet cathodes, Thorium-, tungsten- and LaB_6-based cathodes, and dispenser cathodes. The dispenser cathode consists of a strongly-bonded continuous metallic phase of a refractory metal, scattered

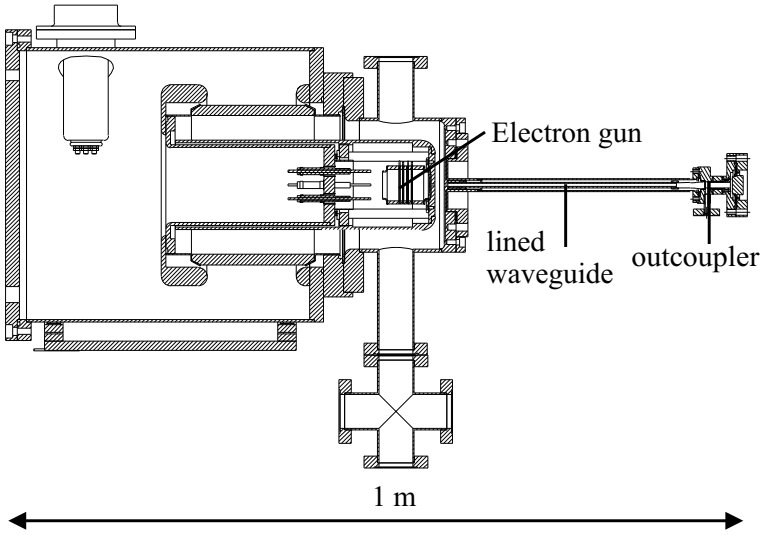

Figure 5.1: Overview of the experimental setup of the CFEL.

uniformly with an emitting material [90, 91]. The porous metal matrix acts as a reservoir from which the emitting material can diffuse to the surface to maintain a photoemissive layer with a low work-function for thermionic emission of electrons. A subgroup is formed by dispenser cathodes of the M family [92], which are fabricated from porous tungsten impregnated with barium calcium aluminate. The cathode is coated with a thin layer of osmium-ruthenium or osmium-iridium. The coating is done by sputtering, vapor deposition or ion plating to a thickness of 0.2-1 μm. After the coating, these cathodes are fired in a hydrogen atmosphere for several minutes to further sinter the coating into the tungsten substrate. When the cathode is heated, the barium calcium aluminate that impregnates the tungsten reacts with the tungsten releasing barium which travels through the pores to the surface of the cathode. There, the barium uniformly covers the surface with a monolayer [93]. This coverage and the metal substrate composition determine the surface work function. However, at the elevated temperatures of cathode operation, the barium would evaporate without a previous oxidation of the metal that leads to the formation of dipoles of barium and oxygen, binding this way the barium to the surface. The removal of any species that would otherwise compete with oxygen for the dipole site is known as activation of the cathode, and it is performed by overheating the cathode during a certain period of time. Thus, a fully activated surface needs to have every available site on its surface occupied by the barium-oxygen dipole. The adsorption of gas or metal vapour onto the surface would reduce the dipole effect of the electro-positive osmium-ruthenium layer (used to reduce the work function), especially when the adsorbed species are electro-negative. In this case, the work function would increase and reduce the emission current, a phenomenon usually termed emission poisoning. Below a certain threshold pressure, which is different for each type of gas and which decreases with the temperature of the cathode, no poisoning occurs.

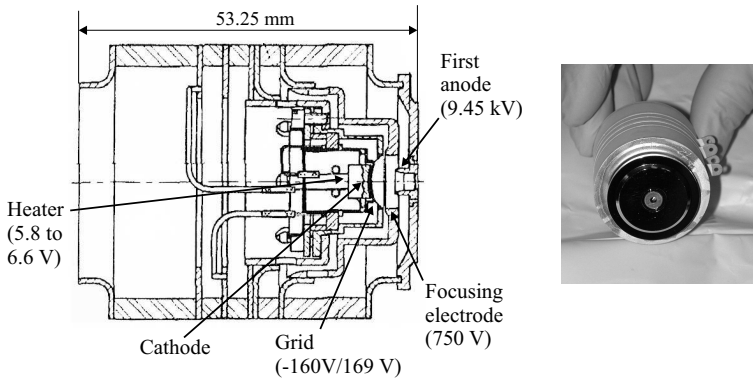

Figure 5.2: Section of the electron gun from e2v technologies. The cathode, heater and electrodes are labelled and the manufacturer operating specifications for each of them are shown. The voltages are given with respect to the cathode voltage. At the right side, a photograph of the electron gun.

The M-type cathodes have shown to have low sublimation rates of the impregnants, resistance to poisoning and long-term stability of emission [94]. The quality of the thermionic cathode as an electron source is determined primarily by the emission current, the energy spread in the emitted electrons, the poisoning resistance and the life time of the cathode. The emission current density J of a thermionic cathode is related to the operating temperature T and the electronic work function ϕ through the Richardson-Dushman equation [86]

$$J = AT^2 e^{-\frac{\phi}{k_B T}} \tag{5.1}$$

where A is the Richardson constant, which depends on the type of material, and k_B is Boltzmann's constant. When the emission current increases with the temperature according to equation (5.1), the cathode emission is said to be temperature-limited. For sufficiently high temperatures, the electrons in front of the cathode surface lower the externally applied field at the surface, resulting in a stabilization of the emission independent of the temperature of the cathode. This is called space-charge limited emission and has the advantage that a non-uniform temperature distribution at the cathode surface does not result in a non-uniform electron density within the electron beam. Therefore, the space-charge limited emission is the preferred regime of operation for a thermionic cathode. On the other hand, the temperature of operation determines the evaporation rate of barium from the cathode. After some operation time, due to depletion of the impregnating material, the barium must travel a longer distance to the surface. At some point, the transport of barium is insufficient to maintain an adequate barium coverage on the surface and emission begins to drop. One can increase the temperature to maintain the emission current, but this accelerates the depletion rate and the life of the cathode. Therefore,

the operating temperature must be chosen so that adequate space-charge limited emission is obtained at the minimum evaporation rate.

In summary, the operation with a dispenser thermionic cathode requires an activation and the selection of the specific temperature of operation. The characterization of these properties will be presented with the experimental results in chapter 6.

5.1.2 Structure of the 10-kV electron gun

While the cathode is the source of the electrons, the electron gun structure is responsible for forming the electron beam and for providing the initial acceleration of 10 kV. This initial acceleration stage forms the beam to a diameter of 2 mm. Here, we describe the characteristics of the electron gun, which has been designed by e2v Technologies [95] in a collaboration before we calculated the electron beam properties expected from such gun.

The electron gun is shown in figure 5.2. It follows the Pierce design [96] and also contains a focusing electrode to balance the space-charge force within the cathode-anode gap and to compress the electron beam, such that an electron beam with uniform current density is formed. To allow for generation of a pulsed electron beam, the electron source is equipped with a grid electrode very close to the cathode. This proximity has the advantage that only a few volts are required to suppress or start emission from the cathode. Due to the low voltage, a rapid on and off switching of the electron beam can be done in only a few nanoseconds, *e.g.,* to generate a nearly rectangular current pulse of microsecond duration. The cathode, the anode, the focusing electrode, the grid and the heater are integrated within a compact structure of 55 mm length. The electron gun is designed to provide a 2 mm diameter electron beam with a nominal electron current of 800 mA at an acceleration voltage of 10 kV.

For the design of the post-acceleration section, which will be presented in section 5.2, we have modelled the electron trajectories using the design provided by e2v Technologies and shown in figure 5.2. For that, we have used the Trak software from *Field Precision* [97]. Figure 5.3 shows a longitudinal-radial cross-section of the electron gun zoomed to the cathode and part of the grid, focusing electrode and anode, assuming cylindrical symmetry. The figure also shows the electrons trajectories calculated with the voltages for the anode, the focusing electrode, the grid and the heater recommended by e2v Technologies, which are also indicated in the figure with respect to the cathode voltage. The calculation also uses the magnetic field advised by e2v Technologies for proper injection of the electron beam. One can see that almost all of the electrons cross the 2 mm diameter aperture in the anode, while only a small fraction hits the anode and gets lost. From the calculations, the lost electrons amount to about 4 % of the total current. The manufacturer specifies a lower intercepted fraction of the beam at the first anode which may be due to the different models used for emission at the cathode surface.

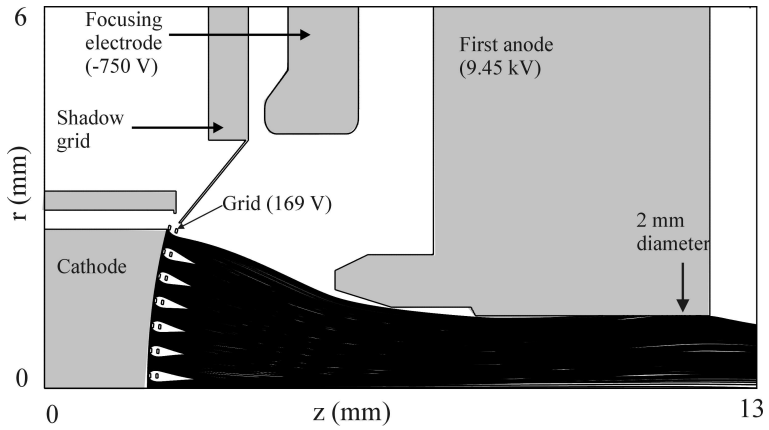

Figure 5.3: Longitudinal cross-section of the electron gun showing the result of the calculated trajectories of the electrons. The voltages used in the calculation are those indicated in the figure, which are given with respect to the cathode voltage.

5.2 Acceleration and transport of the electron beam

In order to use the electron beam in the CFEL, the 10 keV electrons require a post-acceleration to a maximum of 100 keV. Further, the electron beam is to be guided through the lined waveguide. In the following three sections we describe the electrical circuit to accelerate the electrons, the post-acceleration section that increases the beam voltage up to a maximum of 100 kV, and the transport of the electrons through the waveguide to the outcoupler structure.

5.2.1 Electrical circuit

The 10 kV acceleration of the electron beam is realized with a constant voltage, but to allow for a tuning of the frequency of the CFEL, the post-acceleration stage is designed for a variable voltage. The second anode, that provides the post-acceleration, is part of the vacuum chamber where the 10 kV electron source is mounted, and which is electrically isolated from the 10 kV source. For safety reasons, it is convenient to ground the second anode, which is physically accessible from the outside, and bias the first anode to a negative potential with respect to ground. The cathode voltage is then biased to -10 kV floating on the first anode potential. In such a way, none of the high voltage electrodes is accessible to the user.

The electrical circuit and the corresponding connections to the CFEL electrodes are schematically shown in figure 5.4. A negative-polarity 100 kV-30 mA power supply is used to bias the first anode. A 10 kV-30 mA power supply floating on the first anode potential is used to power the cathode at -10 kV with respect to the first anode. The remaining voltage supplies act on the focusing electrode, heater and grid and are floating on the cathode voltage. The focusing electrode uses a 3 kV-5 mA power supply and the heater and grid power supplies are home

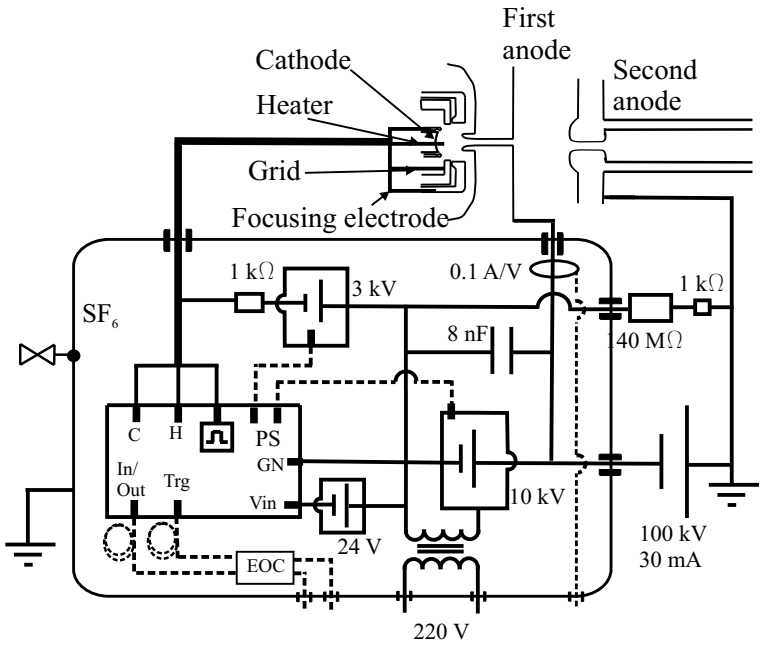

Figure 5.4: Electrical circuit for the injection and the acceleration of the electron beam.

built. All the power supplies are powered by an isolation transformer that provides 100 kV isolation to the 220 V mains connection. To make the floating high voltage power supplies physically inaccessible to the user, they are inserted into a grounded tank. The tank is filled with Sulphur Hexafluoride (SF_6) at 1.6 bar overpressure, which increases the breakdown field to about 10 kV/mm. Thereby the expected maximum voltage difference of 100 kV only requires a minimum of one centimetre of separation between elements.

The tank containing the floating power supplies has electrical feedthroughs both for the high-voltage and for the low-voltage input and output signals. Two high-voltage feedthroughs are, via two high-voltage cables, connected to each of the accelerating stages of the CFEL. Each cable contains 4 isolated conductors. One of the high-voltage cables is used for the cathode, the heater, the focusing electrode and the grid voltages. The four conductors of a single cable can be used for different elements because the isolation required between these voltages is only of a maximum of 10 kV. In the other high-voltage cable all the four conductors are used for the anode voltage. The low-voltage feedthroughs of the tank are used for the mains, for the communication between the control-system and the power supplies, and for diagnosis. A fibre optic provides the communication link and, at the same time, provides a 100 kV isolation between the low voltage input/output signal and the electronic controller, which is floating in high-voltage. This electronic controller communicates the PC-based external control system and the various floating power supplies and is used, *e.g.,* to set the voltages of the supplies. Additionally, the high-voltage isolation tank contains several diagnostic tools which are used

for measuring the total current that is extracted from the cathode with each pulse applied to the grid, and for measuring the electron current intercepted by the first anode.

5.2.2 Electron gun chamber

The electron gun chamber houses the electron gun and also forms the second anode to accelerate the beam and inject it into the waveguide. The design of the electron gun chamber must fulfil a number of requirements. First, the electrostatic field inside the chamber has to provide the correct acceleration profile in the gap between the first and second anode for the electron beam. Next, the pressure should be low enough for preserving the cathode. Last, the mechanical design has to allow for a proper aligning and for a simple assembling of the components. Figure 5.5 shows a longitudinal cross-section of the chamber and photographs of some of the details, which we use in the following sections as reference for the explanation. One can see that the total length of the chamber is only 50 cm. In the following, we show a description of the chamber based on figure 5.5 and then, an analysis of the electrostatic field distribution in the structure.

To preserve the vacuum conditions required by the cathode, the chamber is equipped with two vacuum ports, one of which is used for the connection to a dry high-vacuum pumping system, while the other is used to connect a sensor for monitoring the pressure. We use a two-stage and dry pumping system formed by a diaphragm and a turbomolecular vacuum pump. To monitor the chamber pressure we use a Bayard-Alpert ionization gauge (BAG) [98, 99]. The main components of the electron gun chamber are made from stainless steel 317L. However, to avoid excessive weight, the electric shield of the 10 kV electron source mounting structure is made from aluminium. To minimize the adsorption of gasses on the surfaces of the chamber, all components in direct contact with high field strength are electro-chemically polished.

The vacuum chamber, shadowed in figure 5.5, is actually formed by two parts, which are electrically isolated from each other by means of an aluminum oxide isolator. One of the parts, visible in figure 5.5 (a), contains the second anode and is grounded. The other part, visible in the figures 5.5 (b) and (c), contains the first anode and is floating on the first anode voltage, *i.e.,* at -90 kV with respect to ground. The edges of the ceramic isolator are equipped by corona rings to reduce the electric field strength in these areas, where the isolator and the metal are connected. To allow for alignment of the 10 kV electron source with the axis of this chamber, we have provided an adjustable mount for the 10 kV electron source, visible in figure 5.5 (d). The base of this adjustable mount also contains four high-voltage and ultra high-vacuum feedthrough connectors for the cathode, grid, focus and heater voltage. To connect the feedthrough connectors with the terminals on the 10 kV electron source we use wires of Oxygen Free High Conductivity (OFHC) copper isolated with ceramic beads, as can be seen in figure 5.5 (d). Finally, to provide a smooth electrical surface around the mount for the 10 kV

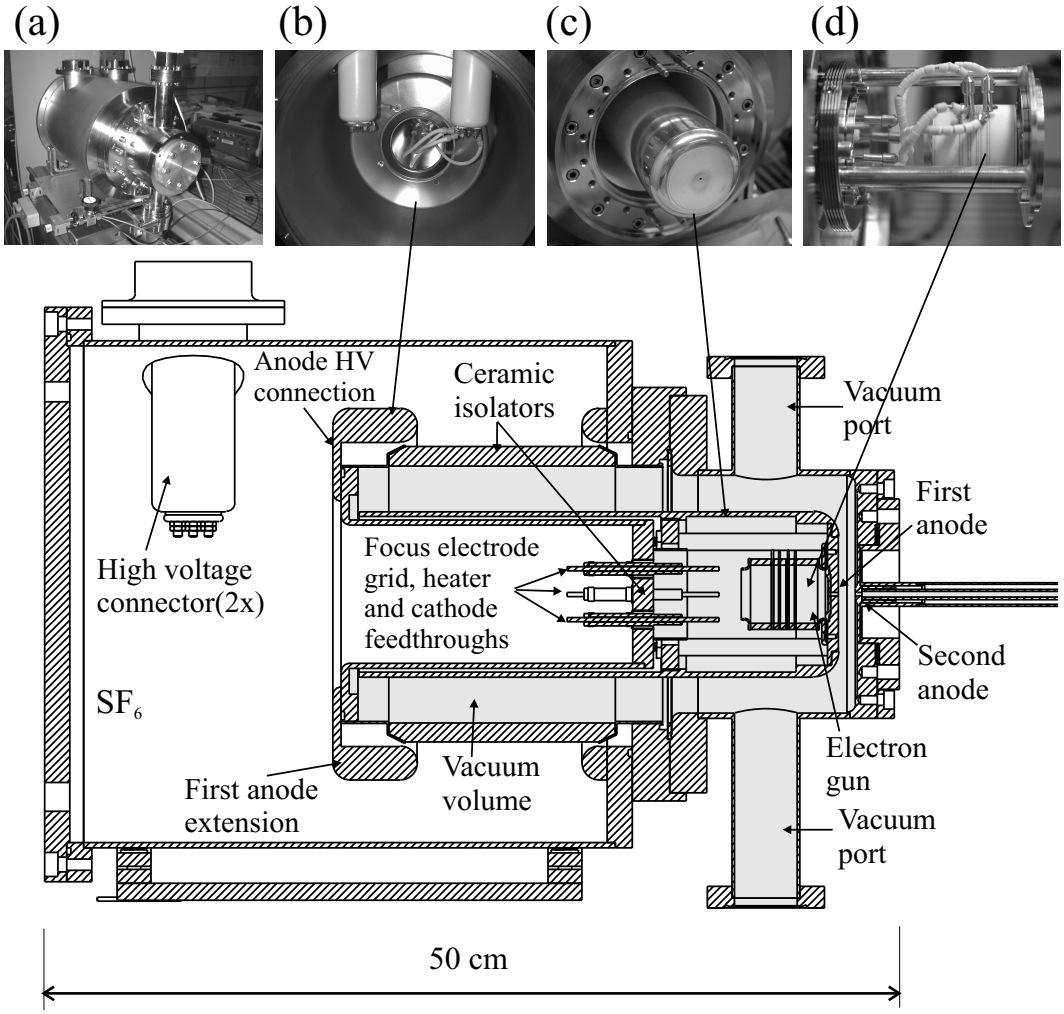

Figure 5.5: Longitudinal cross-section of the electron gun chamber with labels in each of the components. Also shown are the photographs of (a) the whole chamber, (b) detail of the first anode extension, (c) front part of the first anode, and (d) electron gun.

electron source, an aluminium shield is placed around the whole structure, as can be seen in figure 5.5 (c).

Breakdown discharges are one of the main issues in the electron gun chamber. To prevent breakdown discharges, the surfaces exposed to high electric field strengths are electrochemically polished, which improves the resistance against field emission, and the distances between electrodes at different potential are chosen above the corresponding breakdown voltage threshold. To further increase the breakdown voltage, the non-vacuum volumes of the electron gun chamber are filled with SF_6 at 1.6 bar, which at this pressure has about the same breakdown field strength as commonly used transformer oil. To have quantitative data of the electrostatic fields inside the chamber, we have calculated the electrostatic field distribution using the software EStat 6.0 from *Field Precision* [97]. Figure 5.6 shows a longitudinal cross-

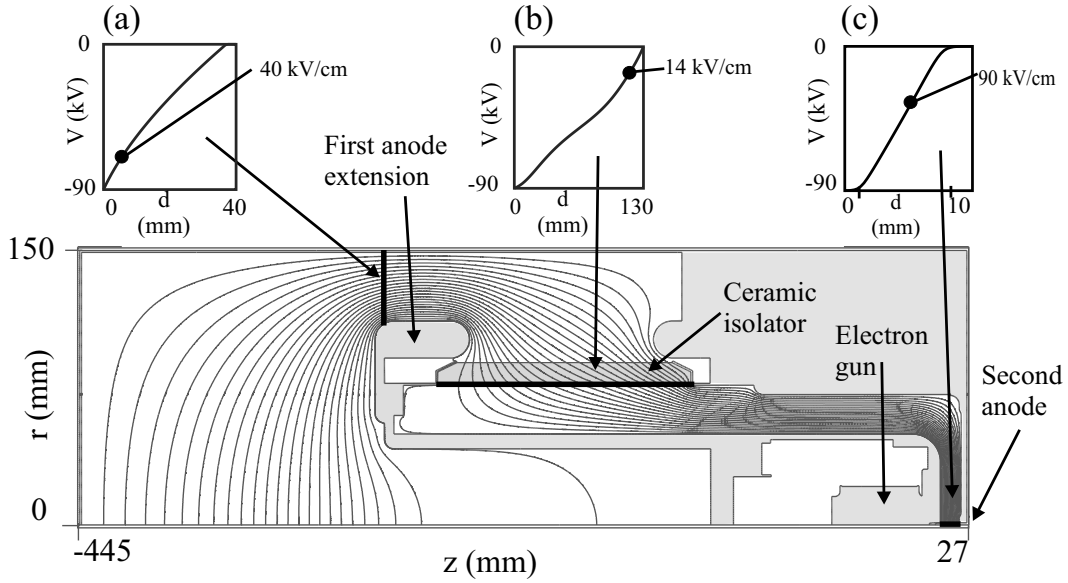

Figure 5.6: Longitudinal section (cylindrical symmetry is assumed) of the electron gun chamber, showing the equipotential lines of the electrostatic field. The insets show the voltage as a function of the distance between (a) first anode extension and walls of the chamber, (b) edges of the ceramic isolator and (c) first and second anode. We have used a voltage of the first anode of 10 kV and a voltage of second anode of 100 kV, both with respect to the cathode voltage.

section of the whole chamber assuming cylindrical symmetry with the resulting equipotential lines when applying the voltages of operation of the CFEL, as indicated in the caption of the figure. One can see that the largest field strength occurs in the gap between the cathode and the anode. One can also see that the corona rings at either side of the isolator help to control the field gradients near the ends of the isolator. A discharge along the surface of the ceramic isolator requires usually a lower field strength compared to a bulk discharge in vacuum and, therefore, the design avoids large values in the tangential field strength on the isolator surface. To further quantify the field strength in such areas of higher risks, figure 5.6 also contains three insets that show the voltage as a function of the distance along three lines marked in the cross-section and which correspond to (a) the gap between the first anode extension and the outer wall of the chamber, (b) the surface of the ceramic isolator and (c) the gap between the first and second anode. Figure 5.6 (a) shows that the maximum field strength between the first anode extension and the wall is of 40 kV/cm. Since this chamber is filled with an absolute pressure of 1.6 bar SF_6, the field strength is well below the threshold voltage and we do not expect any problem here. Regarding the ceramic isolator, it has a length of 11.4 cm and it is rated for voltages up to 75 kV in air, so the average field strength that it can support in air is 6.5 kV/cm. Figure 5.6 (b) shows that the maximum field strength is 14 kV/cm. Although this value is higher than the 6.5 kV/cm average field strength in air specified by the manufacturer, we use SF_6 at 1.6 bar

pressure which should improve the manufacturers specification considerably. Therefore, the isolator is expected to withstand the higher field strength along its surface and we expect no problems with this component. Finally, the most critical zone is in the gap between the cathode and the anode since to focus the electron beam into the waveguide, the distance must be relatively small. Figure 5.6 (c) shows that the design compromise distance of 10 mm between the first and the second anode restricts the maximum gradient to 90 kV/cm. This field strength is well below the breakdown threshold in vacuum, which is usually around 200-300 kV/cm [100]. Therefore, the distance of 10 mm here should be adequate to avoid any discharge.

5.2.3 Electron beam transport

Due to their charge, the electrons are copropagating in a parallel beam only under the application of external forces, such as an external magnetic field, since otherwise the space-charge forces would let the beam diverge. The magnetic field induces helical trajectories on the electrons with the axis of the helix parallel to the magnetic field direction. If the magnetic field strength is high enough, the electron trajectories can be approximated by a linear trajectory following the magnetic field lines. To generate such magnetic field, we chose a solenoid because it is simple, of low-cost and allows for an easy change of the field by simply varying the flowing current.

To design the solenoid, we used the specifications from the electron gun manufacturer, which give the magnetic field necessary to focus the beam in the gap between first and second anode, and to transport it through the aperture in the second anode. The magnetic field is shown in figure 5.7 (b) as solid line. This figure shows the magnetic field strength as a function of the distance on the axis of the CFEL, where $z = 0$ corresponds to the cathode position. The slope of the magnetic field profile near the cathode surface is responsible for focusing and balancing the space-charge forces in the post-acceleration section, while the plateau of the magnetic field profile determines the final beam radius. To obtain such magnetic field, the solenoid must be placed very near to the cathode surface, since the magnetic field strength decreases rapidly with increasing distance to the end of the coil. In the proximity to the cathode chamber, the thickness of the solenoid is determined by the thickness of the groove machined in the electron gun chamber, as it can be seen in the figure 5.5. To obtain the magnetic field given by e2v Technologies with such a thickness, a current density in the solenoid of 6.7 $\mathrm{A/mm^2}$ is required. However, currents densities more than 3-4 $\mathrm{A/mm^2}$ need an adequate cooling of the solenoid to avoid excessive resistive heating. This was not properly considered during the design of the post-acceleration section of the electron gun by the engineers of e2v Technologies, and resulted in a lack of room in the groove, which needs to house both the magnet and the cooling system. To obtain the required high current density inside the solenoid while having adequate cooling, we decided to use a copper tube as electrical conductor, where a water flow through the tube

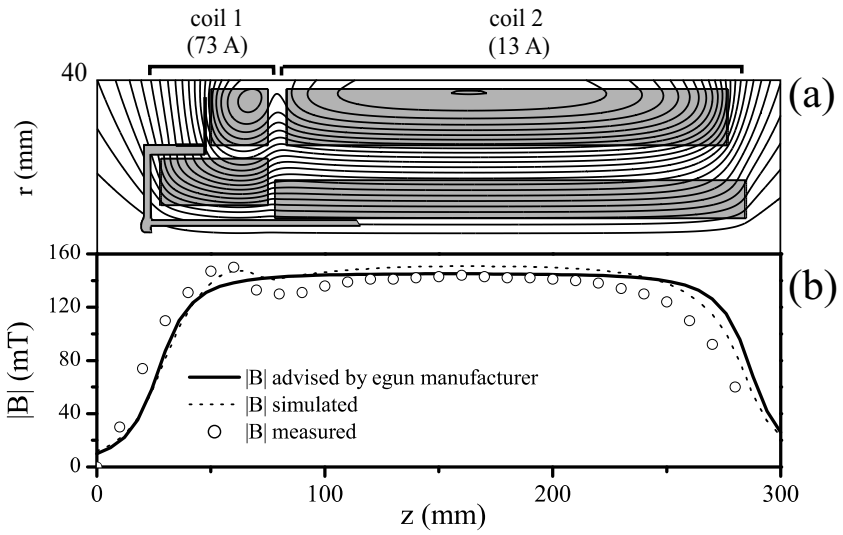

Figure 5.7: (a) Longitudinal section (cylindrical symmetry is assumed) of the solenoid. The coordinate z=0 corresponds to the position of the cathode. The gaps between different sections of the coil are reserved for the cooling pipes. Also, the equipotential lines of the magnetic field created by currents of I_1=73 A and I_2=13 A are shown. (b) Magnetic field strength along the axis of the waveguide with the data advised by the manufacturer, simulated numerically (for I_1=73 A and I_2=13 A) and measured in the actual magnets (for I_1=75 A and I_2=13 A).

provides the internal cooling of the solenoid.

Figure 5.7 (a) shows the longitudinal cross-section of the final design of the solenoid, where cylindrical symmetry is assumed. The whole solenoid is divided in two parts. The part closer to the electron gun, labelled as coil 1 in figure 5.7 (a), is built using a copper tube for simultaneous electric current and water flow. The tube used in coil 1 has an outer diameter of 2.05 mm, an inner diameter of 0.90 mm and a total length of 11 m. The length of this part of the solenoid is 30 mm. The rest of the solenoid, labelled as coil 2 in figure 5.7 (a), has no limitations on the thickness, so, in order to have less severe cooling demands, we decided to reduce the current density by increasing the thickness of the solenoid. Coil 2 is simply made from a wire of 2 mm diameter wound around the waveguide. In this case, to preserve a moderate temperature increase, it is sufficient to include a single layer containing a cooling tube at about 1/3 of the thickness of the wire package of the coil.

In order to calculate the necessary current density in the solenoid and to compare the expected values of such solenoid with the specifications of e2v Technologies, we calculated the magnetic field profile for various currents in the coils. For that, we used BStat from Field Precission [97]. Because of technical limitations we could not completely reproduce the field profile specified by e2v Technologies, which is based on an unrealistically high current density within the solenoid. Our best match is shown by the dotted line in 5.7 (b), which shows the

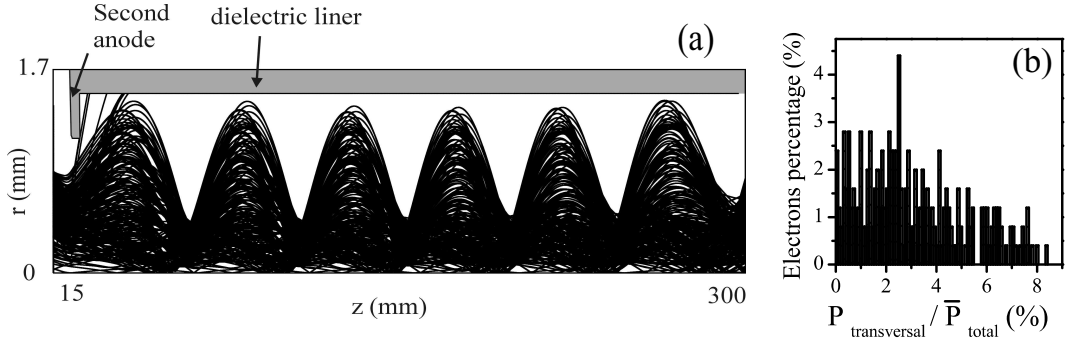

Figure 5.8: (a) Longitudinal cross-section of the lined waveguide (assuming cylindrical symmetry) with the simulation of the trajectories of the electrons. We have used a total acceleration voltage of 75 kV, a grid voltage of 169 V, a focus voltage of -750 V, all of them with respect to the cathode voltage. The first magnet has a current of 70 A and the second magnet has a current of 13 A. (b) Histogram showing the transversal momentum fraction of the total momentum of the electrons at one of the planes of the trajectory, z=60 cm.

magnetic field along the axis for the geometry given in figure 5.7 (a), for a current of 73 A in the first coil and a current of 13 A in the second coil. One can see that the profile of the field at the entrance of the waveguide matches rather well with the value provided by e2v Technologies. Since this is the most important part of the field in forming a good quality electron beam, we decided to use this geometry. Figure 5.7 (a) also shows the magnetic field lines resulting from the same calculation, where one can see that the field decreases rapidly at the edges of the solenoid. Finally, the circles of figure 5.7 (b) show the measured values of the on-axis magnetic field for a current of 75 A through the first magnet and 13 A through the second magnet. One sees that there is a slight difference between the measurement and the calculation of the uphill slope. Also, the division of the solenoid in two parts creates a small bump at the beginning of the plateau but it is expected that these differences do not cause a major problem in the injection. For the dimensions of the wires given above and for a water flow of 9 $\mathrm{cm}^3/\mathrm{min}$, the coil 1 reaches a maximum temperature of 116 $^{\circ}$C for a current of 75 A, and the coil 2 reaches a maximum temperature of 42 $^{\circ}$C for a current of 13 A. With these values, the cooling provided is adequate.

To study the guiding of the electron beam inside the waveguide, we have calculated the trajectories of the electrons with the magnetic field produced by the solenoid of figure 5.7 (a). For this, we used Trak 6.0 from *Field Precision* with the solenoid currents of 73 A and 13 A. Figure 5.8 (a) shows the trajectories of the electrons in a longitudinal cross-section of the lined waveguide. In this figure, the cathode is at position z=0 and the lined waveguide extends up to z=275 cm. This figure shows that almost all of the electrons are transported through the lined section. Only a negligible amount of electrons are lost directly after the aperture in the second anode, most likely due to too strong focussing. One can see that the average radius of

the beam is near 1 mm and, therefore, it is close to the designed value. However, the electron beam seems to have an oscillating radius along the waveguide. The electrons perform helical trajectories along the waveguide but a problem would only arise if a larger percentage of the electrons would develop an appreciable transversal velocity component. Note that the scale of the axes in figure 5.8 (a) are very different, which can give the perception of an excessive transversal velocities of the electrons. The distribution of momenta of the electrons for one of the positions along the waveguide (we choose here z=60 mm) is given in figure 5.8 (b). This shows that up to 8 % of the total energy is to be associated with a transverse momentum of the electrons although this applies only for less than 1 % of the total number of electrons. The mean transverse momentum of the electrons is 3 % of the total momentum.

From the results given in the present section we conclude that the transport of the electrons should be successful with the described solenoid. Nevertheless, one needs to be aware that a small fraction (1 %) of the electrons can have up to 8% of their energy contained in the transversal components of their velocity, which induces an energy spread in the electron beam.

5.3 Outcoupling of the radiation

Chapter 3 described the CFEL designed as an oscillator for the quartz-lined CFEL, and as an amplifier for the alumina-lined CFEL. In this section, we describe the method used to outcouple the amplified radiation in both configurations of CFELs.

5.3.1 Oscillator CFEL

The resonator is formed by the lined waveguide, which has a total length of 25 cm, and by microwave mirrors at each end. The lined waveguide section is terminated at the upstream side by a copper ring with an aperture of 2.25 mm diameter to allow for the entrance of the electron beam into the lined waveguide. The size of the aperture is such that it is below cut-off for frequencies below 78 GHz. In the current CFEL design, we expect to amplify frequencies of about 50 GHz and, therefore, this copper ring functions as the upstream mirror with almost 100 % reflectivity, despite the presence of the aperture. The downstream mirror is thus to be designed to couple out the desired amount of radiation, however, this cannot be achieved by a commercially available component due to the following. The CFEL uses a circular lined waveguide, which is non-standard in microwave circuitry. Also, both the microwaves and the electron beam co-propagate in the waveguide and the coupler would have to separate the electrons from the radiation. Ideally, the downstream mirror has to fulfil several functions. First, it needs to reflect an adjustable fraction of the radiation. Second, it needs to separate the electron beam from the

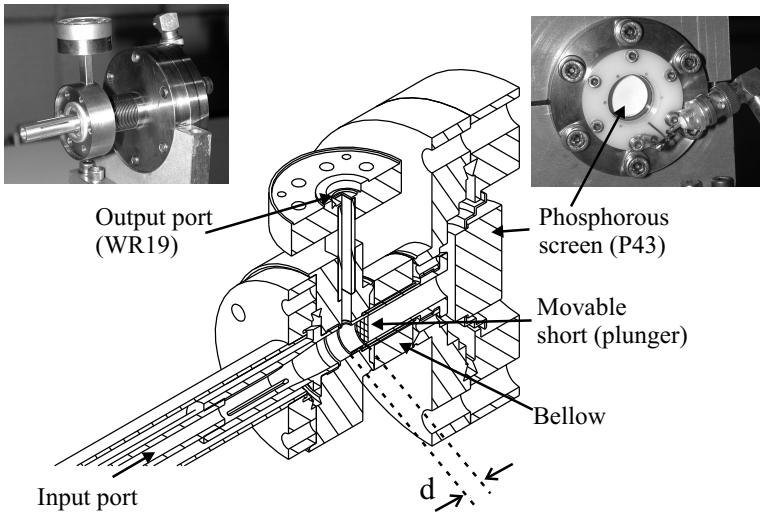

Figure 5.9: Longitudinal section of the out-coupling mirror. Also, a photograph of the outcoupler and of a detail of the phosphorous screen are shown.

radiation wave. Last, it needs to provide a mode conversion from the cylindrical symmetry, in the lined waveguide, to the rectangular symmetry, as the standard. In the following, we present an according design which fulfils these requirements and, in addition, incorporates a diagnostic tool for the cross section of the electron beam.

Figure 5.9 shows a schematic drawing and photographs of the realized downstream outcoupling mirror. The circular waveguide of the CFEL (labelled in figure 5.9 as input port) is matched to the output port, to which a standard rectangular waveguide can be connected. Both the radiation and electron beam enter the outcoupler through the input port. An adjustable plunger, which is downstream with respect to the circular waveguide, acts as a movable microwave short. The plunger is a hollow tube, the front of which is terminated by a mesh of sub-wavelength holes (squares of 290 μm side). This mesh allows a large fraction of the electron beam to pass straight on to a phosphorous screen at the end of the vacuum tube. The phosphorous screen allows for the measurement of both the total current and the cross-sectional distribution of the electrons hitting the screen. The phosphorous screen also acts as vacuum seal. A second vacuum window is placed in the rectangular output port and consist of a 2 mm thick high-density polyethylene plate.

The plunger acts as a movable short that ideally should provide full reflection of the incident waves. The mesh of the plunger is sufficiently fine to act as a perfect reflector but some radiation may leak through the gap between the walls of the plunger and the waveguide. The gap is needed for allowing the plunger to be moved. However, we reduced the leakage through the gap by varying abruptly the width of the gap along the plunger thereby inducing an impedance mismatch large enough to reflect most of the power that entered the gap. The technical

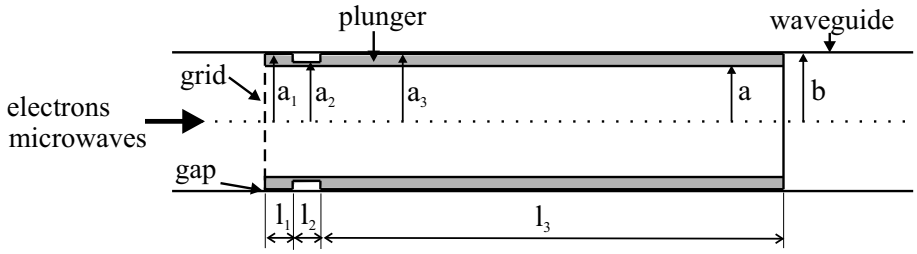

Figure 5.10: Longitudinal section of the plunger that acts as movable short for the microwave radiation.

realization of this approach is shown in figure 5.10, where the longitudinal cross-section of the cylindrical waveguide (radius $b = 3.75$ mm) is displayed with the plunger inside. It can be seen that the plunger is formed by three coaxial tubes of the same inner radius (a =3 mm) and different outer radii ($a_1 = 3.65$ mm, $a_2 = 3.2$ mm and $a_3 = 3.65$ mm). The tubes have lengths of $l_1 = l_2 = 1.5$ mm and $l_3 = 25$ mm. The reflection coefficient of the microwave radiation at the grid surface, Γ, was calculated from the impedances of the waveguides at both sides of the surface, which are the impedance Z_g of the circular waveguide and the impedance Z_p of a coaxial waveguide, which is made of three sections of coaxial waveguides. The reflection coefficient is [101]

$$\Gamma = \frac{Z_p - Z_g}{Z_p + Z_g}. \tag{5.2}$$

Also, the analytical expressions of the characteristic impedance of a circular waveguide and of a coaxial waveguide are well-known [101]. Our calculations gave a reflection bigger than 99.9 % for frequencies between 40-60 GHz, indicating that the plunger is, to good approximation, equivalent to a perfect short.

The reflectivity of the outcoupler can be controlled by adjusting the position of the plunger. This can be explained as follows. For a specific distance between the plunger mesh and the output port (labelled as d in figure 5.9) and for a specific frequency, the incident and the reflected wave interfere constructively at the position of the rectangular output port. Looking at the electric field polarization, the direction of the electric field in the TM_{01} mode of the circular waveguide amplified in the CFEL is the same as the direction of the electric field in the TE_{10} mode (fundamental mode) of the rectangular port. As a result, the TM_{01} mode in the circular waveguide is strongly coupled to the TE_{10} mode in the rectangular waveguide and thus most of the radiation is coupled into the rectangular guide with almost no radiation reflected back into the gain section of the CFEL. By changing the distance d the interference pattern changes and thus the coupling to the stationary output port. In this way a variable reflectivity is obtained for the outcoupler. Note that the position of the plunger that is required to obtain a certain reflectivity is strongly dependent on the frequency. Qualitatively it can be expected that the

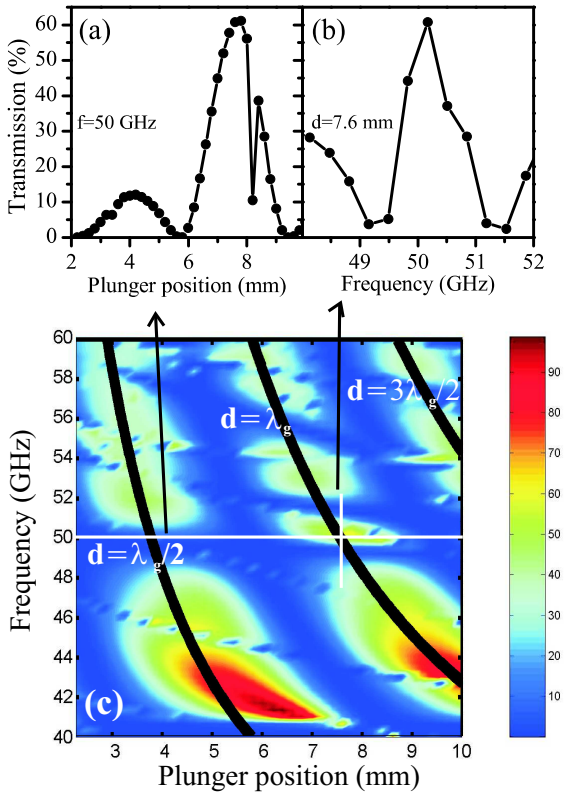

Figure 5.11: Percentage of transmitted radiation from the TM_{01} mode (input port) to the TE_{10} mode (output port) (a) as a function of the plunger position for a frequency of 50 GHz, (b) as a function of the frequency for a fixed position of the plunger of d=7.6 mm, and (c) as a function of the frequency and the plunger position. The superimposed lines in (c) represent distances corresponding to n times $\lambda_g/2$ for each frequency, with $n = 1, 2, 3$. Lines in (a) and (b) are for guidance.

maximum coupling occurs when an anti-node is formed at the position of the output port, *i.e.,* when $d = \lambda_g/2$, λ_g is the wavelength in the circular waveguide. Similarly, shifting the plunger, so that a node is formed at the output port, would minimize the output coupling. To be able to set the output coupling over this full range, we have chosen a desing where d can sweep across an interval from 0 to 10 mm, ensuring a displacement larger than one wavelength for all frequencies in the operational band, *i.e.,* between 40 GHz and 60 GHz, corresponding to λ_g between 7.5 mm and 5 mm.

As with any type of laser oscillator, the transmission of the outcoupler has to be set to its optimum value for achieving the maximum laser output power, a procedure which requires to calculate the single-pass gain of the amplifier. In chapter 4, we have seen that the CFEL can provide a relative large gain in a single pass. On the other hand, to avoid excessive heat dissipation in the liner of the waveguide, the intra-cavity power should be as low as possible. Hence, we choose a relative small feedback in the resonator rather than a high feedback. To estimate the percentage of radiation that is outcoupled to the rectangular port as a function of the position

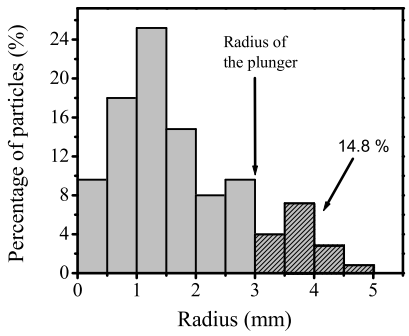

Figure 5.12: Percentage of electrons hitting the phosphorous screen as a function of the distance to the center of the screen.

of the plunger, we have calculated the propagation of the microwave electromagnetic field for a fixed frequency of 50 GHz using a commercially available code. Figure 5.11 (a) shows the percentage of transmitted radiation from the TM_{01} mode (input port) to the TE_{10} mode (output port) as a function of the distance d for 50 GHz. It can be seen that the largest transmission of the radiation is about 60 % and occurs for positions of the plunger between 7 mm and 8 mm. In order to determine the reflectivity for the entire expected tuning we have repeated the same simulations as a function of the frequency with a fixed plunger position (d=7.6 mm) and the result is shown in figure 5.11 (b). One can see that the mirror has a varying reflectivity with varying frequency for a fixed position of the plunger, which means that the quality of the resonator depends strongly on the frequency of the wave. A full overview on the expected transmission is shown in figure 5.11 (c) as a function of both the frequency and the plunger position. As expected already from the qualitative node picture given above, the transmission is maximum when d equals an integer number of half guide wavelengths, as indicated by the solid lines.

So far, we have only looked at the microwave properties of the outcoupler. However, the outcoupler also separates the wave from the electrons and allows for the measurement of some electron beam parameters. As was described above, the electron beam travels from the input port straight towards the phosphorous screen at the end of the waveguide. The screen is of P43 phosphorous material (Gadoliniumoxysulphide with Terbium doping), which is standard for electron imaging. The phosphorous particles have a diameter of typically 2 μm and are fixated in a silicate matrix. On top of it, at the vacuum side, there is an aluminium layer of about 65 nm. An external resistor connects this layer to ground and is used to measure the electron beam current that reaches the screen.

The comparison of the current measured at the phosphorous screen with the total current emitted from the cathode gives information about the quality of the electron beam transport through the waveguide. However, not all the electrons can reach the phosphorous screen partly

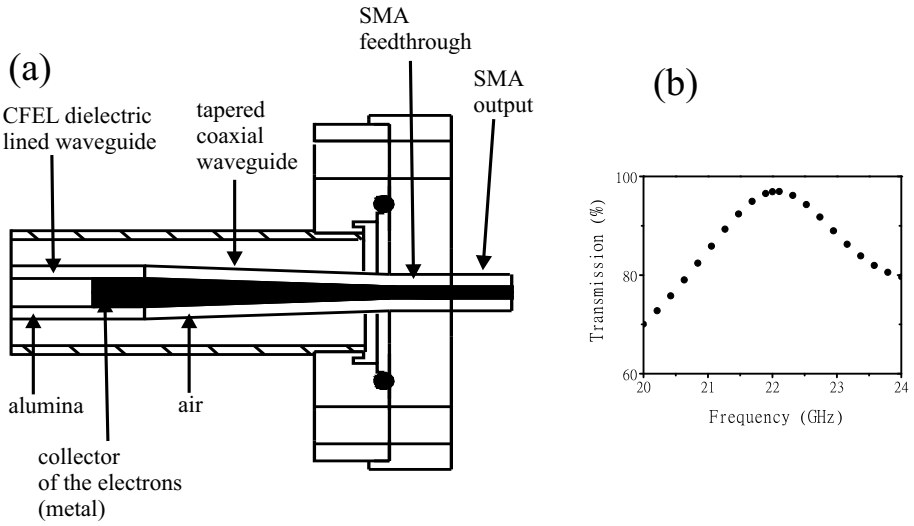

Figure 5.13: (a) Longitudinal section of the coaxial outcoupler of the radiation. (b)Percentage of outcoupled power as a function of the frequency.

due to the divergence of the beam after leaving the solenoid, and partly due to electrons lost at the mesh of the plunger. To estimate the amount of electrons that are lost due to the divergence of the electron beam, we have calculated the trajectory of the electrons, using ETrak from *Field Precision* [97], for an accelerating voltage of 75 kV and a magnetic field on axis of 0.15 T. For this, we have assumed that the waveguide has an infinite radius so that the electrons do not hit its walls. In this way, we tracked the radial positions in a transversal plane at the axial position of the phosphorous screen. Figure 5.12 shows the distribution of radii of the electrons at this plane. It can be seen that almost 15 % of the electrons hit the screen at a radius larger than 3 mm, *i.e.*, for the actual radius of the waveguide of 3 mm, they would have been intercepted by the walls. To estimate the amount of electrons lost in the mesh of the plunger, we can use geometrical arguments. The mesh possesses a square-patterned structure with a wire thickness of 28 μm, and a distance of 290 μm in between. This results in approximately 17 % of the total electron beam being intercepted at the mesh. Therefore, due to the divergence of the electron beam and to the mesh interception, a total of 32 % of the current is expected to be lost before reaching the phosphorous screen, which should be taken into account when analyzing the total electron current measured on the screen.

The phosphorous screen forms the vacuum window so it acts as an axial view-port of the waveguide as it can be seen in the photograph of figure 5.9. As a result of the impact of the electrons, the phosphorous screen emits visible light of 545 nm, which can be easily detected with a CCD camera. Therefore, we use the phosphorous screen as a visual port to measure the electron beam profile and position with respect to the axis.

5.3.2 Single-pass amplifier

One of the difficulties to outcouple the radiation to a standard microwave circuit lies in the circular geometry of the CFEL waveguide, which is different from the rectangular waveguide that is commonly used there. In section 5.3.1, we have proposed a perpendicular connection between the circular and the rectangular waveguides that allows to couple the circular TM_{01} mode to the rectangular TE_{10} mode. It was described that such a configuration involves a partial reflection of the wave and results in a feedback of radiation into the CFEL waveguide. There also exist circular-to-rectangular adaptors in standard microwave waveguides [102] but they are designed to couple the TE_{11} mode from the circular waveguide to the TE_{10} in the rectangular waveguide, while the CFEL amplifies the TM_{01} mode of a circular waveguide. Here, we propose two new methods for the outcoupling of the radiation when the CFEL operates as a single-pass amplifier: one that outcouples the radiation to a coaxial waveguide and one that outcouples the radiation to free space.

The coupling between the TM_{01} mode of the CFEL and the TEM mode propagating in a coaxial waveguide is straightforward since the electric field has a radial component in both of them. The lined circular waveguide can be transformed into a coaxial waveguide by inserting in the hole of the tube a metal rod that would act as coaxial inner conductor, as shown in figure 5.13 (a). The mode TM_{01} that travels in the lined waveguide can couple to the fundamental TEM mode of the coaxial waveguide. Since most of the electromagnetic power is travelling through the dielectric material of the waveguide and only an evanescent part tails off from the liner, the inner conductor is expected to cause only a minor reflection of the wave. The advantage of the coaxial geometry is that a standard high-frequency coaxial feedthrough, *e.g.*, SMA, can be used for the outcoupling, so that the CFEL can be connected to an external microwave circuit. To adapt the size of the lined waveguide to the size of the SMA connector, a tapering of the coaxial structure is needed. One can see in figure 5.13 (a) the longitudinal cross-section of the coaxial taper. To determine the transmission properties of this section in the entire tuning, we have calculated the wave propagation for various different frequencies of the field. Figure 5.13 (b) shows the transmission as a function of the frequency and it can be seen that at around 22 GHz there is almost 100 % transmission. Thus, such structure behaves as a good outcoupler for the CFEL amplifier. The inner conductor is used also as a collector of the electron beam.

The second configuration that we propose here couples the radiation to free space by means of a microwave transparent window, *e.g.,* a polyethylene window, and dumps the electrons on the walls of the waveguide. To avoid damaging of the liner, it is necessary to stop the dielectric lining of the waveguide before the electron beam hits it. For the alumina lined waveguide, the inner diameter of the waveguide that contains the liner is 7 mm. A non-lined waveguide of the same dimension is below cut-off for frequencies around 22 GHz, and would reflect the wave

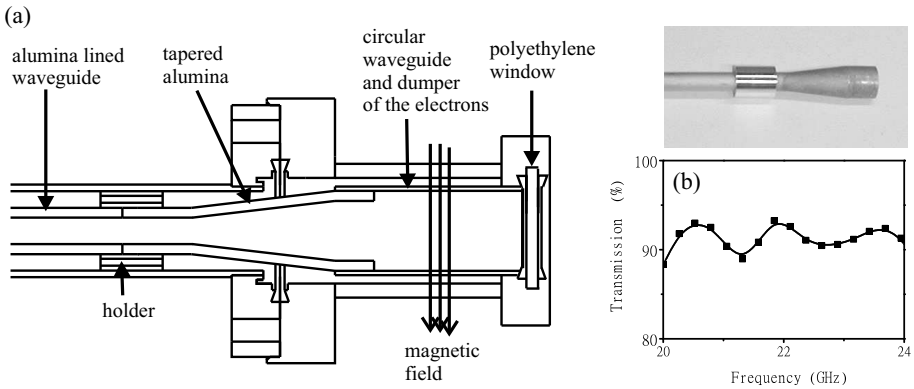

Figure 5.14: (a) Longitudinal section of the outcoupler to free space. (b) Percentage of outcoupled power as a function of frequency.

back to the lined waveguide. We use instead a 12 mm diameter waveguide for the non-lined section, which shows a cutoff frequency for the TM_{01} mode of about 19 GHz. To provide a smooth transition from the alumina-lined waveguide to the 12 mm diameter waveguide, a tapered section, also lined with alumina, connects both parts as is shown in figure 5.14 (a). Again, to determine the propagation properties, we calculated the transmission of the tapered section as a function of the frequency. The result is shown in figure 5.14 (b). It can be seen that a transmission of at least 90 % is expected for all frequencies within the tuning range. To avoid the contamination of vacuum when the electrons hit the walls of the waveguide, OFHC copper should be used for the non-lined waveguide. To avoid that the electrons hit the polyethylene vacuum window at the end of the waveguide, which could end up in breaking of the window and exposition of the hot cathode to air, a 10 cm long waveguide should be used, which is long enough to dump all the electrons at the wall of the waveguide. In addition, a constant magnetic field perpendicular to the waveguide can be used to direct the electrons to the waveguide wall.

5.4 Interface with the experimental setup

The CFEL experimental setup described in this chapter is controlled via a hardware and software interface, which operates on actuators placed in the setup and can read from various diagnostic devices. A Peripheral Component Interconnect (PCI) eXtensions for Instrumentation or PXI [103] is chosen as automation platform for the CFEL. The PXI is a PC-based platform for measurement and automation systems that combines standard PC technology with integrated timing and triggering capabilities. The PXI offers faster data transfer times than other type of systems, such as GPIB-controlled instruments. Other advantages of the PXI include compactness, modularity and compatibility. The PXI system was acquired from National Instruments (NI) [104] and is comprised of three basic components: the chassis, which contains the sys-

tem bus and the power supply; a NI-8176 embedded controller with several ports; and three peripheral modules (NI-6070E, NI-6602 and NI-6533). The PXI works basically as the communication link between the software and the experiment. These modules work together to control, set and read back values for several critical components, such as the 100 kV power supply, the trigger signals and the pump group. Interlocks and an emergency stop button are used to provide safe working conditions. Besides the peripherical modules of the PXI, the RS232 ports at the embedded controller are used to control the vacuum pump system, the solenoids power supplies and a home build embedded controller for the floating power supplies. The PXI platform is controlled by LabView, from NI [104].

6

Experimental results and discussion

Abstract

In this chapter, we present the experimental demonstration of microwave emission from the low-current CFEL described in the previous chapters. We show that the alumina-lined CFEL was brought into oscillation for accelerating voltages ranging from 75 to 82 kV and electron currents from 150 mA to 400 mA. We show that the radiation was tunable around 24.5 GHz with an output power of a few watts. This shows that the main design approach was successful, namely, to realize a working FEL oscillator with a rather small pump current (200 mA), with a moderate voltage (80 kV) and with a rather short interaction length of 25 cm. We show here that the results are in agreement with the theoretical predictions.

The previous chapters have presented the theoretical background and the experimental setup. With this setup we performed measurements with the goal to detect Čerenkov laser emission. In this chapter, we present the results of these measurements. In section 6.1 we describe the characterization of the emission from the electron gun and we compare it with the expected performance. Next, in section 6.2, we present the characterization of the electron beam transport through the waveguide and, finally, in section 6.3, we present the results obtained from the radiation measurements.

6.1 Electron gun characterization

In chapter 4 and 5 we used for the design of the CFEL the electron gun specifications provided by the manufacturer of the gun, e2v Technologies. In order to compare the results expected from the design of the CFEL with the experimental results described in the present chapter, the properties of the electron gun have to be characterized experimentally and compared to the specifications provided by e2v Technologies. In the following, we present the results from the measurements on the emission properties of the electron gun.

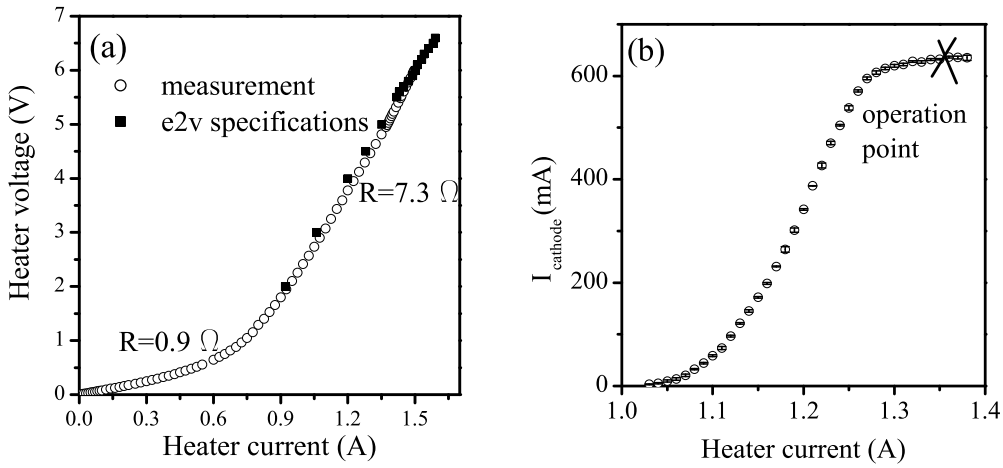

Figure 6.1: (a) Measured Voltage-Current characteristic of the heater and specifications given by e2v Technologies, the manufacturer of the electron gun. (b) Measured emitted current by the cathode as a function of the heater current. Also shown is the point selected for the operation of the electron gun.

To activate the electron gun, the electric current flowing through the heater was slowly increased until a value of 1600 mA, as specified by the manufacturer. Thereafter, we kept the current constant for one hour and returned it to zero. Figure 6.1 (a) shows the voltage drop in the heater as a function of the heater current during the activation. Together with our own measurements, figure 6.1 (a) also shows the theoretical values provided by e2v Technologies. In summary, it is found that both sets of data are in good agreement with each other, which indicates that a successful activation of the cathode was achieved with appropriate heating conditions.

As was explained in chapter 5, for a maximum spatial quality and maximum overall strength of the electron beam, the cathode needs to be operated between the temperature-limited and the space-charge limited regime. In the former, one expects an emission current proportional to the temperature, and in the latter, one expects a saturation of the current with increasing temperature due to the space-charge in front of the cathode. In order to find this point of operation, we have measured the current emitted by the cathode as a function of the current flowing through the heater. The result is shown in figure 6.1 (b). The figure shows that the cathode starts to emit electrons at a heater current of approximately 1 A. From approximately 1.1 A to 1.3 A flowing through the heater, the current emitted from the cathode increases linearly with the heater current. From this linearity, it can be concluded that in this regime the cathode operates in the temperature-limited regime. Beyond approximately 1.3 A through the heater, the emission from the cathode saturates. This saturation indicates that here the cathode has entered the space-charge regime. Based on these results, we have selected a heater current between the two

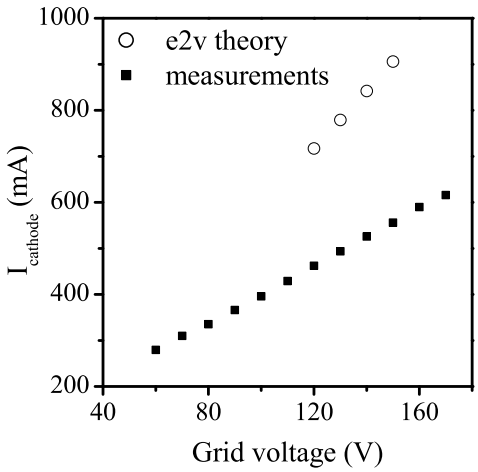

Figure 6.2: Emitted current by the cathode as a function of the grid voltage as specified by e2v Technologies (circle) and measured by us (square).

regimes for the following experiments, specifically, the heater current in the highlighted point in figure 6.1 (b) was chosen. These operation conditions form the best compromise between a long cathode lifetime, a homogeneous current density and a high current. One can notice from the graph that, under these conditions, a maximum current of about 600 mA is obtained from the electron gun. Note that this is somewhat below the value of 800 mA specified by e2v Technologies and on which we based the design of the laser in chapter 4. Therefore, it is expected that the measured radiation power will be less than the one predicted in the calculations of chapter 4, and that increasing the drive current with re-designing the gun would form an essential step of improvement for a next experiment. A further discussion will be given in the section on the radiation measurements.

The electron beam current measurements presented in figure 6.1 (b) are done with a first anode voltage of 9.45 kV, as specified by e2v Technologies. For that value, the modelling of the electron beam trajectory presented in chapter 5 showed that a 4% of the current is expected to be lost in the walls of the first anode. For an experimental check of the latter, we have measured the current intercepted by the first anode and obtained a value of about (0.6 ± 0.08) % of the total current, which is only a few milliamps. These measurements actually indicate a much smaller loss of current in the first anode than the loss expected on the basis of the modelling. Although the reason for this discrepancy is unknown, it can be concluded that electron beam loss at the first anode can be considered a rather small contribution.

As described earlier (chapter 5), the design of the laser was chosen such that, for a fixed cathode temperature and a fixed first anode voltage, the emitted current by the cathode, and thus the gain of the CFEL, can be varied by changing the grid voltage. For an experimental check

of this, the emitted current as a function of the grid voltage predicted by e2v Technologies was measured and both, theoretical prediction and results, are shown in figure 6.2. The theoretical prediction shows a variation of the current with the grid voltage from 600 mA to 1000 mA, with a rate of about 6 mA/V. The experimental results display a variation of the current with the grid voltage from 300 mA to almost 600 mA, with a rate of about 2 mA/V. It can be seen that the measured current extracted from the cathode for a given grid voltage is again smaller than specified by the manufacturer and that the rate theoretically predicted by e2v Technologies is higher than the experimental measurements. As can be inferred from the working principle of the gun given in chapter 5, the observed difference between the design values and the measured ones might be due to a deviation during the fabrication of the gun, *e.g.,* that the size or position of the grid is slightly different from the design. Low emission currents might also occur if the cathode did not attain a sufficiently high temperature during the activation process to fully remove all undesired chemical species from the cathode surface.

The measurements of the emitted current by the cathode indicated some limitations on the length of the electron beam pulses, and thus on the length of the radiation pulses from the current design of the CFEL. We observed that the impact of the electron beam when it is eventually dumped on the walls of the vacuum chamber increases the background pressure since wall material and adsorbed gasses are released from the surfaces where the electron beam impacts. Particularly, as explained before, care has to be taken that the pressure does not rise above 10^{-7} mbar, as this is harmful for the cathode. Based on measurements of the pressure rise as a function of the strength and temporal duration of the electron beam, we have decided to limit in the following experiments the operation of the gun to pulses with a duration of a few tens of microseconds, and the current to a range between 300 mA and 500 mA. Alternatively, when using single pulses, we found an acceptably low pressure with pulses of up to 100 microseconds duration, or, at high repetition rates (up to 1 kHz), a maximum pulse duration of 10 microseconds, when the pulse train is up to several minutes long.

In summary, the experimental investigation has shown that the maximum current delivered by the cathode is somewhat lower than was assumed in the design for the theoretical modelling of the laser. As an additional limitation, we found a lower maximum current and lower rate of current change with grid voltage. However, we also found that a pulsed operation provides a safe operation in terms of acceptable background pressure, when pulse durations of a few tens of microseconds is used and when the maximum current is limited to 500 mA.

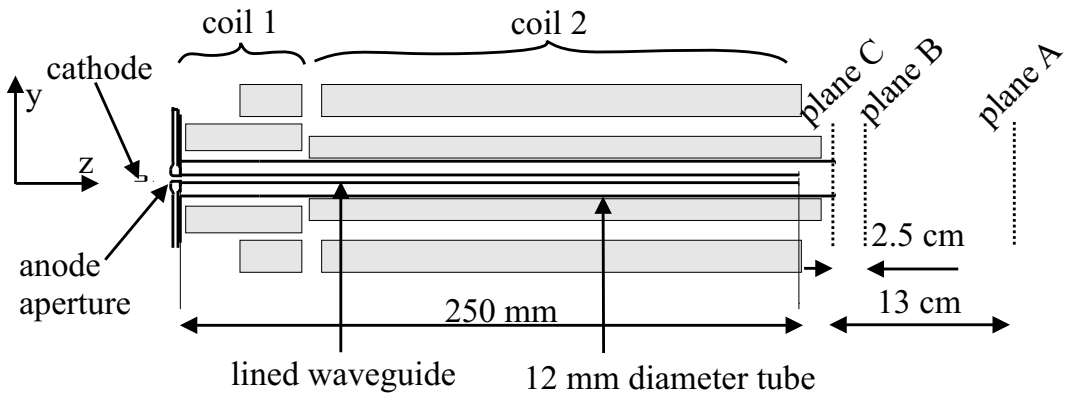

Figure 6.3: Longitudinal cross-section of the experimental setup for characterization of the electron beam transport.

6.2 Electron beam transport characterization

As was described in chapter 2, to achieve a sufficiently high gain of the electromagnetic field for laser emission, it is required to realize a proper transport of the electron beam through the waveguide. For instance, if the electron beam diameter became too small compared to the optimum value found in the design calculations (2 mm), the overlap between the wave and the electron beam would become smaller and the gain would decrease. Also, if the diameter of the electron beam became too large, the electrons would hit the dielectric liner, leading to a loss of part of the current, which again would decrease the gain. Furthermore, one would expect some deposition of charge in the dielectric material. This might induce unwanted effects, such as an increased energy spread in the electron beam and an uncontrolled focusing or defocusing of the electron beam, both reducing the gain as well. Finally, a local charging of the liner might also perturb the propagation of the wave due to a locally modified dielectric constant of the liner material. As was shown in chapter 2, this would lead to local variations of the phase velocity which reduces the gain again. In summary, a sufficiently high quality of the electron beam transport is of absolutely central importance for establishing a sufficiently high gain and thus realizing laser oscillation. In the present section, we describe the measurements performed to characterize the quality of the electron beam in our setup.

6.2.1 Experimental setup

To illustrate how these measurements were done, figure 6.3 shows a longitudinal cross-sectional view of the path of the electron beam from the cathode through the lined waveguide. The figure also shows the two solenoids (coil 1 and coil 2) used for the transport of the electron beam. The electron beam injected from the gun passes through the 2.25 mm-diameter aperture of the second anode at the entrance of the lined waveguide. Next, the electron beam travels all the

way through the lined waveguide, which possesses an inner diameter of 3 mm or 4 mm for the quartz and alumina lining, respectively. In both cases, the lined waveguide is mounted inside a 25 cm long steel tube with an inner diameter of 12 mm, coaxially aligned with the solenoid. This tube extends the vacuum volume in the laser such that it reaches from the cathode surface to beyond the end of the waveguide. To determine the fraction of electrons that might hit the walls of the lined waveguide, the axial position and transverse dimension of the electron beam were characterized both with the lined waveguides in place and also with the lined waveguides removed for comparison. In the latter case the electrons simply travel through the vacuum tube with 12 mm diameter. This diameter is large compared to the specified diameter of the electron beam (2 mm). After having passed through the 12 mm diameter tube (with or without the lined waveguides installed), the electron beam is analysed with various types of detectors. Figure 6.3 shows three planes, labelled A, B and C, where the detectors are placed. A scanning wire and a Faraday collector were used in plane A, a scintillating screen was used in plane B and a second Faraday collector was used in plane C. Because each detector intercepts the beam fully, or at least a part of it (such as the wire detector), the beam is analysed only with one of the detectors at a time.

The first set of experiments was done with the lined waveguide removed. To measure the total current that reaches the end of the vacuum tube, we used a Faraday charge collector positioned at plane A in figure 6.3. The collector consists of an OFHC copper disk of 20 mm diameter centred on the axis. The charge deposited by the electron beam is guided as a current to ground potential via a calibrated load resistor (1.9 Ω). The voltage across the resistor, which is recorded as a function of time with an oscilloscope, can thus be transformed with Ohm's law into the electron current received across the total collector surface. To characterize the spatial distribution of electrons in the beam in that plane, we installed in front of the Faraday collector a metallic wire made of OFHC copper. The 500 micrometer thick wire can be translated in the vertical direction from a position of y=+10.34 mm above the axis of the vacuum tube to a position of y=-10.34 mm below the tube axis. The current received by the wire is also measured via the voltage drop in a load resistor connected to the wire. To map the electron distribution in the beam, we record this current as a function of the wire position. We note that this mapping, actually, yields only one-dimensional information on the spatial distribution of electrons along the y-coordinate, because all charge received along the wire direction (x-direction) becomes integrated.

To obtain a more complete characterization, still without the lined waveguide, we performed a second set of measurements. This time the electron beam was characterized in plane B, where the divergence of the magnetic field, and thus also of the electron beam, is expected to be much smaller than in plane A. We placed a scintillating screen in plane B as indicated in figure 6.3. As

a suitable screen we selected a YAG(Ce) (Yttrium Aluminum Garnet doped with Cerium) plate. The fluorescence from the screen, which has its spectral maximum around 550 nm, is recorded with a Si-CCD camera. The location of the peak of fluorescence in the recorded distribution indicates the location of the centre of the electron beam at the end of the tube, which can be used to investigate the degree of parallelism between the magnetically guided electron beam and the intended on-axis propagation. For this, we have measured the dependence of the coordinates of the centre of the distribution of fluorescence upon a variation of the current through the coils 1 and 2 in figure 6.3.

In order to find out how big the loss of current would be in the liner of the waveguide during laser experiments, the latter set of measurements was done with the lined waveguide installed. In this case, we used the Faraday collector located in plane C as indicated in figure 6.3, *i.e.,* directly at the end of the waveguide. The collector is made of a disk of OFHC copper with a diameter of 5.5 mm and the received current was measured with the same method as described before.

6.2.2 Electron beam transport characterization results

The results of the first set of measurements performed without the lined waveguide and with the detectors at plane A showed that the received current is approximately 73 % of the current emitted by the cathode. This corresponds to a fraction of 27 % of the electrons which are lost somewhere on the way from emission at the cathode to reception at the Faraday collector. The result of the measurements with the scanning wire is shown in figure 6.4, which displays the current collected by the wire as a function of the vertical distance to the z-axis. The curve added to the figure is for guidance. It can be seen that the measured current possesses a maximum at about -2.5 mm away from the z-axis (indicated by the vertical dashed line), and that it decreases gradually towards both sides. Around this maximum, the current distribution appears rather symmetric. The figure also shows that some current is still detected at the edges of the scan. The full width (diameter) at half maximum (FWHM) of the beam is seen to be approximately 10 mm.

To explain why not all of the emitted electrons reach the Faraday collector at plane A, several causes come into consideration. A certain fraction is known to be lost already at the first anode (see section 6.1). We have shown there, however, that this fraction is rather small, only about 0.6% of the emitted current. A second fraction of the electron beam might be lost by hitting the second anode. With the current setup we were not able to measure this fraction so that here, one has to rely on an estimate, after having excluded other possible causes of loss. The electron beam is expected to have a diameter of approximately 2 mm, which is much smaller than the diameter of the vacuum tube (12 mm) through which the electron beam travels. Therefore,

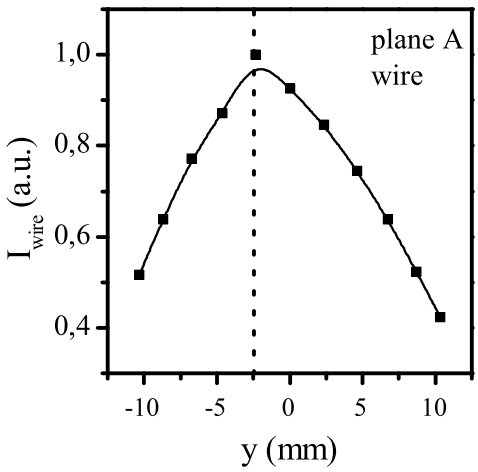

Figure 6.4: Current collected by the wire (normalized to its maximum value) as a function of the vertical positions of the wire. The measurement is done without the lined waveguide installed. The lines are shown for guidance.

we expect that no significant current would be lost at the walls of the 12 mm diameter tube. However, even in this situation, a third fraction of the electron beam might be lost at the walls of this tube behind the end of the solenoid due to the following. One can see in figure 6.3 that there is some distance (about 13 cm) from the end of the solenoid to the plane of the collector and wire (plane A). Beyond the end of the solenoid, the magnetic field lines diverge rapidly, and thus the field strength decreases also rapidly. As a result, the transverse beam focusing force becomes less than the Coulomb repulsion and the electron beam diverges. This divergence of the electron beam may cause that some of the electrons hit the walls of the tube before arriving to the collector. The divergence of the electron beam in front of the Faraday collector and the wire is somewhat corroborated by the results from the measurements with the wire detector. The non-zero current at the edges of the scan indicates that some of the current is not collected by the plate and is not measured. We estimate that 26.4 % of the emitted current by the cathode is lost both in the second anode and in the tube walls before the collector.

The measurements with the wire detector show a displacement of the centre of the beam with respect to the centre of the waveguide. This indicates a certain misalignment of the beam, *e.g.,* that the direction of the magnetic field is not exactly parallel to the vacuum tube axis used as reference here. Another possible type of misalignment is that the magnetic field is parallel to the vacuum tube axis, however, that the electron beam is injected slightly off-axis.

We intended to gain further information related to these possible misalignments from measurements with the fluorescent YAG screen, which were done without the lined waveguide installed, to provide a wider field of view. A typical image of the recorded distribution of fluo-

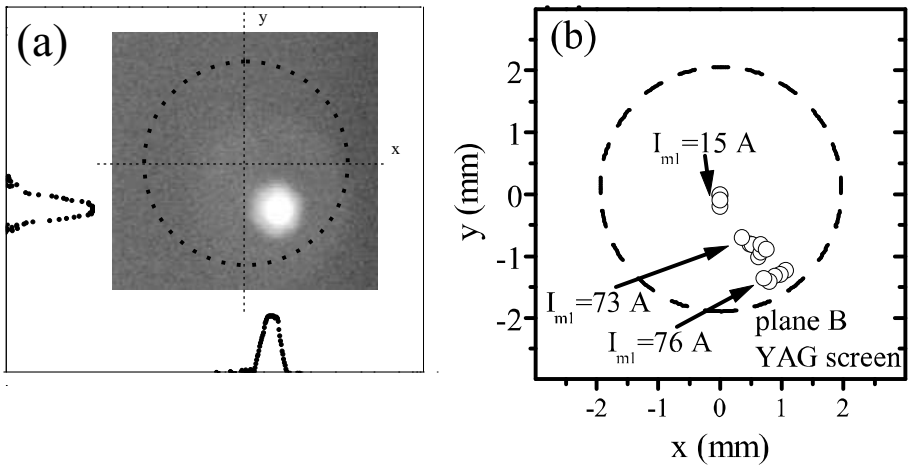

Figure 6.5: (a) Photograph of the fluorescence distribution in the YAG screen and intensity profiles, and (b) coordinates of the centre of the light spot in the YAG screen produced by the electron beam for different currents flowing through the first coil. The measurements are done without the lined waveguide installed but for reference, a dashed circle of the same diameter as the inner diameter of the lined waveguide is drawn in both graphs.

rescence is shown in figure 6.5 (a). The figure shows a photograph of the fluorescence captured by the CCD camera, and, projected on the axes, the corresponding horizontal and vertical intensity profiles. For reference, the dashed circle indicates the 2 mm inner radius of the lined waveguide to be installed for the next set of experiments (see below). It can be seen that the maximum intensity of the fluorescence distribution, *i.e.,* the centre of the electron beam, is off-axis for the specific settings of this example, which are 73 A in coil 1 and 11.5 A in coil 2. In order to investigate the misalignment of the electron beam to more detail, and also to identify the most promising settings of the experimental parameters for the subsequent radiation experiments, we have measured the coordinates of the electron beam for various different currents flowing through the coils of the solenoid, and thus for various magnetic fields strengths. We observed that the electron beam centre coordinates do not strongly depend on the current flowing through coil 2, as long as the coil current does not deviate by more than 2 A from the design value current of 13 A presented in chapter 5. However, we observe a strong influence of the current in coil 1 on the coordinates of the electron beam. We found that the beam coordinates shift from the centre of the screen as far as 1.5 mm when the current in coil 1 is kept around its design value.

For a more quantitative study of the named effects of the currents in the two coils, we have recorded the electron beam coordinates for several currents in coil 1, while keeping the current in coil 2 constant at a value of 11.5 A. The recorded data are shown in figure 6.5 (b), which shows the transverse position of the beam in plane B for several current pulses of 10 μs duration, for various currents sent through coil 1. Also here for reference, the dashed circle indicates the

inner radius of the lined waveguide to be installed in the next set of experiments. From the data in figure 6.5 (b) can be seen that at low currents in coil 1 (below 15 A) the fluorescence is well centred on the axis of the lined waveguide with a high precision of a small fraction of a millimetre. However, it can also be seen that, at higher current in coil 1 (73 A), required for laser operation according to the design, the beam centre becomes noticeably displaced from the z-axis (to x=0.7 mm, y=1 mm), and that at even higher current in coil 1 (76 A), the displacement is nearly as large as the inner radius of the lined waveguide.

The results from the measurements with the YAG screen show that the design of the first magnet is successful when operating at low magnetic fields. However, we conclude from the experimental data in figure 6.5 that, at high magnetic fields, as required for proper electron beam transport according to our design considerations, coil 1 would require a fine adjustment of its axis with respect to the axis of the electron gun. Unfortunately, this is not possible with the present construction, and is thus subject of an improved design. As was explained in chapter 5, in the present design, the tube of coil 1 transports both the water flow for cooling and the current flow for the magnetic field generation. Such a design produces a less homogeneous current density through the tube, and does not allow for a simple alignment of the coil with respect to the axis, which makes it difficult to achieve a perfectly homogeneous and parallel magnetic field on axis. Further, the two coils that form the entire solenoid have a small gap between them, as can be seen in figure 6.3, which produces a not perfectly constant magnetic field strength at the border between coil 1 and coil 2. To obtain a constant magnetic field on axis and an easy alignment of the solenoid, the design should be improved by having the whole solenoid formed by a single coil thick enough to allow for a reduced current density. As was also explained in chapter 5, a thick coil was, however, not suitable for the current design of the electron gun chamber, but a re-design of the electron gun chamber can be consider in future improvements of the experimental setup.

To measure the possible loss of current due to the impact of the electrons on the walls of the liner, the last set of measurements was performed with the lined waveguide installed and with the Faraday collector placed at plane C as indicated in figure 6.3. As explained above, we recorded the current that reaches the collector as a function of time for each electron beam pulse. Although the grid was supplied with a rectangular switching pulse, the detected electron current pulse only roughly showed a rectangular shape. Typical temporal displays of detected current pulses, generated with rectangular grid voltage pulses of 10 μs and 20 μs duration, are shown in the examples of figure 6.6. The figure shows the fraction of collected current with respect to the total emitted current by the cathode as a function of time for four examples of electron beam pulses. For some of the pulses, *e.g.,* examples (a) and (b), it can be seen that, within one electron beam shot the received current varies strongly as a function of time. Further,

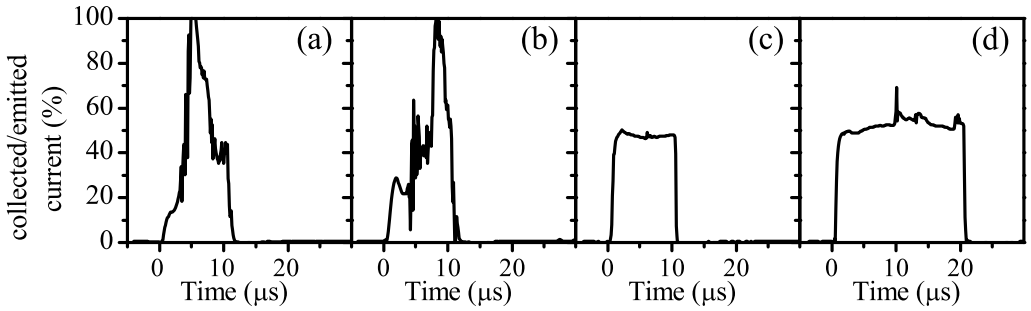

Figure 6.6: Examples of collected electron beam currents as a function of time, measured with the Faraday collector in plane C and with the lined waveguide installed.

the temporal pulse shapes of consecutive shots are different from each other. Some other pulses, *e.g.,* examples (c) and (d), showed an almost rectangular temporal pulse shape, independently of the pulse duration. We measured the average current received in each of the measured pulses, and averaged it over the number of pulses. The result shows that, on average, (52±7) % of the total current emitted by the cathode is detected at the collector. The irregular temporal shape of some of the electron beam current pulses, and the low percentage of current collected seem to indicate that the electrons impact on the walls of the dielectric liner. An expected consequence of the impact of the electrons with the walls of the liner is a charging of the liner material. If that occurs, the deposited charge would cause an uncontrolled focusing or defocusing of the electron beam that, in some cases, can lead to an improved transport of part of the electron beam through the liner. For example, if the leading edge of an electron beam pulse impacts with the walls of the liner and charges the material, the charge on the walls can induce a focusing of the remaining part of the pulse. This would explain the high detection of current observed in the middle of pulse (a) and near the end of pulse (b) in figure 6.6.

In these measurements, we could only measure the total current detected at the Faraday collector and not the spatial distribution. However, after removing this collector from the experimental setup, we have inspected the damage pattern on the collector disk made by the impact of the electrons. We observed that the damaged area typically lies about 1 mm off the centre of the disk. This is consistent with what is seen in figure 6.5 (b), which shows an off-axis propagation of the beam as well. The observation thus corroborates the misalignment of the electron beam due to the first magnet, and the installation of a fine adjustment.

In summary, we have observed that the current transported through the lined waveguide amounts to about 50% of the total current emitted by the cathode, and that the installation of a fine adjustment of the position and axis of the first coil would enable to achieve much improved

on-axis propagation in a next design. The measurements of the electron beam transport seem to indicate that misalignment of the first magnet with respect to the axis of the waveguide forms the main reason for the current loss. We have, during the course of the current project, not attempted to more thoroughly investigate and thereafter remove the named misalignment. The reason for this choice is that corresponding considerations had shown that such improvement would have required to replace the solenoid. This would then have required a major modification of the entire setup, specifically, the second anode would have to be redesigned. Instead, we decided to continue the experiments with the central goal to demonstrate the generation of radiation, even if this was under the presence of misalignment. This decision was based on the observation that the electron beam remained well centred when the current in the first coil was kept low, and that the available beam current of a few hundred milliamperes travelling through the lined waveguide should theoretically enable the generation of laser radiation.

6.3 Radiation measurements

In sections 6.1 and 6.2, it was described that, in pulsed operation (pulses tens of microseconds long), 50 % of the emitted current travels through the entire length of the lined waveguide, *i.e.,* a maximum pump current of approximately 250 mA is available for wave amplification. In the present section we describe measurements of the radiation emitted by the CFEL with that electron beam current. As was described in the introduction of this thesis, attempts to observe Čerenkov radiation had been done in two steps of the project:

1. The first step consisted in designing and building the CFEL as an oscillator with a quartz-lined waveguide for the generation of frequencies in the higher-frequency band (V-band). This included the first attempt to detect microwave radiation and, indeed, radiation was detected in this band. However, as will be described in the next section (6.3.1), the emitted power was rather low and appeared incoherent because it was distributed across a wide range of frequencies. Although undesired on a first glance, we note that these results have actually triggered a second, rather important phase of investigation which is the first theoretical description of liner-induced losses for CFELs (chapter 2).

2. In the second step, however, only after having modified the former experimental design to one with much less susceptibility to losses, a second attempt to observe radiation was done. Based on our theoretical investigations described in chapter 2, we expected much lower losses by moving to the lower-frequency band (K-band) with an alumina-lined waveguide, which promised that, in single-pass amplification, several watts of output should be observable. Indeed, this second attempt was successful. Narrowband (*i.e.,*

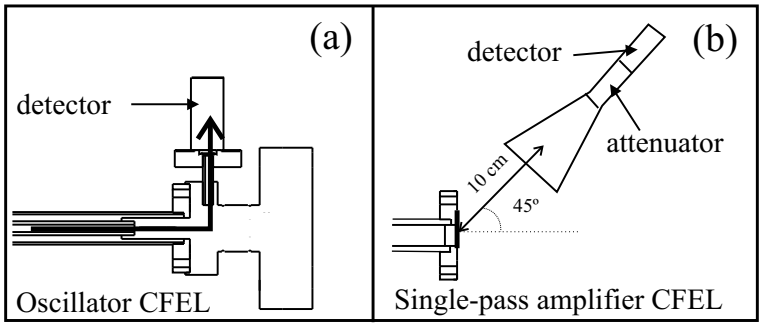

Figure 6.7: Setup for the detection of output radiation from the CFEL configured as (a) oscillator, and as (b) single-pass amplifier.

coherent) radiation was observed which was tunable via the accelerating voltage, in consistency with stimulated Čerenkov emission. We note that these results, although still far from a complete experimental characterization and optimization, actually form a very important breakthrough. They prove that Čerenkov lasers can indeed be brought into operation with very desirable properties, namely, a compact design based on low currents and moderate acceleration voltages. The observation of narrowband emission is of high importance because from now on, the much easier phase of systematic characterization of the source can start. This is, actually, the beginning of a stepwise engineering towards a source with its output performance and specifications optimized for particular applications.

6.3.1 Preliminary measurements with a quartz-lined oscillator

The setup for the measurement of the output radiation from the CFEL configured as an oscillator is shown in figure 6.7 (a). Here, we use the output coupler which was described in chapter 5. As explained there, the output coupler forms the transition between the cylindrical waveguide of the CFEL, which is non-standard, to rectangular waveguides, specifically, the type WR19, which are standard for frequencies between 40 GHz and 60 GHz. Two types of detectors were mounted to the rectangular waveguide output port. To measure the spectral power distribution, we used an Agilent E4407B spectrum analyser with an external mixer that allows for detecting frequencies up to 60 GHz. A frequency scan is performed by triggering the RF spectrum analyser at the CFEL repetition rate. To measure the power for each radiation pulse, we used a Flann-24510NJ crystal detector. This detector rectifies and squares the incident field, providing a signal with an amplitude proportional to the input power level. This signal is sent to an oscilloscope that traces the power detected as a function of time for a single pulse. Finally, as described in chapter 5, the phosphorous screen of the output coupler is coated with an aluminium layer that allows for measurement of the electron beam current as a function of time for each radiation pulse.

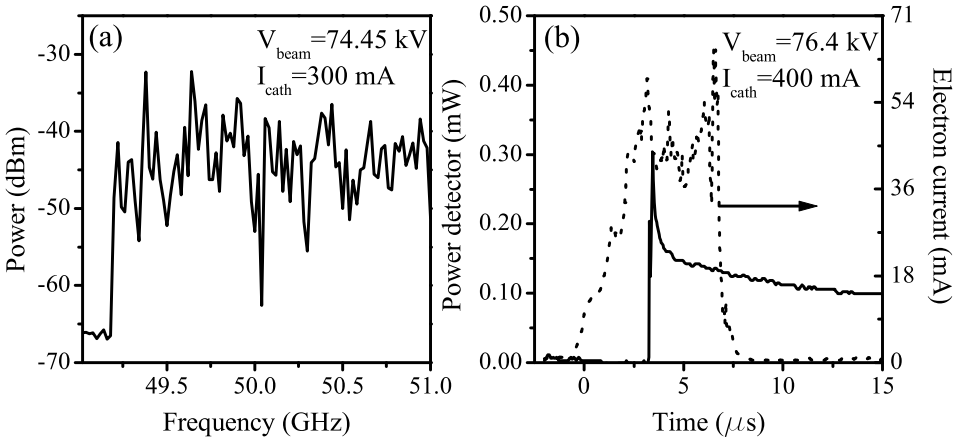

Figure 6.8: (a) Measured spectrum with the CFEL configured as oscillator. The acceleration voltage is 74.4 kV and the electron beam current emitted by the cathode averaged over the total number of pulses is approximately 300 mA. (b) Detection signals of the electron beam current (dotted line) and microwave power (continuous line) as a function of time for a 7 μs long pulse.

The measurements showed that weak radiation is emitted within the entire 40-60 GHz range in the form of a mostly flat spectrum. A typical power spectrum of the output is shown in figure 6.8 (a). In this example, the acceleration voltage of the electron beam was set to 74.45 kV and the electron beam current emitted by the cathode averaged over the total number of pulses was approximately 300 mA. For this measurement, the CFEL was pulsed with a repetition rate of 1 Hz during 200 s and with pulse lengths of 10 μs, and the spectrum analyser was set to measure within a frequency span of 2 GHz centred at 50 GHz. We found a spectral signal, only present when the electron gun was in operation. It can further be seen that the spectrum is approximately flat. The same response was observed for all the spectral measurement within the entire 40-60 GHz range. A typical measurement of the electron beam current and radiation power as a function of time is shown in figure 6.8 (b). This figure shows the detected electron beam current as a function of time with a dotted line, and the voltage signal from the crystal detector as a function of time with a continuous line. The measurement is taken for a 7 μs pulse, for a cathode electron beam current of 400 mA, and for an acceleration voltage of 76.4 kV. It can be seen that the current pulse is only roughly rectangular because it contains several temporal peaks and dips. We note that only the overall rectangular shape but not the finer temporal structure (appearance of peaks and dips) is reproducible from pulse to pulse. For this specific example, the maximum current detected is about 60 mA in a spike near the end of the overall rectangular pulse shape. Note that the actual current used for the amplification is larger than

this value since some of the electrons are lost in the mesh and walls of the outcoupler, as was described in chapter 5. In figure 6.8 (b) it can be seen that the inset of microwave emission was detected to be delayed by approximately 2.5 μs with regard to the beginning of the electron beam pulse. The radiation pulse initially peaks and then decays slowly beyond the end of the electron beam pulse. This decay is given by the RC-time of the detector capacitance and the oscilloscope impedance. The high impedance of the oscilloscope, 1 MΩ, explains the slow decay of the detector signal after the end of the electron beam pulse.

As shown in chapter 4, the ideally expected radiation should have a narrow gain bandwidth of about 0.5 GHz, and high output powers in the kilowatt range for the originally devised electron beam current of 800 mA. In the measurement displayed above, the maximum electron beam current measured at the phosphorous screen of the outcoupler is only 60 mA. To estimate the amount of current travelling through the liner in the same example and thus available for wave amplification, one should add the 32 % of the total current lost in the mesh and the walls of the output coupler as explained in chapter 5. This means that the maximum of 60 mA correspond to a maximum of about 180 mA travelling through the waveguide for the example shown in figure 6.8 (b). We have calculated that, for these currents, a power of still several tens of watts should be expected. Instead, the results presented above show a much lower power emission (about 0.3 mW) distributed over the entire observable frequency band, *i.e.,* from 40 GHz to 60 GHz.

In summary, the shown results obtained with the quartz-lined oscillator setup reveal that the gain in the interaction region is not high enough and also does not last long enough to overcome the roundtrip losses in the RF resonator. The low electron beam current available for wave amplification is a clear reason of gain reduction. Nevertheless, even with weak pumping, *e.g.,* 100 mA, we calculated that it is enough to provide lasing with a few hundreds of watts of output power. The absence of laser oscillation motivated us to look into further reasons of losses, which we associated to the liner used for the interaction. As we explained in the introduction of the thesis, it was the set of data recorded during these experiments that motivated us to develop the thorough theoretical investigation of gain reduction in Čerenkov lasers caused by liner induced phase velocity fluctuations [105]. From chapter 4 we recall that, to achieve amplification at 50 GHz, the quartz liner should have tolerances in the inner radius well below 5% to reach the laser threshold. However, the tolerance of the quartz liner during this experiments was as large as 10 %. From these reasons, for insufficiently high gain, and from the observed properties of the emitted radiation, we conclude that the detected radiation is not stimulated Čerenkov emission.

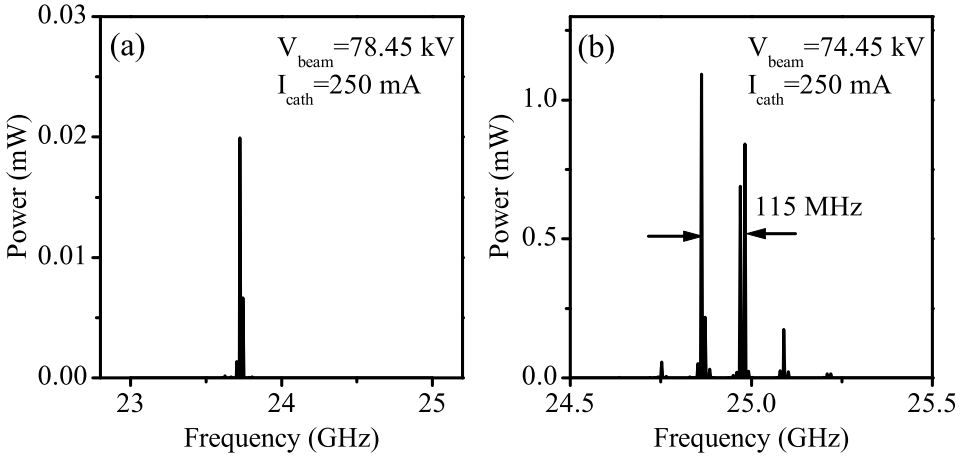

Figure 6.9: Typical spectral power distribution measurements in the CFEL configured as single-pass amplifier for (a) 78.45 kV, and (b) 74.45 kV accelerating voltages, and for 250 mA electron beam current in both cases.

6.3.2 First lasing with the alumina-lined single-pass amplifier

As was described in chapter 4, an alumina liner was used in the experimental setup of the CFEL configured as a single-pass amplifier. In this case, the liner fulfils some conditions learnt from the previous experiment. To reduce the number of impacts of the electrons in the walls of the liner, we used an inner liner diameter of 4 mm, and to avoid gain degradation produced by the liner radius fluctuations we used a precision liner of 3 % tolerance. The setup for the measurement of the output radiation from the CFEL configured as single-pass amplifier is shown in figure 6.7 (b). The waveguide used for dumping the electron beam, as described in chapter 5, ends in a polyethylene window, which forms both the vacuum window and the output coupler of the radiation. A microwave horn (model 20240 from Flann Microwave) is placed at a distance of about 10 cm from the output window. In order to measure the spatial distribution of the radiation, the horn can be swept widely ($\pm$ 90 degrees) around the axis of the waveguide. A variable attenuator (model 20020 from Flann Microwave) is connected between the horn and a detection device. Two types of detectors were used with this setup, to measure the relative spectral distribution of the radiated power, and to measure the total absolute power. The spectral power distribution was measured with the RF spectrum analyser, using the internal mixer that allows for detection of frequency up to 26.5 GHz. As before, the frequency sweeps of the local oscillator in the RF analyser are triggered with a pulse from the CFEL electronics at the CFEL pulses repetition rate. A typical frequency span covers a range of 2 GHz and is recorded using 100 electron beam pulses. With these settings we measured the RF frequency emitted

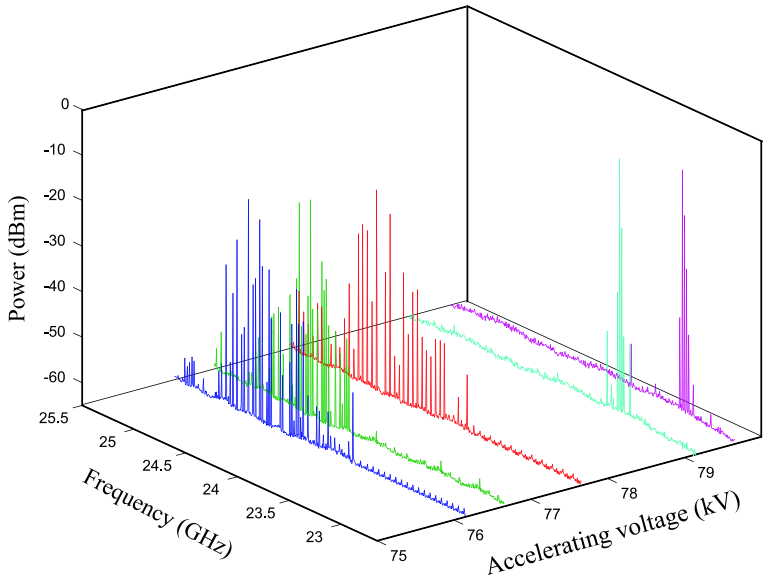

Figure 6.10: Spectral power distribution measurements for the CFEL configured as single-pass amplifier for various accelerating voltages of the electron beam.

by the setup, or its spectral distribution, as a function of the accelerating voltage, which will be named the tuning curve of the CFEL. To measure the absolute total power of the radiation (spectrally integrated) in each radiation pulse, we used a waveguide Hewlett Packard K422A crystal detector. The detector rectifies and squares the incident field, providing a signal with an amplitude proportional to the input power level. This signal is sent to an oscilloscope, which then displays the power of the radiation as a function of time. As the laser settings, we used for these measurements accelerating voltages between 74 kV and 79 kV, and the used current measured at the cathode was set in a range between 300 mA and 500 mA.

With these settings we observed a clear sign of laser emission, which can be considered an important success, namely, a first lasing of a compact CFEL. To more detail, the detected radiation showed the following properties. The frequency of emission was found in the range between 23 and 26 GHz and this frequency depended on the accelerating voltage. Two examples of emission spectra are shown in figures 6.9 (a) and (b). The acceleration voltages were 78.45 kV and 74.45 kV, respectively, and the pump currents were 250 mA in both cases. Both spectra were recorded with a repetition rate of 1 Hz and a sweep time of the RF analyser of 100 s. The frequency spans of the RF analyser were 2 GHz and 1 GHz, respectively. The spectrum in figure 6.9 (a) shows that the power peaks at a frequency of about 23.75 GHz, and the signal has a FWHM of approximately 20 MHz. The spectrum in figure 6.9 (b) shows that the power peaks at several frequencies, separated approximately 115 MHz from each other, and that the maximum power peak corresponds to 24.86 GHz. The equidistant frequency peaks seem to indicate the existence of several longitudinal modes, and thus that the laser oscillates. In

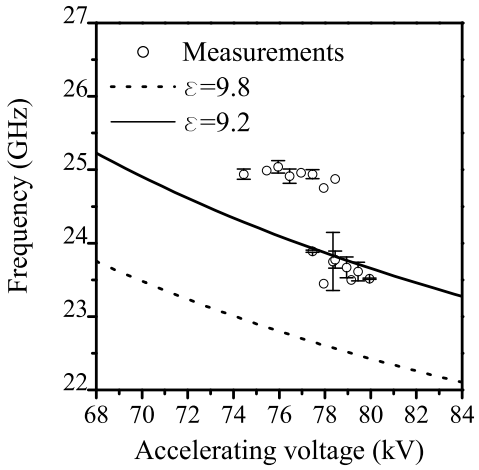

Figure 6.11: Frequency of the radiation as a function of the accelerating voltage for the CFEL configured as single-pass amplifier. The theoretical tuning curve for $\epsilon = 9.8$ (dotted line) and for $\epsilon = 9.2$ (solid line) are also shown.

chapter 5 was shown that the alumina-lined taper, used for the transition from the CFEL lined waveguide to the empty waveguide, has a reflectivity of approximately 10 % for the frequency range of the experiments. In the experimental results shown here, we observe that, indeed, the CFEL exhibits spectral properties typical of a resonator.

The same type of measurement is shown in figure 6.10 for several accelerating voltages. To show more details on the spectral distribution, we have used here a logarithmic power scale. It can be seen that the peak shifts to lower frequencies as the accelerating voltage is increased. We have recorded the peak frequency for each measurement, and we have displayed them as a function of the accelerating voltage in figure 6.11. This figure again shows that the peak frequency of emission systematically decreases for increasing accelerating voltage. The corresponding slope of frequency change versus accelerating voltage, which we call the tuning rate, is about -0.15 GHz/kV. One can also see that the experimental data points form two groups, with a frequency gap between them.

To compare the measured emission frequencies shown in figure 6.11 with theory, we have drawn in figure 6.11 the tuning curve for a liner with various dielectric constants and for the fixed dimensions of r_d=2 mm and r_g=3.5 mm. The dashed line corresponds to a dielectric constant of 9.8, as was used in chapter 4. The solid line has been obtained using the dielectric constant of 9.2, as specified by the manufacturer for a frequency of 10 GHz. It can be seen that the solid line matches well the absolute value of the observed frequency of the laser for voltages above 77 kV. Also, the rate of tuning (about -0.14 GHz/kV) matches the experimental rate, which is -0.15 GHz/kV. Nevertheless, the question remains why the laser frequency jumps

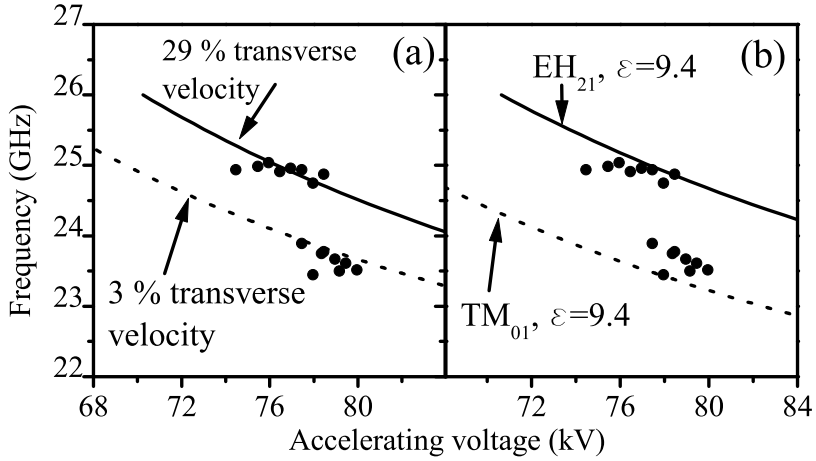

Figure 6.12: Theoretical tuning curves of the alumina-lined CFEL (a) when 3 % (dotted line) and 29 % (solid line) of the electrons momentum is contained in the transverse momentum and (b) for the TM_{01} (dotted line) and the EH_{21} mode (solid line) when ϵ =9.4. The measurement results (solid circles) are also plotted.

by approximately 1 GHz at an acceleration voltage of about 78 kV. To explain the measured oscillation frequencies, several physical mechanisms can be considered.

A first possible explanation is related to the trajectory performed by the electrons. As was described in chapter 2, only the longitudinal component of the velocity of the electrons is responsible for maintaining the phase matching between electron beam and wave, and therefore for determining the operating frequency. As explained previously in this chapter, the electron beam in the experiment undergoes a type of helical motion. In such trajectories, a fraction of the total kinetic energy is contained in an azimuthal rotation, which reduces the longitudinal momentum. This should be considered in the calculation of the tuning curve of the CFEL, where, via the dispersion relation, we calculate the accelerating voltage required to excite a specific frequency. Our calculations of the dispersion curve assume that the accelerating voltage is fully employed in the longitudinal velocity, and does not include the transverse motion. Due to the transverse motion, the actual longitudinal velocity, which determines the frequency of the amplified wave, is reduced, which would increase the oscillation frequency. With this mechanism, the frequency jump by 1 GHz may have been caused by a corresponding change in transverse velocity. To test this assumption, we refer to the results obtained in chapter 5 with the electron beam tracing calculation. There it was found that the expected transverse velocity is at least 3 % of the total velocity. We also note that this transverse momentum underestimates the experimental transverse momentum, because we found in section 6.2 that part of the solenoid is slightly misaligned. Therefore, a transverse velocity higher than 3 % of the total velocity is ex-

pected to be present in the experiment. To show the effect on the calculated operating frequency, we have plotted in figure 6.12 (a) the resonant frequency for a transverse momentum equal to 3 % of the total momentum (dotted line). We note that the curve is not noticeably different from the curve with zero transverse momentum (compare with figure 6.11). Figure 6.12 (a) also shows the tuning curve for a 29 % transverse momentum (solid line) that is required to fit the experimental data (solid circles). However, we find such a large spread of velocity very unrealistic.

A second possible explanation is as follows. From the measurements of the electron beam transport it can be seen that the electron beam propagation is not fully axially symmetric. Therefore the electron beam can possibly excite modes with no azimuthal symmetry, which are hybrid modes. Hybrid modes have both the electric and magnetic field pointing along the axis of the waveguide and, although less efficiently than a TM mode, they can still interact with the electrons if the phase velocity of the wave is adequate. In order to find higher order modes resonating at the frequencies observed in the experiments we have calculated the tuning curve for several of these modes. In particular, we found that the frequencies of the EH_{21} and TM_{01} match the experimental results rather well, as can be seen in figure 6.12 (b). This indicates that, for voltages between 78 kV and 80 kV, the laser oscillates on the fundamental TM_{01} mode, whereas for voltages between 74 kV and 77 kV, the laser oscillation hops to the higher order EH_{21} mode. Note that, in order to better match the experimental values, a slightly higher dielectric constant of the material was used ($\epsilon = 9.4$ instead of $\epsilon = 9.2$). However, such rise can be explained based on the temperature dependence of the dielectric constant [76]. For example, measurements of the dielectric constant of a sample of 95 % purity, at a frequency of 3 GHz, showed a 3 % increase when the temperature was raised from 25^o C to 200^o C [76]. In our experiment, the temperature of the liner may have increased due to the following mechanisms. First, the power dissipated by dielectric losses of the liner should rise the liner temperature, but our estimates shows that this should be a minor contribution, considering the moderate power of the laser radiation observed. A second possibility is that the liner is simply heated by surrounding heat sources. As was described in chapter 5, we observed that the solenoid around the lined waveguide section exhibited an elevated temperature of up to 116 ^{o}C during operation. From estimates on heat conduction and radiation we expect that this may have raised the temperature of the liner to more than 100 ^{o}C, which would explain an increase of the dielectric constant, from 9.2 to 9.4.

In summary, the transverse velocity of the electrons, the excitation of two different modes and the temperature dependence of the dielectric constant can explain the two groups of experimental data observed in figure 6.11.

The measurements of the power as a function of time, using the crystal detector, showed

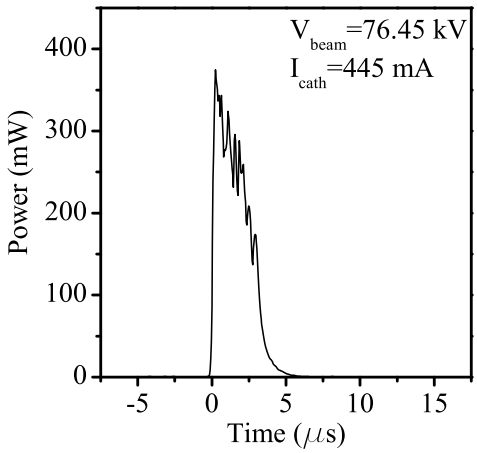

Figure 6.13: Typical measurement of the power as a function of time for a single pulse in the CFEL configured as single-pass amplifier.

the detection of radiation pulses of the same duration as the electron beam pulses. Further, the detection is maximum when the horn forms 45 ^{o}C with the axis of the waveguide, as shown in figure 6.7. A typical measurement of the power of the radiation as a function of time is shown in figure 6.13. This measurement was recorded with an electron beam pulse of 445 mA peak current and 5 μs long duration, and with an acceleration voltage of 76.45 kV. It can be seen that the maximum power detected yields a value of 350 mW. It can be observed that the pulse is not perfectly rectangular, but shows a maximum power level at the beginning of the pulse, and a power level decreasing with the pulse duration.

The power shown in figure 6.13 is a measurement of the power collected by the horn, which is only a fraction of the total emitted power. In order to compare the experimental and theoretical output power, the total emitted power by the CFEL has to be estimated. Although a complete spatial map of the output power distribution was not measured, we saw that the maximum emission occurs for approximately 45 ^{o}C. This angle seems to be consistent with the maximum of the expected power spatial distribution of the modes amplified inside the lined waveguide. Thereby, one can assume a torus-like distribution of the electromagnetic power when the wave propagates in free space. Assuming this shape, approximately a 10 % of the total radiation outcoupled from the window would be collected by the horn. For the typical example shown in figure 6.13, the maximum total emitted power by the CFEL would then be of the order of 3.5 W.

The measured emitted power has to be compared with the calculated output power. In chapter 4, for a voltage of 77.1 kV and at a frequency of 22.4 GHz, the alumina-lined CFEL was predicted to emit more than 3 kW output power for a few percent reflected power. This

predicted power seem to be much larger than the experimental result. For a better understanding of the discrepancy between the expected and the obtained powers, let us review the parameters that were used for the calculations. In chapter 4, we used a pump current of 800 mA, negligible dielectric losses of the liner, no liner radius fluctuations, and an energy spread of 1 %. However, now it is to be noticed that many of the parameters used there possess quite different values in the present experimental setup. Such is the case for the total electron beam current available for amplification of the wave. Our measurements of the electron beam transport showed that only a maximum of about 250 mA is actually travelling till the end of the lined waveguide and not 800 mA. Also, during the experiments the tangent loss can be as high as 10^{-3}, due to the temperature of the liner elevated to above 100 ^{o}C [81]. Furthermore, the manufacturer of the liner specified a radius tolerance of 3%, or equivalently an rms fluctuation of 60 μm. Finally, our electron beam transport measurements had shown that the electron beam quality is somewhat degraded due a small misalignment of the first magnet such that the resulting effective energy spread can easily be as high as 5 %.

To quantify the effect of such experimental conditions on the outcoupled power expected from the CFEL, we have calculated the output power produced a 250 mA electron beam current, a tangent loss of 10^{-3}, an rms value of liner radius fluctuations of 60 μm, and an energy spread in the electron beam of 5 %. We chose an acceleration voltage of $V_b = 77.1$ kV, for which lasing occurs at 22.24 GHz. The result showed that, with those parameters and 10 % reflectivity in the resonator, an output power of (0.13$\pm$0.13) mW is expected. The larger uncertainty in the result comes from the large standard deviation produced by the liner fluctuations. This result is even lower than the power obtained experimentally. This can be because the energy spread might be lower than assumed here, or the dielectric losses might suffer a less severe increase as we assumed here. The large number of free parameters, makes it difficult to attempt to perform a fit-procedure with the experimental data. Besides, we also note that in the analysis of the tuning curve, the possibility of exciting the mode EH_{21} was pointed out. Since such a mode is a hybrid mode, the coupling of the electrons with the EH_{21} mode is not so efficient as with the TM_{01} mode, which, in principle, would result in a lower output power, although it cannot be calculated with our model. However, the result presented here based on the excitation of the TM_{01} mode shows that, with a low electron beam current and several type of losses, the predicted output power from the CFEL remains about the same order of magnitude as the results we have obtained experimentally.

In summary, we have shown the first demonstration of lasing in a table-top Čerenkov FEL. Thereby we have opened the way to a systematic characterization of such devices, and to a further engineering of such devices in the direction of specific applications. As the initial steps of such characterization, we measured a maximum output power of about 3.5 W at microwave fre-

quencies in the K-band at frequencies around 24 GHz. The output was spectrally narrowband, with typical bandwidths in the order of 20 MHz. The output is emitted in the form of pulses with, currently, 5 μs duration, which is equal to the pumping electron beam pulse length. The output frequency was found to be tunable with the accelerating voltage, with the same rate as calculated for the CFEL under investigation. The experimental output power is consistent with the theoretical prediction, when considering the several mechanisms present in CFELs, such as dielectric losses in the liner, radius fluctuation of the liner, and the energy spread of the pumping electrons.

Based on this consistency, we can predict particular improvements in the setup and which scaling of parameters would considerably increase the laser output towards the kilowatt level.

7

Summary and conclusions

In this thesis, the first realization of a millimetre wave emitting Čerenkov laser (CFEL) in table-top format has been demonstrated, where operation is based on a low-current and low-voltage electron beam. Within a comprehensive theoretical model we show that such lasers offer a high potential as high-power and widely tunable microwave sources. Such sources, especially due to their compact format, can be of high interest in a wide range of applications, and might also lead to novel applications.

The overall approach of this thesis is the question whether free-electron lasers can be down-scaled in size, by the use of low currents below the 1 A level and by use of a low kinetic energy of the electron pump current, however, while retaining a low pump threshold and high output power. As with any attempt to scale lasers into novel regimes of performance, there is a considerable risk of failure, namely, that the pump threshold to overcome the losses cannot be reached. To address such issues in a realistic manner, in the first part of this thesis we developed a comprehensive theoretical model of the laser which allows, for the first time, to describe two loss mechanisms present associated with the liner of Čerenkov lasers. Although previous models of the dynamics of FELs include various types of loss mechanisms, those models are mainly inspired by undulator-type FELs thus lack the possibility to describe losses associated with the dielectric liner, which is responsible to provide the gain in Čerenkov-type FELs.

The first effect we consider is the dissipation of power due to dielectric loss in the liner material, and the second is a degradation of the gain due to geometrical imperfections of the liner as can be caused, *e.g.,* during its manufacturing. To include the first effect, we have generalized the Čerenkov FEL model of Freund [55] by introducing a complex number for the dielectric constant of the liner material. With this, we re-derived the dispersion relation of the lined waveguide where dielectric liner losses are characterized by the imaginary part of a complex wavenumber. The dynamic CFEL equations have been subsequently derived with the complex wavenumber. The second cause of loss considered here, slight imperfections of the liner tube, has been modelled by letting the wavenumber vary randomly with the longitudinal coordinate of propagation through the liner. To first approximation, we found that the variation

of the wavenumber causes a variation of the phase velocity during interaction with the electron beam while the transverse mode profile is preserved. The named variations of the phase velocity affect the formation of the bunches and, thereafter, also the relative phase between the bunches and the wave, resulting in a degradation of the laser gain. With the description of such mechanisms, this first part of the thesis provides a more complete model of CFELs where the output power from the laser can be calculated in the presence of imperfections that are unavoidable in an experimental realization. The availability of such generalized model is of high importance to predict whether laser operation would be possible, especially when the CFEL is to be pumped with a low current and low energy electron beam.

As preparation for addressing an experimental design of the CFEL, the model was used to investigate the expected gain and output power from, particularly, a low current-pumped in the presence of dielectric loss and liner imperfections, and for comparison, also from a stronger-pumped CFEL in combination with stronger losses. This theoretical study yielded two novel results of both conceptual and practical interest.

The first result was obtained with the analysis of a high-current pumped CFEL. We found that such CFELs show a spectrally broad gain bandwidth, with an appreciable gain at frequencies far below resonance, where low-current pumped CFELs do not show any wave amplification at all. The occurrence and reasons for such broadband gain has not been reported before, although this phenomenon is contained and can be explained with known models of CFELs. We have explained the physical mechanism behind such amplification off-resonance as follows. With strong pumping the electron density becomes sufficiently high to strongly drive the phase of the wave. This reduces the phase velocity by precisely the amount which is required to match it to the velocity of the electrons. With such synchronization, the electrons can transfer energy to the field, and amplify the wave.

The second and quite surprising result was found in the regime of high pump current as well, when we intended to study a presumable reduction of the laser output with increasing dielectric liner losses. However, we found that the off-resonant output power does not become reduced when the losses are increased. Instead, the output power remains approximately constant up to substantial loss values. At the same time, we found that the power dissipated in the liner increased with the losses as expected. Apparently and, to our knowledge, in contrast to any other laser system, the amplification of the wave becomes *bigger* when one adds losses. This extra power amplification exactly equals the power dissipation, thereby making the output from the CFEL independent of the losses.

Besides these results of more fundamental relevance, the numerical investigation provided a wealth of information essential for an experimental design. More specifically, we found that a rather critical point can be dielectric loss and fabrication errors of the liner, especially in weakly

pumped CFELs considered here. As these parameters are usually not well specified and because the dielectric loss can also depend on the operating conditions, there is a substantial risk that a weakly-pumped CFEL would fail to oscillate.

The second part of the thesis was devoted to demonstrate the operation of a low-current and low-voltage pumped CFEL. To come to a specific and compact design to be realized we restricted ourselves to a set of pumping and performance parameters. This comprises an electron beam current of less that 800 mA from a commercially available gun, a pre-acceleration voltage of 10 keV, and total acceleration voltage of less than 100 keV, to generate microwave emission in the V-band and the K-band. Two liner designs were selected to provide wave amplification at the nominal frequencies of 50 GHz and 22 GHz, namely, a 1.3 mm thick quartz liner of 3 mm inner diameter and a 1.5 mm alumina liner of 4 mm inner diameter, respectively. To preserve small sizes of the overall setup, in both cases the lined waveguide was limited to 25 cm long. In order to produce adequate output power within such a small distance, the quartz-lined design requires to configure the CFEL with a microwave resonator. The specific needs of the CFEL, that are derived from the combined propagation of the electron beam and of the electromagnetic wave, require tailored designs for the acceleration and transport of the electron beam and for the outcoupling of the wave from the resonator cavity. Emphasis has been put on converting the circular geometry of the interaction region to a rectangular geometry, so that standard microwave components can be used to guide the generated radiation to, *e.g.,* measurement devices or applicators. We have designed a tailored microwave mirror that provides feedback of radiation to the lined waveguide. In summary, the entire setup is formed by the electron gun containing the commercial 10 kV electron source, a post-acceleration section, the lined waveguide section, a resonator with outcoupler, and the electron beam transport mechanism.

In the last part of the thesis, we experimentally demonstrate the successful operation of the designed low-current and low-voltage CFEL. The experiments provided the first working CFEL pumped by less than 1 A current and with electron energies below 100 keV. With weak pumping, *i.e.,* with an electron beam of approximately 250 mA current and 80 keV kinetic energy, we obtained an output power of several watts in the K-band, centred at around 24 GHz. This power level is consistent with the experimental electron beam parameters, *i.e.,* about 250 mA electron beam current and 5 % energy spread, and also with the properties of the alumina liner, *i.e.,* a maximum tangent loss of 10^{-3} and 3 % tolerance of the liner radius. The emitted radiation was tunable via a tuning of the acceleration voltage at a rate of -0.15 GHz/kV, which is in excellent agreement with the tuning rate predicted by theory. On the other hand, our attempts to generate tunable laser emission at around 50 GHz, in the initial experiments during the beginning of the project, had failed, due to excessive tolerances of the liner radius. However, this failure, actually, had led us to a much improved modelling of the laser and, thereby, to successful operation at

24 GHz, based on an improved design with an alumina liner.

After such first improvement regarding the liner properties, further improvements of the setup should also yield substantially higher output power. Specially, a good-quality electron beam transport through the waveguide and energy spreads of around 1 % should rise the gain levels considerably. These improvements of the setup seem realistic with a redesign of the electron beam transport system and of the electron gun chamber, in a way that allows for a more accurate regulation of the magnetic field and for a better cooling of the waveguide. With such enhancement of the electron beam transport, in the limit of low dielectric loss (below 10^{-3}), which can be achieved for moderate temperatures of the liner, and by using precision machined liners, we expect that, with 800 mA and 75 keV, the quartz and alumina lined waveguides allow for reaching the kilowatt level for 50 GHz and 22 GHz, respectively. In particular, a quartz-lined CFEL should be able to produce about 2 kW output power at 50 GHz, and an alumina-lined CFEL about 3 kW output power at 22 GHz. These large output powers indicate the high future potential of compact CFELs. A huge number of industrial uses can be thought for the CFEL, which could be installed as wide-spread as currently found with the magnetrons.

Finally, the theoretical model and experimental results presented in this thesis also enable to look upon a further scaling of CFELs, in which the emission frequency is brought into the THz range. Terahertz radiation covers the electromagnetic spectrum between microwaves and far infrared radiation where numerous potential applications are being investigated or have been identified. However, the lacking availability of powerful, compact and tunable sources in the THz range is a main obstacle for the implementation of such applications. In a previous work, we have shown that, by reducing the diameter of the CFEL lined waveguide, the CFELs should be able to produce output powers in the 100 mW range at frequencies above 1 THz [106]. This makes the CFEL a good candidate as compact terahertz radiation source.

In summary, we have demonstrated that CFELs are promising as compact sources of tunable high power microwave radiation. This potential is clearly worth to be exploited for the construction of smaller CFELs operating with higher power and at higher frequencies.

A

Modes in a dielectric-lined cylindrical waveguide

In the present appendix we describe the electromagnetic modes in the so-called cold waveguide of the CFEL, *i.e.*, the waveguide when the electron beam is not present. This waveguide is shown in figure 2.2 in chapter 2, where it can be seen that it is formed by a cylindrical metal waveguide with an inner radius r_g, lined with a dielectric material with inner radius r_d. In this waveguide two regions can be defined, namely, the vacuum region of permittivity ϵ_0, for radii less than r_d, and the dielectric region of permittivity $\epsilon = \epsilon_r/\epsilon_0$, for radii between r_d and r_g. The magnetic permeability is equal to the vacuum permeability μ_0 in both regions.

The general solution for the electromagnetic field propagation in such a lined waveguide is given by a superposition of solutions or modes of the lined waveguide. As described in chapter 2, for a cylindrical coordinate system with azimuthal symmetry, each mode can be written as a transverse eigenmode only depending on the radial coordinate r, and which propagate along z. For a monochromatic field of frequency ω, the general solution can be written as:

$$\begin{aligned} \vec{E}(\vec{r},t) = &\ \textstyle\sum_{n=1}^{\infty} \mathrm{Re}\left(\vec{\mathcal{E}}_n(r)\ A_n\ e^{i(k_{zn}z-\omega t)}\right) \\ \vec{B}(\vec{r},t) = &\ \textstyle\sum_{n=1}^{\infty} \mathrm{Re}\left(\vec{\mathcal{B}}_n(r)\ A_n\ e^{i(k_{zn}z-\omega t)}\right) \end{aligned} \tag{A.1}$$

where A_n is the field amplitude of the nth mode and $\vec{\mathcal{E}}_n(r)$ and $\vec{\mathcal{B}}_n(r)$ are the transverse eigenmodes with longitudinal wavenumber k_{zn}. The transverse eigenmodes are given by linear combinations of Bessel's functions, where the coefficients can be particularized to the specific geometry of the waveguide shown in figure 2.2 by applying the corresponding boundary conditions. The mathematical treatment can be simplified by using only the longitudinal components of the fields, $\mathcal{E}_{zn}(r)$ and $\mathcal{B}_{zn}(r)$, since the rest of the field components are expressed as a function of

the longitudinal components as

$$\begin{aligned} \mathcal{E}_{rn}(r) &= \tfrac{ik_{zn}}{\kappa_n^2}\tfrac{\partial \mathcal{E}_{zn}}{\partial r} \\ \mathcal{E}_{\theta n}(r) &= -\tfrac{i\omega}{\kappa_n^2}\tfrac{\partial \mathcal{B}_{zn}}{\partial r} \\ \mathcal{B}_{rn}(r) &= \tfrac{ik_{zn}}{\kappa_n^2}\tfrac{\partial \mathcal{B}_{zn}}{\partial r} \\ \mathcal{B}_{\theta n}(r) &= \tfrac{i\omega\epsilon_r}{\kappa_n^2 c_0^2}\tfrac{\partial \mathcal{E}_{zn}}{\partial r} \end{aligned} \tag{A.2}$$

Here, the transverse wavenumbers for the vacuum and dielectric regions defined in equations (2.7) have been used.

In order to find the expression of the transverse eigenmodes in the lined waveguide described above, and thus the general solution of the system, in the following we apply the boundary conditions to the longitudinal components $\mathcal{E}_{zn}(r)$ and $\mathcal{B}_{zn}(r)$. As said before, these components can be written as linear combinations of Bessel's functions, which we write here as

$$\begin{aligned} \mathcal{E}_{zn}(r) &= \begin{cases} A_1 J_0(\kappa_n r) + B_1 Y_0(\kappa_n r) & \text{for } 0 \le r < r_d \\ A_2 J_0(\kappa_n' r) + B_2 Y_0(\kappa_n' r) & \text{for } r_d < r \le r_g \end{cases} \\ \mathcal{B}_{zn}(r) &= \begin{cases} C_1 J_0(\kappa_n r) + D_1 Y_0(\kappa_n r) & \text{for } 0 \le r < r_d \\ C_2 J_0(\kappa_n' r) + D_2 Y_0(\kappa_n' r) & \text{for } r_d < r \le r_g \end{cases} \end{aligned} \tag{A.3}$$

where J and Y are Bessel functions of first kind and second kind, respectively, and $A_1, \ldots, D_2$ are constant coefficients.

A first boundary condition determines that the fields in the axis of the waveguide are finite. Due to the properties of the Bessel function of second kind [74], this thus leads to $B_1 = D_1 = 0$ in equations (A.3). Further boundary conditions for the fields are imposed at the interface between the vacuum and the dielectric regions of the waveguide, and can be written as

$$\begin{aligned} \vec{n} \cdot (\vec{D}_2 - \vec{D}_1) &= 0 \\ \vec{n} \times (\vec{E}_2 - \vec{E}_1) &= 0 \\ \vec{n} \cdot (\vec{B}_2 - \vec{B}_1) &= 0 \\ \vec{n} \times (\vec{H}_2 - \vec{H}_1) &= 0 \end{aligned} \tag{A.4}$$

where the subscripts 1 and 2 refer to each of the two regions. Here, $\vec{D} = \epsilon \vec{E}$ is the displacement vector and $\vec{H} = \frac{1}{\mu_0}\vec{B}$ is the magnetic induction. Using the equations (A.3) in (A.4) yields the

following independent equations:

$$\begin{aligned}
A_1 J_1(\kappa_n r_d) &= \tfrac{\kappa_n \epsilon_r}{\kappa'_n}(A_2 J_1(\kappa'_n r_d) + B_2 Y_1(\kappa'_n r_d)) \\
A_1 J_0(\kappa_n r_d) &= A_2 J_0(\kappa'_n r_d) + B_2 Y_0(\kappa'_n r_d) \\
C_1 J_1(\kappa_n r_d) &= \tfrac{\kappa_n}{\kappa'_n}(C_2 J_1(\kappa'_n r_d) + D_2 Y_1(\kappa'_n r_d)) \\
C_1 J_0(\kappa_n r_d) &= C_2 J_0(\kappa'_n r_d) + D_2 Y_0(\kappa'_n r_d) \\
A_2 J_0(\kappa'_n r_g) &+ B_2 Y_0(\kappa'_n r_g) = 0 \\
C_2 J_1(\kappa'_n r_g) &+ D_2 Y_1(\kappa'_n r_g) = 0
\end{aligned} \tag{A.5}$$

The set of equations (A.5) has non-trivial solution if the following conditions fulfils

$$\begin{vmatrix}
J_1(\kappa_n r_d) & -\frac{\kappa_n \epsilon_r}{\kappa'_n} J_1(\kappa'_n r_d) & -\frac{\kappa_n \epsilon_r}{\kappa'_n} Y_1(\kappa'_n r_d) & 0 & 0 & 0 \\
J_0(\kappa_n r_d) & -J_0(\kappa'_n r_d) & -Y_0(\kappa'_n r_d) & 0 & 0 & 0 \\
0 & 0 & 0 & J_1(\kappa_n r_d) & -\frac{\kappa_n}{\kappa'_n} J_1(\kappa'_n r_d) & -\frac{\kappa_n}{\kappa'_n} Y_1(\kappa'_n r_d) \\
0 & 0 & 0 & J_0(\kappa_n r_d) & -J_0(\kappa'_n r_d) & -Y_0(\kappa'_n r_d) \\
0 & J_0(\kappa'_n r_g) & Y_0(\kappa'_n r_g) & 0 & 0 & 0 \\
0 & 0 & 0 & 0 & J_1(\kappa'_n r_g) & Y_1(\kappa'_n r_g)
\end{vmatrix} = 0 \tag{A.6}$$

After some algebra, (A.6) can be simplified yielding the following condition, which is known as the dispersion relation of the lined waveguide,

$$\left(J_1(\kappa_n r_d) Y + \frac{\kappa_n}{\kappa'_n} J_0(\kappa_n r_d) Z\right)\left(J_1(\kappa_n r_d) W + \frac{\kappa_n \epsilon_r}{\kappa'_n} J_0(\kappa_n r_d) X\right) = 0 \tag{A.7}$$

where the following definitions apply:

$$\begin{aligned}
W &= \begin{vmatrix} J_0(\kappa'_n r_g) & Y_0(\kappa'_n r_g) \\ J_0(\kappa'_n r_d) & Y_0(\kappa'_n r_d) \end{vmatrix} \quad X = \begin{vmatrix} J_1(\kappa'_n r_d) & Y_1(\kappa'_n r_d) \\ J_0(\kappa'_n r_g) & Y_0(\kappa'_n r_g) \end{vmatrix} \\
Y &= \begin{vmatrix} J_1(\kappa'_n r_g) & Y_1(\kappa'_n r_g) \\ J_0(\kappa'_n r_d) & Y_0(\kappa'_n r_d) \end{vmatrix} \quad Z = \begin{vmatrix} J_1(\kappa'_n r_d) & Y_1(\kappa'_n r_d) \\ J_1(\kappa'_n r_g) & Y_1(\kappa'_n r_g) \end{vmatrix}
\end{aligned} \tag{A.8}$$

The dispersion relation of the waveguide given in equation (A.7) provides the relation between the frequency ω and the wavenumber k_{zn} for the nth mode. Besides the dispersion relation, the set of equations (A.5) also provides a relation between the constant coefficients $A_1, \ldots, D_2$,

which can be written in the following way:

$$\begin{aligned}
A_2 &= \tfrac{1}{2}\pi\kappa_n' r_d \left[\tfrac{\kappa_n'}{\epsilon_r\kappa_n} Y_0(\kappa_n' r_d) J_1(\kappa_n r_d) - J_0(\kappa_n r_d) Y_1(\kappa_n' r_d)\right] A_1 \\
B_2 &= -\tfrac{1}{2}\pi\kappa_n' r_d \left[\tfrac{\kappa_n'}{\epsilon_r\kappa_n} J_0(\kappa_n' r_d) J_1(\kappa_n r_d) - J_0(\kappa_n r_d) J_1(\kappa_n' r_d)\right] A_1 \\
C_2 &= \tfrac{1}{2}\pi\kappa_n' r_d \left[\tfrac{\kappa_n'}{\kappa_n} Y_0(\kappa_n' r_d) J_1(\kappa_n r_d) - J_0(\kappa_n r_d) Y_1(\kappa_n' r_d)\right] C_1 \\
D_2 &= -\tfrac{1}{2}\pi\kappa_n' r_d \left[\tfrac{\kappa_n'}{\kappa_n} J_0(\kappa_n' r_d) J_1(\kappa_n r_d) - J_0(\kappa_n r_d) J_1(\kappa_n' r_d)\right] C_1
\end{aligned} \tag{A.9}$$

From equations (A.9) one can see that the solution of the field depends on only two constants, namely, A_1 and C_1. By using (A.9) and (A.2), the transverse eigenmodes can be now written in the following way.

For the region $0 < r < r_d$

$$\vec{\mathcal{E}}_n(r) = \begin{pmatrix} -i\frac{k_{zn}}{\kappa_n} J_1(\kappa_n r) A_1 \\ -i\frac{\omega}{\kappa_n} J_1(\kappa_n r) C_1 \\ J_0(\kappa_n r) A_1 \end{pmatrix} \qquad \vec{\mathcal{B}}_n(r) = \begin{pmatrix} -i\frac{k_{zn}}{\kappa_n} J_1(\kappa_n r) C_1 \\ -i\frac{\omega}{\kappa_n c_0^2} J_1(\kappa_n r) A_1 \\ J_0(\kappa_n r) C_1 \end{pmatrix} \tag{A.10}$$

and for the region $r_d < r < r_g$

$$\begin{aligned}
\vec{\mathcal{E}}_n(r) &= \begin{pmatrix} -i\frac{k_{zn}}{\kappa_n'}(a_n J_1(\kappa_n' r) + b_n Y_1(\kappa_n' r) A_1) \\ -i\frac{\omega}{\kappa_n'}(c_n J_1(\kappa_n' r) + d_n Y_1(\kappa_n' r) C_1) \\ a_n J_0(\kappa_n' r) + b_n Y_0(\kappa_n' r) A_1 \end{pmatrix} \\
\vec{\mathcal{B}}_n(r) &= \begin{pmatrix} -i\frac{k_{zn}}{\kappa_n'}(c_n J_1(\kappa_n' r) + d_n Y_1(\kappa_n' r) C_1) \\ -i\frac{\omega\epsilon_r}{\kappa_n' c_0^2}(a_n J_1(\kappa_n' r) + b_n Y_1(\kappa_n' r) A_1) \\ c_n J_0(\kappa_n' r) + d_n Y_0(\kappa_n' r) C_1 \end{pmatrix}
\end{aligned} \tag{A.11}$$

where the following definitions apply:

$$\begin{aligned}
a_n &= \frac{1}{2}\pi\kappa_n' r_d \left[\frac{\kappa_n'}{\epsilon_r\kappa_n} J_1(\kappa_n r_d) Y_0(\kappa_n' r_d) - J_0(\kappa_n r_d) Y_1(\kappa_n' r_d)\right] \\
b_n &= -\frac{1}{2}\pi\kappa_n' r_d \left[\frac{\kappa_n'}{\epsilon_r\kappa_n} J_1(\kappa_n r_d) J_0(\kappa_n' r_d) - J_0(\kappa_n r_d) J_1(\kappa_n' r_d)\right] \\
c_n &= \frac{1}{2}\pi\kappa_n' r_d \left[\frac{\kappa_n'}{\kappa_n} Y_0(\kappa_n' r_d) J_1(\kappa_n r_d) - J_0(\kappa_n r_d) Y_1(\kappa_n' r_d)\right] \\
d_n &= -\frac{1}{2}\pi\kappa_n' r_d \left[\frac{\kappa_n'}{\kappa_n} J_0(\kappa_n' r_d) J_1(\kappa_n r_d) - J_0(\kappa_n r_d) J_1(\kappa_n' r_d)\right]
\end{aligned} \tag{A.12}$$

Finally, the general solution of the electromagnetic field propagating in the lined cylindrical waveguide is obtained by substituting (A.10) and (A.11) in (A.1). As said before, the modes depend on two constants, which, in turn, are determined by the power of the electromagnetic field. Further, the modes can be divided in two distinct sets by making each of these constants equal to zero. To more detail, modes with a zero longitudinal component for the magnetic field, called transverse magnetic or TM_{0n} modes, are obtained by making $C_1 = 0$ in equations (A.10) and (A.11). Similarly, modes with a zero longitudinal component for the electric field, called transverse electric or TE_{0n} modes, are obtained by making $A_1 = 0$ in equations (A.10) and (A.11).

Bibliography

[1] H. Hertz (translated by D.E. Jones). *Electric Waves*. Dover Publications Inc., New York, (1962).

[2] H. Sobol. Microwave communications. A historical perspective. *Microwave Theory and Techniques, IEEE Transactions on*, 32(9):1170–1181, (1984).

[3] M. Makowski. ECRF systems for ITER. *IEEE Transactions on Plasma Science*, 24(3):1023 – 1032, (1996).

[4] V.L. Granatstein and W. Lawson. Gyro-amplifiers as candidate RF drivers for TeV linear colliders. *IEEE Transactions on Plasma Science*, 24(3):648–665, (1996).

[5] A.W. Guy. History of biological effects and medical applications of microwave energy. *Microwave Theory and Techniques, IEEE Transactions on*, 32(9):1182–1200, (1984).

[6] E.T. Thostenson and T.W. Chou. Microwave processing:fundamentals and applications. *Composites Part A:Applied Science and manufacturing*, 30:1055–1071, (1999).

[7] D.E. Clark, D.C. Folz, and J.K. West. Processing materials with microwave energy. *Materials Science and Engineering A*, A287:153–158, (2000).

[8] E.J. Minay, A.R. Boccaccini, P. Veronesi, V. Cannillo, and C. Leonelli. Processing of novel glass matrix composites by microwave heating. *Journal of Materials Processing Technology*, 155-156:1749–1755, (2004).

[9] M. Al-Harahsheh and S.W. Kingman. Microwave-assisted leaching-a review. *Hydrometallurgy*, 73:189–203, (2004).

[10] K.E. Haque. Microwave energy for mineral treatment processes-a brief review. *International Journal of Mineral processing*, 57:1–24, (1999).

[11] D.A. Jones, T.P. Lelyveld, S.D. Mavrofidis, S.W. Kingman, and N.J. Miles. Microwave heating applications in environmental engineering-a review. *Resources, Conservation and Recycling*, 34:75–90, (2002).

[12] R.J. Wise and I.D. Froment. Microwave welding of thermoplastics. *Journal of Materials Science*, 36:5935–5954, (2001).

[13] P.D.D.V. Yarlagadda and T.C. Chai. An investigation into welding of engineering thermoplastics using focused microwave energy. *Journal of Materials Processing Technology*, 74:199–212, (1998).

[14] G. Bonizzoni and E. Vassallo. Plasma physics and technology;industrial applications. *Vacuum*, 64:327–336, (2002).

[15] P. Mavromatidis, A. Shaw, A.I. Al-Shamma'a, J. Lucas, and W. Lucas. 2.45 GHz microwave plasma system for high-velocity thermal spraying. *Journal of Materials Processing Technology*, 153-154:294–299, (2004).

[16] J. Feichtinger, A. Schult, M. Walker, and U. Schumacher. Sterilization with low-pressure microwave plasmas. *Surface and coatings technology*, 174-175:564–569, (2003).

[17] S.R. Wylie, A.I. Al-Shamma'a, J. Lucas, and R.A. Stuart. An atmospheric microwave plasma jet for ceramic material. *Journal of Materials Processing Technology*, 153-154:288–293, (2004).

[18] S.R. Wylie, A.I. Al-Shamma'a, and J. Lucas. Microwave plasma system for material processing. *IEEE Transactions on Plasma Science*, 33(2I):340 – 341, (2005).

[19] D. Michaud, J. Hamelin, F. Texier-Boullet, and L. Toupet. MIMIRC Reactions of nitromethane with electrophilic alkenes in solvent-free reactions under microwave irradiation. *Tetrahedron*, 58:5865–5875, (2002).

[20] L. Paquin, J. Hamelin, and F. Texier-Boullet. Efficient microwave-assisted solvent-free synthesis of n-substituted aldimines. *Synthesis*, (10):1652 – 1656, (2006).

[21] J. Luo, C. Hunyar, L. Feher, G. Link, M. Thumm, and P. Pozzo. Potential advantages for millimeter-wave heating of powdered metals. *International Journal of Infrared and Millimeter Waves*, 25(9):1271–1283, (2004).

[22] E.L. Ginzton. The $100 idea. *Electron Devices, IEEE Transactions on*, 23:714–723, (1976).

[23] H.A.H. Boot and J.T. Randall. Historical notes on the cavity magnetron. *Electron Devices, IEEE Transactions on*, 23:724–729, (1976).

[24] R. Kompfner. The invention of traveling wave tubes. *Electron Devices, IEEE Transactions on*, 23:730–738, (1976).

[25] J.C. Wiltse. History of millimeter and submillimeter waves. *IEEE Transactions on Microwave Theory and Techniques*, MIT-32:1118, (1984).

[26] H. Motz. Applications of the radiation from fast electron beams. *Journal of Applied Physics*, 22:527, (1951).

[27] R.M. Phillips. The ubitron, a high power traveling-wave tube based on a periodic beam interaction in an unloaded waveguide. *I.R.E. Trans. Electron Dev.*, 7:231, (1960).

[28] V.A. Flyagin and G.S. Nusinovich. Gyrotron oscillators. *Proceedings of the IEEE*, 76(6):644 – 656, (1988).

[29] J.M.J. Madey. Stimulated emission of bremsstrahlung in a periodic magnetic field. *Journal of Applied Physics*, 42:1906, (1971).

[30] L.R. Elias, W.M. Fairbank, J.M.J. Madey, H.A. Schwettman, and T.I. Smith. Observation of stimulated emission of radiation by relativistic electrons in a spatially periodic transverse magnetic field. *Physical Review Letters*, 36:717, (1976).

[31] D.A.G. Deacon, L.R. Elias, J.M.J. Madey, G.J. Ramian, H.A. Schwettman, and T.I. Smith. First operation of a free-electron laser. *Physical Review Letters*, 8:892, (1977).

[32] C.A. Brau. *Free-Electron Lasers*. Academic Press, Inc., (1990).

[33] E.L. Saldin, E.A. Schneidmiller, and M.V. Yurkov. *The Physics of Free Electron Lasers*. Springer-Verlag Berlin Heidelberg, (2000).

[34] H.P. Freund. *Principles of Free-Electron Lasers*. Chapman and Hall, London, (1996).

[35] T.C. Marshall. *Free-Electron Lasers*. Macmillan, (1985).

[36] A. Gover and P. Sprangle. A unified theory of magnetic Bremsstrahlung, electrostatic Bremsstrahlung, Compton-Raman scattering, and Cerenkov-Smith-Purcell Free-Electron Lasers. *IEEE Journal of Quantum Electronics*, QE17(7):1196–1215, (1981).

[37] P.G. O'Shea and H.P. Freund. Free-electron lasers:status and applications. *Science*, 292:1853, (2001).

[38] M. Thumm. Free-electron maser vs. gyrotrons:prospects for high-power sources at millimeter and submillimeter wavelengths. *Nuclear Instruments and Methods in Physics Research A*, 483:186–194, (2002).

[39] J. Walsh, B. Johnson, G. Dattoli, and A. Renieri. Undulator and cerenkov free-electron lasers: A preliminary comparison. *Physical Review Letters*, 53:779–782, (1984).

[40] W. Case, editor. *High-Power Microwave Sources*, chapter Basic theory of Cerenkov radiators. Artech house, (1987).

[41] V.L. Ginzburg. *Dokl. Akad. Nauk SSSR*, 56(3):253–254, (1947).

[42] M. Danos *et al.* Cerenkov effect at microwave frequencies. *Physics Review*, 92:828, (1953).

[43] P. Coleman and C. Enderby. Megavolt electronics cerenkov coupler for the production of millimeter and submillimeter waves. *Journal of Applied Physics*, 31:1695, (1960).

[44] J.E. Walsh, T.C. Marshall, and S.P. Schlesinger. Generation of coherent cerenkov radiation with an intense relativistic electron beam. *The Physics of Fluids*, 20(4):709, (1977).

[45] S. Jacobs, H. Pilloff, M. Sargent, M. Scully, and R. Spitzer, editors. *Free Electron Generators of Coherent Radiation(Physics of Quantum Electronics)*, chapter Cerenkov and Cerenkov-Raman radiation sources, vol 7. Addison-Wesley, (1980).

[46] S. Von Laven, J. Walsh, J. Branscum, J. Golub, and R. Layman. High power Cerenkov maser oscillator. *Applied Physics Letters*, 41(5):408, (1981).

[47] K.L. Felch, K.O. Busby, R.W. Layman, K. Kapilow, and J.E. Walsh. Cerenkov radiation in dielectric-lined waveguides. *Applied Physical Letters*, 38(8):601, (1981).

[48] E.P. Garate, J. Walsh, S. Moustaizis, J.M. Buzzi, C. Rouille, H. Lamain, and B. Johnson. Cerenkov maser operation at 1-2 mm wavelengths. *Applied Physical Letters*, 48(20):1326, (1986).

[49] E. Garate, J. Walsh, C. Shaughnessy, B. Johnson, and S. Moustaizis. Cherenkov free electron laser operation from 375 to 1000 μm. *Nuclear Instruments and Methods A*, 259:125, (1987).

[50] K.L. Felch, K.O. Busby, R.W. Layman, and J.E. Walsh, editors. *Free Electron Generators of Coherent Radiation(Physics of Quantum Electronics)*, chapter Cerenkov and Cerenkov-Raman masers: experiments, vol 7. Addison-Wesley, (1980).

[51] J. Walsh. *Laser Handbook, edited by W.B. Colson and C. Pellegrini and A. Renieri*. The waveguide free-electron laser, North-Holland, Amsterdam, (1990).

[52] E. Garate, R. Cook., P. Heim, R. Layman, and J. Walsh. Cerenkov maser operation at lower-mm wavelengths. *Journal of Applied Physics*, 58(2):627, (1985).

[53] F. Ciocci, A. Doria, G.P. Gallerano, I. Giabbai, M.F. Kimmitt, G. Messina, A. Renieri, and J.E. Walsh. Observation of coherent millimeter and submillimeter emission from a microtron-driven Cherenkov free-electron laser. *Physical Review Letters*, 66(6):699–702, (1991).

[54] S.H. Gold and G.S. Nusinovich. Review of high-power microwave source research. *Review Scientific Instruments*, 68(11):3945, (1997).

[55] H.P. Freund. Nonlinear analysis of high-power Cherenkov masers. *Physical Review Letters*, 65:2993, (1990).

[56] E.P. Garate and J.E. Walsh. The Cerenkov maser at millimeter wavelengths. *IEEE Transactions on Plasma Science*, 13:524–530, (1985).

[57] H.P. Freund and A.K. Ganguly. Nonlinear analysis of the Čerenkov maser. *Physics of Fluids B*, 2:2506, (1990).

[58] R. Bonifacio, F. Casagrande, and C. Pellegrini. Hamiltonian model of a free electron laser. *Optical Communications*, 61:55, (1987).

[59] L. De Salvo Souza R. Bonifacio and C. Pellegrini, editors. *High Gain, High Power Free Electron Laser*, chapter One-Dimensional Theory of a Free-Electron Laser Amplifier:Steady-State and Superradiance, pages 35–95. Elsevier Science Publishers B.V., (1989).

[60] S. Jacobs, H. Pilloff, M. Sargent, M. Scully, and R. Spitzer, editors. *Free Electron Generators of Coherent Radiation(Physics of Quantum Electronics)*, chapter Stimulated Cerenkov Radiation, vol 5. Addison-Wesley, (1980).

[61] A. Gover and Z. Livni. Operation Regimes of Cerenkov-Smith-Purcell Free Electron Lasers and T.W.A. *Optics Communications*, 26(3):375, (1978).

[62] J.E. Walsh and J.B. Murphy. Tunable Cerenkov Lasers. *Journal of Quantum Electronics*, QE-18:1259, (1982).

[63] P.J.M. van der Slot. *A free-electron laser operating in the collective regime*. PhD thesis, University of Twente, (1992).

[64] E. Garate, R. Cherry, and A. Fisher. Far infrared cherenkov free electron laser. *Nuclear Instruments and Methods in Physics Research A*, 272:129–131, (1988).

[65] E.E. Fisch and J.E. Walsh. Operation of the sapphire Cerenkov laser. *Applied Physical Letters*, 60(11):1298, (1992).

[66] W. Peter and E. Garate. Stimulated Cherenkov emission in dielectric-lined waveguides. *Physical Review A*, 45:8833, (1992).

[67] J. Wieland, J. Couperus, P.J.M. van der Slot, and W.J. Witteman. First lasing of a Cherenkov free-electron laser with annular electron beam. *Nuclear Instruments and Methods in Physics Research A.*, 429:17–20, (1999).

[68] P.A. Cerenkov. Sichtbares Luchten von reinen Flussigkeiten unter der Einwirkung von gamma Strahlen. *Dokl. Akad. Nauk SSSR*, 2:451, (1934).

[69] P.A. Cerenkov. Visible Radiation Produced by Electrons Moving in a Medium with Velocities Exceeding that of Light. *Physical Review*, 52:378–379, (1937).

[70] I. Frank and I. Tamm. Coherent Visible Radiation of Fast Electrons Passing Through Matter. *Dokl. Aka. Nauk SSSR*, 14:109–14, (1937).

[71] J.V. Jelly. *Cerenkov Radiation and its Applications*. Pergammon, London, (1958).

[72] J.G. Linhart. Cerenkov radiation of electrons moving parallel to a dielectric boundary. *Journal of Applied Physics*, 26:527, (1955).

[73] M. Danos. Cerenkov radiation from extended electron beams. *Journal of Applied Physics*, 26(1):62–68, (1955).

[74] M. Abramowitz and I.A. Stegun. *Handbook of Mathematical Functions with Formulas, Graphs, and Mathematical Tables*. New York: Dover, (1972).

[75] R.A. Waldron. *Theory of guided electromagnetic waves*. Van Nostrand Reinhold Company, London, (1970).

[76] W.B. Westphal and A. Sils. Dielectric constant and loss data. *Technical Report AFML-TR-72-39, Massachusetts Institute of Technology*, (1972).

[77] P.J.M. van der Slot *et al.* A Cherenkov free electron laser with high peak power. *Nuclear Instruments and Methods in Physics Research A.*, 358:100–103, (1995).

[78] S.M. Wiggins *et al.* Self-Amplification of Coherent Spontaneous Emission in a Cherenkov Free-Electron Maser. *Physical Review Letters*, 84:2393, (2000).

[79] F. Ciocci, A. Doria, G.P. Gallerano, I. Giabbai, M.F. Kimmitt, G. Messina, A. Renieri, and J.E. Walsh. Observation of coherent millimeter and submillimeter emission from a microtron-driven cherenkov free-electron laser. *Physical Review Letters*, 66(6):699, (1991).

[80] www.gequartz.com.

[81] J. Molla, R. Heidinger, and A. Ibarra. Alumina ceramics for heating systems. *Journal of Nuclear Materials*, 212-215:1029–1034, (1994).

[82] J. Krupka, Wei-Te Huang, and Mean-Jue Tung. Complex permittivity measurements of low-loss microwave ceramics employing higher order quasi TE_{0np} modes excited in a cylindrical dielectric sample. *Measurement Science and Technology*, 16(4):1014–1020, 2005.

[83] J.L. Cronin. Practical Aspects of Modern Dispenser Cathodes. *Techn. Bulletin of Spectra Mat, Incorporated, Watsonville, CA*, pages 57–62, (1979).

[84] R.L. Sheffield. High-brightness electron injectors: A review. *Proc. 1989 IEEE Part. Accel. Conf.*, pages 1098 – 1102, (1989).

[85] J.W. Gewartowski and H.A. Watson. *Introduction to electron tubes*. Van Nostrand Reinhold Co, (1969).

[86] R.E. Thomas, J.W. Gibson, G.A. Haas, and R.H. Abrams. Thermionic sources for high-brightness electron beams. *IEEE Transactions on Electronic Devices*, 37:850–861, (1990).

[87] E.R. Gray R.L. Sheffield and J.S. Fraser. The Los Alamos photoinjector program. *Nuclear Instruments and Methods in Physics Research Section A: Accelerators, Spectrometers, Detectors and Associated Equipment*, pages 222–226, (1988).

[88] F.M. Mako and W. Peter. A High-Current Micro-Pulse Electron Gun. *IEEE PAC*, pages 2702–2704, (1993).

[89] N.S. Xu and S.E. Huq. Novel cold cathode materials and applications. *Material Science and Engineering*, R 48:47–189, (2005).

[90] R. Levi. Improved impregnated cathode. *Journal of Applied Physics*, 26:639, (1955).

[91] J.L. Cronin. Modern Dispenser Cathodes. *IEE Proceedings*, 128(1):19–32, (1981).

[92] P. Zalm and A. van Stratum. Osmium dispenser cathodes. *Philips Techn. Rev.*, 27:36, (1966).

[93] L.R. Falce. High Current Density Dispenser Cathode Surface Activation Phenomena in long Life Vacuum Electron Devices. *The 29th IEEE International Conference on Plasma Science*, page 128, (2002).

[94] R. Bachmor. Lifetime Experience with low Temperature Cathodes equipped in Super Power Klystrons. *IEEE PAC*, (1995).

[95] e2v Technologies Ltd., Essex, England, e2v.com.

[96] J.R. Pierce. *Theory and design of Electron beams*. New York: Van Nostrand, (1954).

[97] Field Precision, PO Box 13595, Albuquerque, New Mexico 87192 USA, www.fieldp.com.

[98] R.T. Bayard and D. Alpert. *Review of Scientific Instruments*, 21:571, (1950).

[99] D. Alpert. New Developments in the Production and Measurement of Ultra High Vacuum. *Journal of Applied Physics*, 24(7), (1953).

[100] S. Sato and K. Kenichi. Relationship between electrode surface roughness and impulse breakdown voltage in vacuum gap of Cu and Cu-Cr electrodes. *IEEE transactions on dielectrics and electrical insulation*, 10(4):576, (2003).

[101] R.E. Collin. *Foundations for Microwave Engineering*. McGraw-Hill, New York, (1966).

[102] Flann microwaves, flann.com.

[103] 2005 PXI Systems Alliance, pxisa.org.

[104] National Instruments Corporation, ni.com.

[105] I. de la Fuente, P.J.M. van der Slot, and K.J. Boller. Phase velocity fluctuations and gain in Cherenkov free-electron lasers. *Journal of Applied Physics*, 100(5):053108, (2006).

[106] P.J.M. van der Slot, I. de la Fuente, and K.J. Boller. Cerenkov free-electron lasers as compact sources for thz radiation. *International Forum on Terahertz Spectroscopy and Imaging*, Kaiserslautern, (Germany), (2006).

Acknowledgments

In these lines I take the opportunity to thank all the persons who contributed in some way or other to the completion of this thesis.

Firstly, I express my gratitude to Huub van Heel and Klaus Boller for offering me the opportunity of joining, first, the Nederlands Centrum voor Laser Research (NCLR), and then, the Laser Physics and Non-Linear Optics group (LPNO). Thank you, Klaus, for all your advices and comments over the years. Thank you also for your clear, elegant and simple manner of illustrating ideas and for letting us enjoy it.

I am specially grateful to my daily supervisor and co-promotor, Peter van der Slot, for his useful and helpful assistance. Thank you, Peter, for you enormous dedication, enthusiasm, effort and patience with me.

My gratitude as well to Vinod Subramaniam, Markus Pollnau and Wim van der Zande for kindly agreeing to form part of the evaluation committee of this thesis. Thanks also to Jordi and Petra for being my *paranimfen* during the defence.

I am grateful to the members of LPNO group and NCLR for their experience and, more importantly, for being patient enough to teach it to beginners like me. Particularly, thanks to Gerard Oudemeijers and Jacob Couperus for their enormous support in the laboratory. Thanks also to Arco, who initiated me in the experimental setup of the CFEL. Thanks to Jeroen, for his recommendations in the lab, and to Arsen, for his help with theoretical issues. Thanks also to Peter and Rolf, who helped me with the Dutch summary of the thesis, and to Ian, for "fine-tuning" the English.

My colleagues of the LPNO group and of NCLR have contributed to make me feel at the office almost like at a second home. I am grateful to all of them: to Balaji, for his big smile; to Denny, for being such a big support; to Petra and Lars, for our Physics meetings; to Liviu, for all his advice; to Ian and Chris, for their irony; to Rolf, Arie, Dimitri, Olivier, Ronald, Roel, Martijn, Hein,... for their fresh company; to Ab, for his never-ending willingness to help; to Claudia and Simone, for their assistance with paperwork; to Bert, for his questions; and to all others-Anton, Denis, Willem, Fred, Jeroen, Piet, Leon, Cees, Ramon, Otto, Peter- for

contributing so positively to this work.

Thank you to many other friends from other groups of the University of Twente, and from outside it, who I have met during these years of my PhD: Laura, Ricardo, Marvin, Martin, Rogelio, Verena, Elena, Giorgia,... I apologize for not mentioning all your names here. I am glad I could enjoy your company, your fun, and your support during this time.

Thank you to the Spanish community in Enschede, for letting me form part of it on my arrival to The Netherlands. Thanks to Gabriel, Jordi, Oliván, Ana, Sesé, Seve, Marta, Luis, Elisa, Miguel and Sonia for making me grow so much, for sharing so much fun, and for being my home in the early years of the thesis.

Thanks to my friends from Olombrada. Thank you to Esther, Gemma, Alberto, Isabel, Mari y Olga, for your particular sense of humour, which has contributed to make the distances shorter and the returns home more enjoyable. Also thanks to Diego and Auri, for being always there.

Special thanks to Balaji and to Jordi for giving me the opportunity of discovering their friendship during this time.

Gracias Gabriele por estar siempre presente. Gracias por escucharme, por comprenderme, por animarme, por hacerme reir, por hacerme enfadar, por enseñarme, por aprender de mí, por criticarme, por apoyarme. Gracias, en definitiva, por haber sabido compartir tanto conmigo durante este tiempo. Grazie anche a Rosanna, Umberto e Ilaria, per essere sempre così affetuosi e simpatici con me.

Por último, gracias a toda mi familia por su cercanía y cariño: a mi abuela Flores, a mi hermano Luis, a María, a mis tíos y a mis primos. Especialmente, gracias a mis padres, Miguel y Carmen. Gracias por respetar siempre mis decisiones, aunque a veces sean irracionales e incomprensibles. Y gracias por, incondicionalmente, prestarme siempre vuestro apoyo. Vuestro apoyo cuando me equivoco y, lejos de increparme, me dais ánimos y fuerzas. Y vuestro apoyo, también, en los buenos ratos, esos que se disfrutan más al compartirlos. Sabeis hacerlo mejor que nadie. Por eso, y por mucho más, os doy mil gracias.

Enschede, 10^{th} February 2007.